

Mechanical behaviour under thermal loading of metallic thin films used as catalysts for graphene growth under CVD

Luís Maldonado Abreu Castelo Branco

Thesis to obtain the Master of Science Degree in

Industrial Engineering and Management

Supervisors: Prof. Augusto Manuel Moura Moita de Deus

Prof. Paulo Jorge Matos Fernandes Martins Ferreira

Prof. João Pedro dos Santos Hall Agorreta de Alpuim

Examination Committee

Chairperson: Prof. Miguel Simões Torres Preto

Supervisor: Prof. Augusto Manuel Moura Moita de Deus

Member of the Committee: Prof. Maria de Fátima Reis Vaz

December 2019

Declaração

Declaro que o presente documento é um trabalho original da minha autoria e que cumpre todos os requisitos do Código de Conduta e Boas Práticas da Universidade de Lisboa.

Declaration

I declare that this document is an original work of my own authorship and that it fulfills all the requirements of the Code of Conduct and Good Practices of the Universidade de Lisboa.

Table of Contents

List of Figures	vii
List of Tables	viii
List of Symbols	ix
List of Abbreviations	x
Resumo	xi
Abstract.....	xii
1. Introduction.....	1
1.1- Defining the problem.....	2
2. Literature Review	5
2.1-The Dewetting Process.....	5
2.1.1- Hole formation in the thin film	6
2.1.2- Hole growth	8
2.1.3-Overall dewetting rate	11
2.1.4- Single-crystal films	12
2.1.5 - Controlling dewetting	13
2.2-Stresses in thin films.....	14
2.2.1-Intrinsic stresses	14
2.2.2- Thermal stresses.....	16
3. Methodology.....	19
3.1-Geometry	19
3.2 - Dimensional analysis.....	21
3.3- Material Properties.....	21
3.4-Thermal load and boundary conditions	23
3.5- Convergence Studies	25
3.5.1- Bidimensional model.....	25
3.5.2- Three-dimensional model	27
3.6 - Assumptions	30
4. Results	31
4.1 Bidimensional study	31
4.1.1 - Copper films.....	31

4.1.2 - Molybdenum films	38
4.2 Three dimensional studies	45
5. Conclusions.....	53
Bibliography	56
Appendix.....	58
Appendix A: Methodology	58
Conversion table	58
Convergence for the 2D model	59
Convergence for the 3D model	61

List of Figures

Fig 1.1 - Example of a simple CVD setup [2]	2
Fig 2.1 - Schematic example of thin film dewetting[8]	5
Fig 2.2 - Schematic representation of grain boundary grooves[8]	7
Fig 2.3 - Schematic representation of edge retraction and subsequent pinch-off[8]	9
Fig 2.4 - Image of fingering instabilities in an Au film[8]	9
Fig 2.5 - Images of growing holes in Si films[8]	12
Fig 2.6 - Generic diagram of the evolution of Force per width over time for high and low mobility materials[20]	15
Fig 2.7 - Stress-temperature plot for an Al film on a Si substrate [22]	16
Fig 2.8 - Stress-Temperature plot for a film (Al+1%Si+2.5%Ti) on Si as-deposited heat-cycle[21]	17
Fig 3.1 - Assembly of a thin copper film atop a SiO ₂ and Si substrate	19
Fig 3.2 - Schematic of the bidimensional model	20
Fig 3.3 - Example of the stress-strain curves used for the model	22
Fig 3.4 - Evolution of temperature with time	24
Fig 3.5 - Schematic of the boundary conditions applied to the model	25
Fig 3.6 - von Mises stress in a bidimensional model at the end of the heating phase at 900°C (Stress in TPa)	26
Fig 3.7 – Convergence study for von Mises stress at the centre for a bidimensional model	27
Fig 3.8 – Convergence study for displacement at the centre for a bidimensional model	27
Fig 3.9 – von Mises stress in a three-dimensional model at the end of the heating phase at 250°C. Stress in TPa	28
Fig 3.10 – Convergence study for von Mises stress at the centre for a three-dimensional model	29
Fig 3.11 – Convergence study for displacement at the centre for a three-dimensional model	29
Fig 4.1 - Von Mises stress at the centre of a 900nm copper film	31
Fig 4.2 - Von Mises stress at the extremity of a 900nm copper film	32
Fig 4.3 - S11 stress at the centre of a 900nm copper film	32
Fig 4.4 - S33 stress at the centre of a 900nm copper film	33
Fig 4.5 - Evolution of yield stress with temperature and comparison with von Mises stress from 900nm copper film	33
Fig 4.6 - Plastic strain at the centre of a 900nm copper film	34
Fig 4.7 - Evolution of yield stress with temperature and comparison with von Mises stress from 900nm copper film	34
Fig 4.8 - S22 stress at the extremity of 900nm copper film	35
Fig 4.9 - S33 stress at the extremity of a 900nm copper film	35
Fig 4.10 - Plastic strain at the extremity of a 900nm copper film	36
Fig 4.11 - Evolution of von Mises stress with the change in copper film thickness. From top to bottom: 900nm, 480nm, 120nm, 30nm. Only half of the film is represented	37
Fig 4.12 - von Mises stress at the centre of a 900nm molybdenum film	38

Fig 4.13 - von Mises stress at the extremity of a 900nm molybdenum film	39
Fig 4.14 - S11 at the centre of a 900nm molybdenum film	39
Fig 4.15 - S33 at the centre of a 900nm molybdenum film	40
Fig 4.16 - S22 at the extremity of a 900nm molybdenum film	40
Fig 4.17 - Plastic strain at the centre of a 900nm molybdenum film	40
Fig 4.18 – Evolution of von Mises stress with the change in molybdenum film thickness. From top to bottom: 900nm, 480nm, 120nm, 30nm. Only half of the film represented	41
Fig 4.19 - von Mises stress at the centre of a 900nm copper film	42
Fig 4.20 - von Mises stress at the centre of a 900nm molybdenum film	43
Fig 4.21 - Evolution of yield stress with homologous temperature in copper and molybdenum.....	43
Fig 4.22 - Plastic strain at the centre of a 900nm molybdenum film	44
Fig 4.23 - Plastic strain at the centre of a 900nm copper film.....	44
Fig 4.24 - Comparison between 2D and 3D von Mises stress of a 480nm copper film, at the centre..	45
Fig 4.25 - von Mises stress at the centre of a 480nm copper film, 3D modell	46
Fig 4.26 - S33 at the centre of a 480nm copper film, 3D modell	46
Fig 4.27 - Plastic strain at the centre of a 480nm copper film, 3D model	47
Fig 4.28 - von Mises stress at the centre of a 480nm copper film, 3D model.....	48
Fig 4.29 - von Mises stress at the centre of a 120nm copper film, 3D model.....	48
Fig 4.30 - S33 at the centre of a 120nm copper film, 3D model	49
Fig 4.31 - Plastic strain at the centre of a 120nm molybdenum film, 3D model	49
Fig 4.32 - von Mises stress at the centre of a 120nm copper film, 3D model.....	50
Fig 4.33 - S33 at the centre of a 120nm copper film, 3D model	50
Fig 4.34 - Plastic strain at the centre of a 120nm copper film, 3D model	51

List of Tables

Table 3.1 - Mechanical properties for the materials used in the model	23
Table 4.1 - Residual values for copper film results	51

List of Symbols

γ	Surface energy
θ, φ	Equilibrium Angle
β	Composite parameter
R, r	Radius
h	Thickness
d, δ	Notch depth
\dot{N}	Hole nucleation rate
D_s	Surface diffusivity of the film
J	Flux
$\nabla_s k$	Surface gradient of the surface curvature
Ω	Atomic volume
k_B	Boltzmann's constant
T	Temperature
t	Time
\dot{x}_0	Edge retraction rate
X_{dewet}	Dewetting rate
Q, q	Activation energy
Δp	Mechanical action
f	Surface stress
σ, σ', S	Stress
E	Young's Modulus
α	Thermal expansion coefficient
e, \mathcal{E}	Strain
R	Universal gas constant (Equation 3.5 only)

List of Abbreviations

INL	International Iberian Nanotechnology Laboratory
CVD	Chemical Vapor Deposition
CNT	Carbon Nanotube

Resumo

Com o maior foco na miniaturização da tecnologia hoje em dia, nanotecnologia e em particular materiais 2D como o grafeno têm recebido considerável atenção em tempos recentes. A técnica mais utilizada para a sua produção é o CVD, ou chemical vapour deposition, usando um filme fino metálico como catalisador para o crescimento. Têm sido feitas tentativas de realizar este processo com filmes de cobre cada vez mais finos e reduzir custos de material, mas as altas temperaturas necessárias para o processo causam instabilidades no filme que comprometem a sua integridade e impedem o crescimento do grafeno. As tensões a que o filme está submetido durante o processo podem causar instabilidades.

Nesse sentido, foi desenvolvido um modelo usando o método dos elementos finitos com o software Abaqus, quer em 2D quer em 3D, em que filmes com diferentes espessuras são submetidos a um ciclo térmico que simule o processo de CVD, permitindo estudar o seu comportamento mecânico.

Os resultados mostram que a variação da espessura do filme tem um impacto limitado nos valores observados para as tensões. A deformação plástica residual é normalmente baixa para os casos que foram estudados ($\approx 0,2\%$), mas a possibilidade existe de que esse facto não possa ser negligenciado, no que toca ao crescimento do filme de grafeno. Foi ainda feita uma comparação com o molibdénio que mostra que existem comportamentos similares nos dois casos, em particular quando se introduz o conceito de temperatura homóloga. Os resultados da análise 3D confirmaram as conclusões do estudo bidimensional.

Palavras-chave: Carregamento térmico, filmes finos, crescimento de grafeno, método dos elementos finitos

Abstract

As boundaries in the miniaturization of technology are being pushed to smaller lengths, nanotechnology and in particular 2D materials such as graphene have been subject of considerable recent attention. The preferred technique for its production is chemical vapour deposition (CVD), using a copper thin film as a catalyst for growth. Attempts have been made to lower the film's thickness to reduce material costs, but this causes the film to become unstable at higher temperatures, which in turn inhibits graphene growth. It is thought that the stresses the film is under during the process can be a source for unstable behaviour.

A model using the finite element method was developed using the software Abaqus both in 2D and 3D, where films of different thicknesses would undergo a thermal cycle simulating that of the CVD process, so as to study the mechanical behaviour of the thin film during that process.

The results showed that stress levels remained similar for all film thicknesses. Residual plastic strain is usually low in the cases studied ($\approx 0,2\%$), but there is the possibility that this cannot be neglected, as far as graphene film growth is concerned. A comparison with molybdenum showed that the behaviours of the two materials were similar, especially when the concept of homologous temperature is introduced. The results of the 3D analysis confirmed the findings of the bidimensional study.

Keywords: Thermal loading, thin films, graphene growth, finite element method

1. Introduction

We live in a world where the latest technology is at our fingertips. Artificial Intelligence (AI) in autonomous vehicles and personal assistance, pocket sized computers and the increasing influence of Internet of Things (IoT) devices shape our lives.

It is then intriguing how, even though we live in such a connected world, the role of materials and the material revolution needed is not yet perceived by the general population. As pointed out by Moita de Deus[1], the attendance and attention given to the Nanotechnology Summit, organized by the International Iberian Nanotechnology Laboratory (INL), centered around a technology that may shape the world in the long term, was much lighter than that of the Web Summit, which was centered around technology that has been around for some time.

One of the many fields of nanotechnology is the development of 1D and 2D materials. These materials possess characteristics that are impressive compared to the materials that we use today, however their manufacturing processes are still at an early age and research must be done to better understand what conditions their growth.

In this study, we will take a look at one specific process, called chemical vapour deposition, and how metallic thin films, which are commonly used for growing nanomaterials like graphene, are affected during the process. After discussing the process of graphene growth, we will delve into some of the limitations faced by the metallic thin films that serve as catalysts during the process. We then will discuss the model that was developed for this study that aims to recreate the thermal loading that the catalysts are under during the CVD process, before analyzing and discussing the results obtained from the simulations.

1.1- Defining the problem

One of 2D materials of great interest is graphene which is a film comprised of a single layer of carbon atoms. Although it is a very thin material, graphene is a material that is many times stronger than steel while remaining lightweight and flexible. It is also a very good thermal and electric conductor. This variety of outstanding properties makes this material very attractive for a very wide range of implementations in very different fields.

Another nanomaterial of interest is the carbon nanotubes (CNT), a tubular structure made from carbon atoms, with a diameter in the nanometer range and can be several micrometers or even millimeters long. Despite the small size, the material properties of CNT are similar to the properties of graphene: it is up to 100 times stronger than steel while being 6 times lighter, it is as hard as diamond and has twice its thermal capacity, is thermally stable up to 4000K, has 1000 times the current-carrying capacity of Copper and can be either metallic or semi-conductive depending on the diameter of the tubes and chirality. However, these are based on ideal CNT structures, without any defects.[2]

The applications for both structures are similar, though the way it is implemented differs. They can be already found in filters, fibers, coatings, electronics.

The most commonly used technique nowadays for synthesis is Chemical Vapor Deposition (CVD) (Fig 1.1) which consists of a catalyst-assisted decomposition of hydrocarbons. In its most basic form, a hydrocarbon vapor would pass through a tubular reactor where the catalyst material is heated to high temperatures, from 600°C to 1200°C, or enough for it to decompose the hydrocarbon. The material will then grow on top of the catalyst material in the reactor.[3]

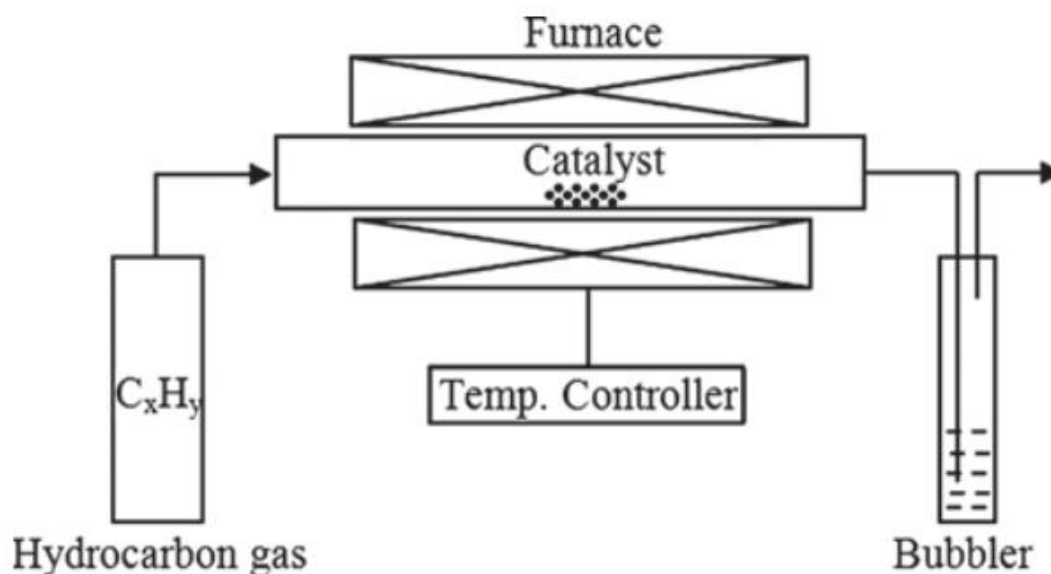


Fig 1.1 - Example of a simple CVD setup [2]

This method is a low cost and easily scalable method that yields the best compromise between quantity, quality and cost, which is one of the main reasons for being widely accepted as the most viable option at the moment. However, the high temperatures that the sputtered metal film is subjected to can lead to unstable states that are unsuited for the growth of CNTs. This can lead to inconsistent results in the diameter of the tubes, where the top may be narrower than the bottom and affect the density of the forests of tubes. It can also define whether the CNTs are single or multi walled, which have different properties, and as such different applications [4]

In the case of graphene growth, several processes exist. In dry exfoliation processes graphene is obtained by splitting layered materials into atomically thin sheets via mechanical, electrostatic or electromagnetic forces in air, vacuum or inert environments. One process associated with dry exfoliating is anodic bonding, where graphite is pressed against a glass substrate. After a high voltage is applied to the graphite and the glass is heated a few layers of graphene form on top of the glass, which is then cleaved off. This is possible as graphite is essentially several layers of graphene stacked on top of each other. The quantity of graphene obtained is controlled by the voltage and the temperature applied, both in size and in number of layers

Liquid-phase exfoliating is also possible, and the process is similar to dry exfoliating except it is performed in liquid environments. It can be divided in three steps: the dispersion of graphite in a solvent, exfoliation, and purification. The purification step consists in ultracentrifugating the mixture in order to separate exfoliated flakes from un-exfoliated flakes.[5]

In order to name but a few of the many processes, we will lastly mention graphene growth by CVD as the process is the same as the one described above for CNT growth.

Graphene growth is heterogenous, starting at impurities or defects in the substrate, like edges of steps in the surface. It then grows into islands by adsorbing carbon species from the surface that then diffuse to the edge of the graphene sheet. Graphene growth is then dependent on high concentrations of carbon in the metal surface.

Another important factor to consider is the morphology of the substrate. As mentioned before, graphene growth starts at the impurities of the substrate's surface. In metals, which are very common substrates for the process, the surface contains atomic-high steps otherwise known as imperfections. However, graphene's ability to grow in surface impurities allow it to develop into defect-free islands that span spaces bigger than any defect-free space on the surface. The surface of the metal may, however, change during growth which can cause problems for graphene growth. For example, submitting copper substrates to high temperatures, such as the ones in CVD that are very close to the melting point of copper, leads to the sublimation and subsequently to step edge retraction. In these cases, the sublimation is slowed in regions where copper is trapped under grown graphene, but this leads to the creation of mounds and the roughening of the topography.[6]

Nonetheless, copper is a very popular substrate for graphene growth as it is cheap, available in large sizes and easily dissolvable, which makes for easy graphene collection. Its main advantage over other metals is its low carbon solubility, allowing for the carbon deposited in its surface to grow into graphene instead of growing by segregation during the cooling period after CVD, thus providing a

monolayer of graphene under optimized growth conditions. Even under non-optimized conditions, copper catalysts normally provide a few layers of graphene, thanks to the low carbon solubility in copper, which is unique among other common metal catalysts. It should be noted that, before CVD, copper is usually submitted to heat treatment with argon/hydrogen that clean the impurities and augment grain size which has an impact of graphene growth as clean and smooth copper surfaces make for better graphene.

Another important fact to note is that thinner films of copper may enter a dewetting state, where holes form and grow in the thin film due to instabilities, at which point graphene growth is not possible as the film no longer has the large and smooth surfaces that are required for graphene growth. One way to prevent this from occurring is to keep the copper films' thickness above 500nm. Despite this, dewetting can be used as a method to deposit the graphene on top of the SiO₂/Si substrate, however we must ensure that the film does not dewet before the graphene is fully grown.[7]

The temperatures required for the CVD process can also pose problems to the stability of copper films as they and the copper's melting point are very close. To this end, other metals such as molybdenum have been used as substitutes of copper due to their higher melting point, which make for more stable films at higher temperatures.

It is, then, very important to have stable and clean surfaces to produce graphene with good properties. However, materials evolve during processes, and the high temperatures at which the thin films are subjected to during CVD cause stresses and instabilities, like dewetting, that can compromise the surface on top of which the graphene is growing. It is then important to study how the film behaves under these conditions to how they affect the graphene growth process.

2. Literature Review

Thin films are subjected to stresses during their deposition and during the processes that they are submitted to. In the following chapter, we will look into how the instabilities influence the film's integrity and how different stresses affect the film.

2.1-The Dewetting Process

The dewetting process is a consequence of the instabilities of the catalyst material. It consists in the formation of "islands" of agglomerated material when metastable thin films are heated up to high temperatures (Fig 2.1), and in the case of films formed through vapor deposition where the atoms have a limited range of movement as they come in contact with the substrate surface leading to nonequilibrium structures. As per Thompson [8], this reaction comes mainly through the minimization of the total energy of the free surfaces of the film and substrate and their interface. As such, the rate of dewetting increases along with the decrease in film thickness, and, conversely, the temperature at which dewetting starts occurring rises as film thickness increases. The process can have various originating factors, ranging from pinholes that already exist between the grains of the film to the creation of new holes during the deposition.

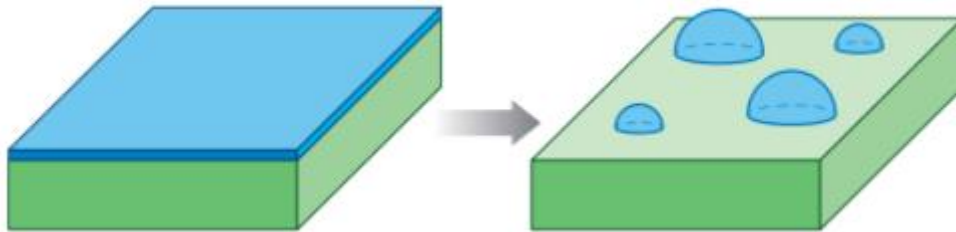


Fig 2.1 - Schematic example of thin film dewetting[8]

So, a way to understand the stability of a film post-deposition is to study its capillary energies and the strain it is subjected to. With the help of the Young-Laplace equation, we can determine if a film is stable or not and as such, whether or not it will dewet. The equation is as follows:

$$\gamma_s = \gamma_i + \gamma_f \cos \theta \quad (2.1)$$

where γ_s is the surface energy per area of the substrate, γ_f is the surface energy per area of the islands formed during dewetting, γ_i is the energy of the substrate-island interface and θ is the equilibrium contact angle, which refers to angle between the substrate and the curvature of the island when the particle stabilizes. For $\gamma_s > \gamma_i + \gamma_f$, the film is considered to be stable and thus does not dewet.

The dewetting process can be divided into 3 steps: Hole formation, hole growth, and impingement. [8]

2.1.1- Hole formation in the thin film

Let's then start by understanding why holes form in an otherwise flat surface in polycrystalline films. Thin films are usually considered stable as long as the amplitude of the perturbations, as in defects in the flatness of the film, that affect them are smaller than the thickness of the film. This means that if the holes are not as deep as the thickness of the film it can still be considered stable. With this we can conclude that the defects in the film can lead to the formation of holes in the film that in turn cause the dewetting process to start.

Srolovitz & Safran [9] studied the stability of a thin film through the variation of capillary energies, basing their work on the Rayleigh-Plateau instability [10] and Mullins' study on the stability of the surface of cylinders for small perturbations [11], to develop a model that showcased the evolution of perturbations of thin films.

Their conclusions were that infinitesimally small holes will decay and restore uniformness to the thin film, but if the hole is large enough then it grows until it reaches its equilibrium size, which is reached when the curvature of the film's edge is equal to the equilibrium contact angle between the film and the substrate. The behaviour of the holes can be determined according to the composite parameter, β , which is determined by the following function:

$$\beta = \left(\frac{R}{h}\right)^2 \left(1 + \frac{\gamma_s}{\gamma_f}\right) \quad (2.2)$$

Where R is the radius of the system and h is the thickness of the film. For large values of β the holes in the film will grow, showing that hole growth increases with the energy of the interface of the film and the substrate as well as the ratio of the area of the system relative to the thickness of the film.

They also observed that, in polycrystalline films, grain boundary grooves and triple grain junctions, where three grain boundaries meet the film's surface, were possible physical origins for holes.

In the case of grain boundaries, a groove forms where the grain meets the free surface and at equilibrium the angle between the grain boundary and the free surface is the equilibrium notch angle φ which is given by:

$$\varphi = \sin^{-1} \left(\frac{\gamma_G}{2\gamma_f}\right) \quad (2.3)$$

where γ_G is the surface energy at the grain boundary. The depth of the groove is defined by:

$$\delta = R \frac{2 - 3 \cos \phi + \cos^3 \phi}{3 \sin^3 \phi} \quad (2.4)$$

When the depth of the notch exceeds the thickness of the film, the groove will intercept the substrate and the film separates into islands. The same happens for triple junction boundaries, but the grooves are deeper which means that these are more likely to develop into a hole.

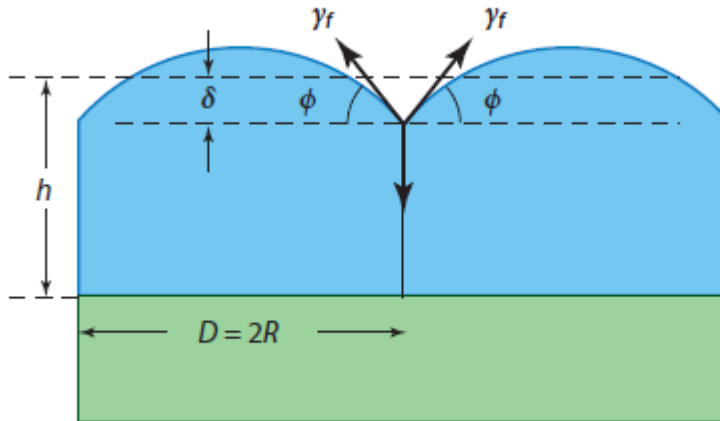


Fig 2.2 - Schematic representation of grain boundary grooves[8]

Besides the development of physical attributes of the film, the stresses present in the film and substrate can cause holes to form. One of the manifestations of the effects of stress is the appearance of blisters at the film's surface usually caused by the creation of voids at the interface of the film and the substrate. This can occur when the film adheres poorly to the substrate's surface, for example Au and Pt films on Si [12]. The blister will grow until it pops, creating a hole that then expands [13]. This is due to differences in the compressive stresses the film and the substrate experience when they come into contact. [8]

Another way stress affects hole formation is through grain thinning, where the films relaxes and relieves compressive stress during heating by forming hillocks. This is caused by the difference of the thermal expansion coefficients of the film and the substrate, leading to the development of tensile stresses during the cooling process. These tensile stresses can then be responsible for the formation of holes near the hillocks.

According to Thompson [8], for a film with pre-existing holes and with no formation of new holes, the dewetting rate will depend on the number of holes and the rate of hole growth. However, if a kinetic process, such as groove deepening, is needed to cause hole formation then the overall dewetting rate is influenced by both hole growth and hole formation rates. For cases where new holes besides the preexisting ones grow, a hole nucleation rate should be included in the overall dewetting rate.

Hole formation rate scales according to:

$$\dot{N} \propto \frac{h^4}{D_s} \quad (2.5)$$

Where h is the film thickness and D_s is the film's surface diffusivity. The time for hole formation will however vary for different groove boundaries and triple junctions as it is dependant on the surface energies of the local interface.

2.1.2- Hole growth

As observed by Srolovitz & Safran [9], once the hole has formed it will continue to grow until it reaches stability. Capillary energies will drive the growth of the hole through the retraction of its edge, which means that the rate of hole growth is related to the rate at which the edge retracts.

The retraction phenomenon is characterized by a flux of material coming from through the triple line, the line where the film is in contact simultaneously with air and the substrate, over the edge to the flat surface of the film around the hole. This flow of material causes the retraction of the edge of the hole, which in turn causes it to grow.

As the edge keeps retracting, material starts to accumulate and forms a rim around the hole higher than the thickness of the film. This happens because of the high curvature of near edge, as opposed to the low curvature near the film surface. The flux J is defined by the following equation:

$$J = - \left(\frac{D_s \gamma_s N_s \Omega}{k_B T} \right) \nabla_s k \quad (2.6)$$

where $\nabla_s k$ is the surface gradient of the surface curvature, D_s is the surface diffusivity, N_s is the number of surface atoms per area, Ω is the atomic volume, k_B is Boltzmann's constant, T is temperature.

As the edge curvature starts to reduce, the driving force for the mass flow also reduces, making for a lower edge retraction rate at this stage. This was first observed by Brandon & Bradshaw [14].

With the height increase of the rim, a valley starts to form where there used to be a stable film surface. This valley becomes shallower as the rim height increases until it reaches a point where the substrate becomes visible and the rim detaches from the rest of the film, a process which is called rim pinch-off. Now that the rim is independent from the film, a new hole is formed and the process of edge

retraction and rim pinch-off begins again for this new hole (Fig 2.3). The fact that this process keeps repeating itself is crucial to determining the rate of edge retraction as the speed varies at different stages of the process, it is faster at the beginning when the rim is starting to form but slows down as the valley gets shallower until it repeats again after the pinch-off.

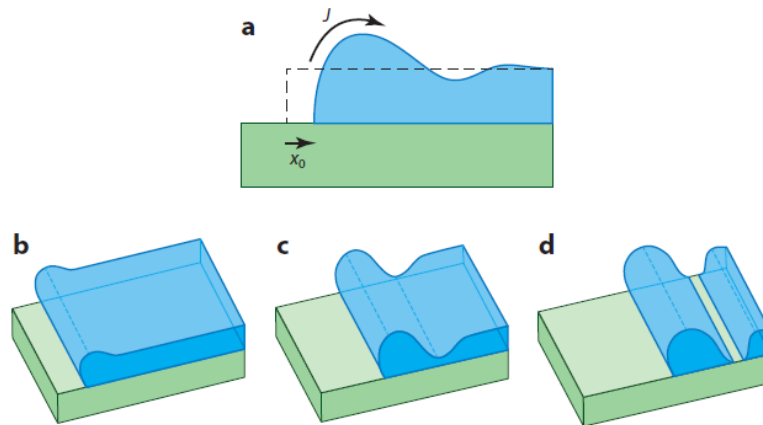


Fig 2.3 - Schematic representation of edge retraction and subsequent pinch-off[8]

While holes tend to retain a circular shape when they grow, they may break up into finger shapes (Fig 2.4) and then into islands if the number of growing holes is low and as such holes grow without meeting other holes. According to Jiran & Thompson [13], this happens because the rim becomes unstable, and Srolovitz & Safran [9] suggested the break-up could be owed to a Rayleigh instability. The process remains similar to the pinch-off, where the rim, which now has a cylindrical or finger shape, continues to retract until it detaches and eventually becomes an island.

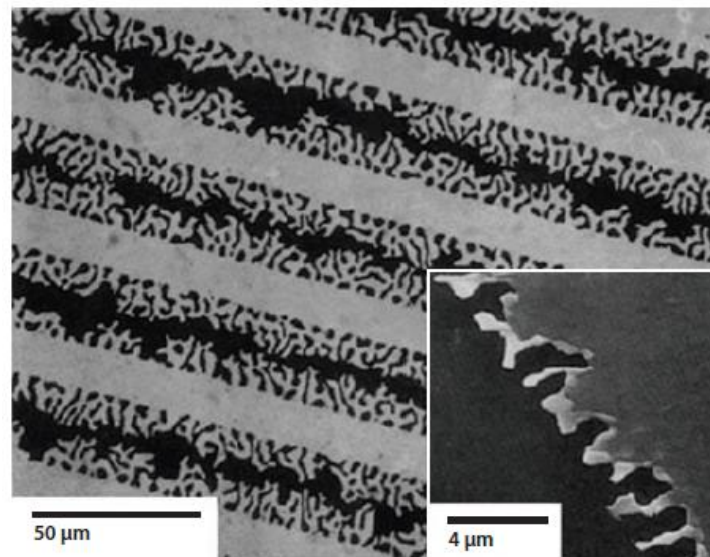


Fig 2.4 - Image of fingering instabilities in an Au film[8]

As discussed before, rims develop into strands after pinch-off or fingering. These strands have cylindrical shapes and the evolution of their radii, referred to as r_{strand} , scales with the film thickness

during the late stages of dewetting, according to Thompson [8]. The cylinders are unstable because of radial perturbations and end up breaking up into spherical caps, as suggested by the Rayleigh instability. Their radius scales accordingly to the radius of the cylinder r_C and the time for spheroidization evolves according to:

$$t_{Rayleigh} \propto \frac{r_C^4}{D_s} \quad (2.7)$$

As indicated previously, the edge retraction rate can vary according to the stage of process, and as such approximations and scaling relationships are different for various stages. However, Wong et al. [15] determined the overall rate, by averaging many pinch-off cycles, to scale according to:

$$\dot{x}_0 \propto h^{-3} \quad (2.8)$$

where \dot{x}_0 is the edge retraction rate and h is film thickness. This is valid for cycles without fingering instabilities.

In that case, Jiran & Thompson [13] found that the rim velocity was constant and scaled as:

$$\dot{x}_0 \propto D_s h^{-3} \quad (2.9)$$

where D_s is the surface diffusivity of the film.

According to Thompson [8], most models suggest that the edge of the film should retract according to:

$$x_0 \propto t^n \quad (2.10)$$

where t is the time and n is a coefficient that changes for different models. As mentioned before, the edge retraction is linear for fingered fronts and as such in those cases $n = 1$. The same condition applies for cases where the pinch-off process is repeated, as we are dealing with average rates. However, when applying models to a film that has yet to undergo either pinch-off or to develop instabilities then $n \in [0,4; 0,5]$.

2.1.3-Overall dewetting rate

According to Thompson [8] and as seen previously, the overall dewetting rate is governed by a series of kinetic processes. Firstly, the pre-existing holes in the film, N , must grow or there is an incubation time, τ , in order to enable holes to form through groove deepening. New holes may continue to form during the process at a rate of \dot{N} . Then, during hole growth, the edges retract at a rate \dot{x}_0 to form the dewetted areas and the holes impinge until the substrate is visible through most of the thin film. The dewetting process will continue in the strands that will decompose into spherical caps because of the Rayleigh instability.

The overall dewetting rate can be described by relating the nucleation rate and growth of dewetted areas to the rate of transformation of total area of the film. As such, the dewetted area X_{dewet} before impingement is given by the following:

$$(X_{dewet})_{preimpingement} = \int_{\tau}^t 2\pi \dot{x}_0^2 \dot{N}(t - t') dt' \quad (2.11)$$

where τ is the time at which holes start to appear. Total true dewetted area, after impingement and as dewetted areas start to overlap, is:

$$X_{dewet} = 1 - \exp(-(X_{Dewet})_{preimpingement}) \quad (2.12)$$

Jiran & Thompson [13] applied this approach in their experiments and found that, apart from a limited number of holes that appeared afterwards, all holes formed during the incubation time τ , making the number of holes after incubation approximately N . By neglecting the time for strand spheroidization and by assuming that \dot{x}_0 remained constant, they also assumed that the overall area of dewetting scaled according to:

$$\dot{X}_{Dewet} \propto \frac{\exp\left(\frac{-Q_s}{kT_{dewet}}\right)}{h^3} t \quad (2.13)$$

where Q_s is the activation energy for surface self-diffusion, and T_{dewet} is the temperature.

2.1.4- Single-crystal films

Single-crystal films are also affected by dewetting when subjected to elevated temperatures, with the process being very similar to the polycrystalline films. According to Thompson [8], the phenomenon also requires pre-existing holes or defects in the film's surface to initialize hole formation, with the main candidates being pinholes, impurities that can react and make the film discontinuous, and defects that cause pit formation and topographical irregularities on the substrate's surface, but no clear mechanism for hole formation has yet been identified. However, unlike polycrystalline films, single-crystal films are strongly affected by their uniform crystallography during hole growth, and this is seen in the shape of the holes and in the shape of the fingers that develop in the process (Fig 2.5).

Thompson [8] reviewed the case of Ni films where the holes grew into square or rectangular shapes. As they continued to grow, the material accumulation formed faceted rims on the edges and corners that continue to grow in height and width. Like in polycrystalline films, the growth of the rims mean that the retraction rate starts to slow down, however, the rim grows faster at the edges than it does in the corners of the hole, implying that the retraction rates of the corners is faster than that of the edges. This difference leads to the change of the shape of the hole.

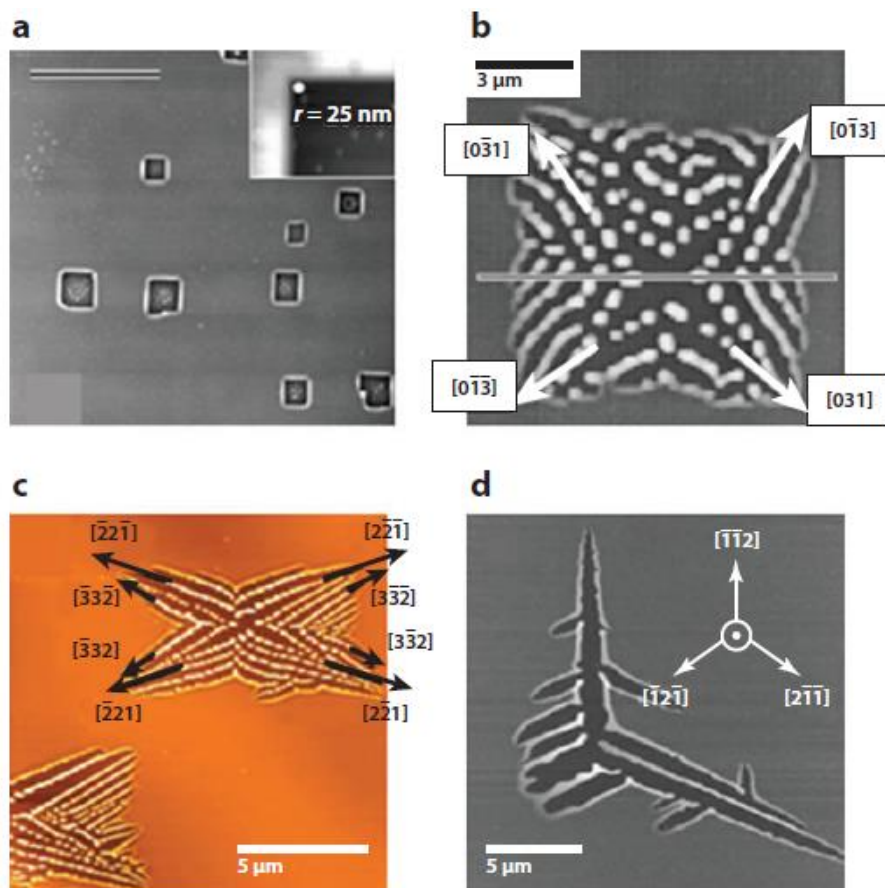


Fig 2.5 - Images of growing holes in Si films[8]

As well as changing the shape of the hole, the higher retraction rate of the corners of the hole allows for fingering instabilities to develop along the edges, which in turn can lead to strand formation

through pinch-off processes. As with polycrystalline films, these strands tend to break-up due to Rayleigh-Plateau-like instabilities and transform into beads spread across the substrate, though Thompson [8] suggests the rate of break-up depends of the crystallographic orientation of the axis of the strand.

2.1.5 - Controlling dewetting

In Leroy et al's short review [16], the authors discuss several methods to control both the island distribution and the kinetics of dewetting.

Being able to control the layout of the islanding process is useful in cases where a controlled shape, size and distribution is needed. This can be achieved by altering different parameters of the film or the processes to which the film is subjected.

For controlling island size and density several approaches are presented. By varying the film's thickness h it is possible to obtain different island sizes and densities. According to Leroy [16], the size scales with h , while density varies following h^{-2} .

It is also possible to control both parameters by changing the temperature at which the process takes place. By increasing the temperature, the dewetting rate raises and creates defects in the fingers formed during dewetting. This means that for higher temperatures the island size is smaller and the density increases. However, it is not possible to vary the temperatures often as they are limited by restrictions imposed by the reaction.

Another factor to consider is strain. Borowik et al [17] conducted tests on SOI where they concluded that Si islands formed on strained silicon samples resulted in smaller islands and higher density when compared to samples without strain.

Borowik et al [17] also investigated the impact of contaminant layers on top of the film. They observed that the higher the contamination of carbon on top of the film the smaller the islands would be and the higher the density of the islands. They also found that the contaminant layer lowered the dewetting rate.

Leroy also mentions ionic bombardment as way to control size and density. By subjecting the film to ionic before annealing defects are created at the films surface. This means that the island density is higher since defects in the film's surface are prone to hole formation, and the longer the bombardment the higher the density of islands.

Aside from controlling the size and density of the islands, it is also possible to control the disposition of the islands during dewetting.

One solution for this is to practice templated dewetting. It consists in patterning the substrate to obtain self-organized dewetting structures which can be achieved by one of three ways. In the first one, natural surface topography, monoatomic steps and facets are used to drag preferential island formation. The second one, lithographed substrates, uses artificially patterned substrates to correlate the dewetting to the topography. It is mainly used for metallic films and has the advantage of allowing for void guidance through substrate modulation which in turn allows for dewetting zones to grow coherently. The third way,

patterned films, which consists in patterning the film as opposed to the patterning of the substrate in lithographed substrates. This method allows for a better localization and distribution of the islands. According to Leroy, these three methods are very promising ways to control the size and distribution of dewetted islands.

Controlling dewetting kinetic is also very important. One way to do so is by inhibiting dewetting through chemical reactivity. Curiotto et al [18] showed that active oxydation inhibited dewetting and that it was a reversible phenomenon as stopping oxygen injection allow dewetting to start again at the same rate.

The dewetting process is then a process that is heavily influenced by the thickness of the film and the amplitude of the perturbations at its surface, as the number of holes that form and how they grow is strongly influenced by those two factors. The edge retraction driven by surface tension instabilities makes for an inhospitable environment for graphene to grow and as such must be prevented. The overall dewetting rate is also influenced by the temperature, with Thompson [8] suggesting that films with higher melting points be used to prevent dewetting.

Techniques like active oxydation that inhibit the dewetting process can help to prevent the rupture of the film before the graphene growth process is completed. Other solutions, like templated dewetting are useful for growing other materials like CNTs where having a predictable arrangement of islands helps obtaining more consistent diameters in the tubes.

2.2-Stresses in thin films

While the dewetting process can be critical for graphene growth, the stresses that affect thin films also cause problems to the growth. These stresses can lead to elastic deformation of the film, impair its mechanical stability and adherence to the substrate, or modify its properties [19] which could hamper the necessities of flat, smooth ground for good graphene growth.

Two different stresses will be reviewed, intrinsic stresses that originate in the vaporization of the metal on top of the substrate and thermal stresses that cause biaxial stresses to develop during heat cycles.

2.2.1-Intrinsic stresses

Intrinsic stresses are stresses that are not induced by applied loads or by the differential of thermal coefficients. These stresses originate during the vaporization of the film, also known as sputtering, as a condition of the atomic arrangement as they are deposited on the substrate. At the start of the process, the unconstrained particles grow under compressive stress. This is due to the interface surface stresses between the particle and the substrate. This can be characterized by an equation derived from Laplace's equation:

$$\Delta p = \frac{2f}{R} \quad (2.14)$$

Where Δp is the mechanical action of the surface, f is the surface stress at the interface and R is the radius of the particle. The sign of f determines whether the stress is tensile or compressive, and in the case of small islands the stress tends to be compressive [20].

As material continues to be deposited on top of the substrate the islands continue to grow. At this point we have a dynamic surface in which the arriving atoms form layers and ledges. When the deposition stops a change in the direction of the force per width makes the stress less compressive, allowing the surface to relax by surface diffusion, and likely reducing the number of ledges. The number of ledges is an important factor in the surface stress since the higher the number of ledges the higher the stress, compressive or tensile.

As the islands continue to grow, they eventually coalesce and form a continuous film that induce a tensile stress. After this point there are two different developments that depend on the material being deposited. For high-mobility materials, the atoms that continue to be deposited on top of the film will diffuse to the grain edges and relax the tensile stress, and the only part of the film that remains in tensile stress is the part that was already present before the coalescence. This leads to an average stress that becomes compressive during cooling. On the other hand, low-mobility films will be under increasing tensile stress as the atoms that arrive will not diffuse and as such maintain the tensile stress that was established before coalescence. The evolution of the stress state of the film is represented in the generic graphic below, showing the difference between low and high-mobility materials after island coalescence (Fig 2.6).

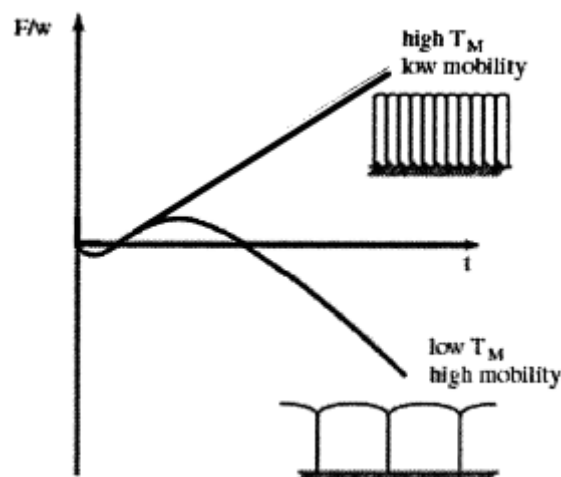


Fig 2.6 - Generic diagram of the evolution of Force per width over time for high and low mobility materials[20]

In the case of a perfect film deposited on top of a perfect substrate, without imperfections, biaxial stresses cannot cause delamination. However, when there are imperfections in the substrate the film can detach from the surface. In the case of tensile stresses, the film would start to peel from the edges as shear stresses may appear at the film/substrate interface. Similarly, compressive stresses can cause the film to buckle and detach due to shear stresses caused by dips and humps on the surface of the substrate.[19]

2.2.2- Thermal stresses

Thermal stresses and strains originate from the difference in the thermal coefficients of the film and the substrate. This causes a stress defined by:

$$\sigma_{thermal} = -E(\alpha_f - \alpha_s)(T - T_0) \quad (2.15)$$

Where E is the film's Young's Modulus, α_f and α_s are the thermal expansion coefficients of the film and substrate respectively, and T and T_0 are the current temperature and the initial temperature at which the film and the substrate were in a stress-free state. In the example below (Fig 2.7) [21], we observe the results of a heating cycle of an aluminum thin film that has been annealed several times to stabilize the intrinsic stresses.

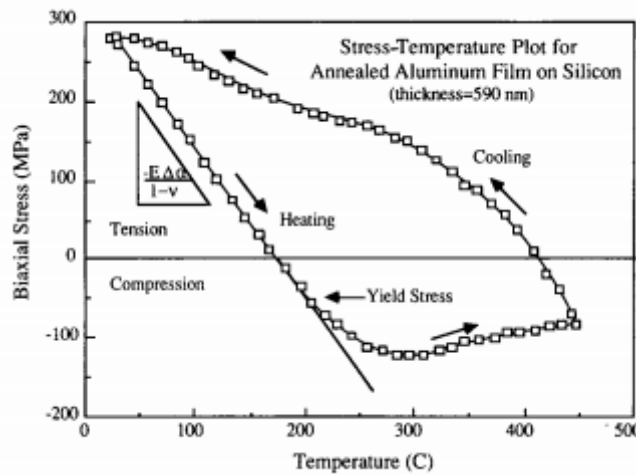


Fig 2.7 - Stress-temperature plot for an Al film on a Si substrate [22]

At the start, at room temperature, the film is under tensile stress. As it is heated, the stress relaxes, accommodated by elastic deformation, until it starts to compress. The heating process continues and the compression stress reaches the film's yield point, after which it starts to deform plastically. The compressive stress peaks at its maximum value before starting to drop. After reaching maximum temperature, the cooling process begins and the film relaxes until it is no longer under compressive stress. As the cooling process advances, tensile stresses develop in the film until it reaches room temperature, causing plastic deformation to occur.

While this plot (Fig 2.7) was obtained through the heat cycle of aluminium, most metal films deposited on silicon exhibit the same behaviour as the one described above. In the case above, the film had already been through several heat cycle. In the diagram below (Fig 2.8), the effect of a heat cycle on an as-deposited film can be observed.

The film starts under biaxial tension, like the previous scenario. However, as the temperature rises and the stresses become compressive, the film relaxes rapidly at around 225°C as the compressive stresses reach their highest value. Unlike the previous scenario, this is not due to the plastic deformation

of the film, it is caused by densification, or grain growth. Grains in as-deposited films are unstable and this causes them to grow when heated up to a size comparable to the thickness of the film. The film then cools down normally, returning to its original state of tensile stress, though the stress is higher than at the beginning. This is due to the densification process that causes a structural transformation in the film. After the first heat-cycle the film structure doesn't change anymore and the stress-temperature curves are similar in subsequent heat-cycles [21].

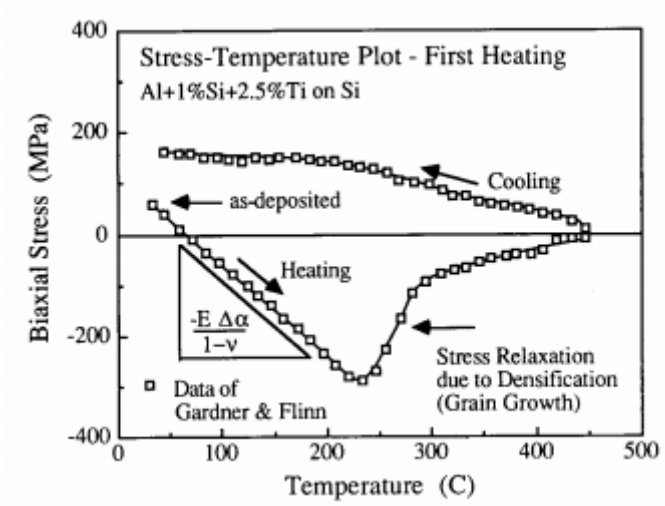


Fig 2.8 - Stress-Temperature plot for a film (Al+1%Si+2.5%Ti) on Si as-deposited heat-cycle[21]

As said previously, stresses in thin films can have different effects in the film. In the two specific situations described here we came across two different scenarios: in one the film failed to adhere properly to the substrate due to shear stresses developing in imperfections of the surface, with the biaxial stresses causing the film to peel or buckle according to the stress applied. In another situation, the effect of thermal strains on the film was examined, and it showed that they caused unstable, as-deposited films to alter their granular structure during a heat-cycle.

3. Methodology

3.1-Geometry

In order to be able to study the stresses and strains exerted on the thin film during the CVD process, the Abaqus software was used to recreate this situation with a virtual model. The finite element method on which Abaqus is based is used to approximate partial differential equations in order to simulate real world conditions. To do this, the model converts mathematical equations into matrix models that can be approximated through nodes and elements that make for simpler problems to solve [22].

The model consists of a representation of the three-layer assembly (Fig 3.1) as it is typically used as a basis for the graphene to grow on top of. The bottom layer is made from silicon, above it sits a layer of silicon dioxide and the top layer is a thin film of copper, the dimensions of which are based on the experimental apparatus at International Iberian Nanotechnology Laboratory (INL). It was decided that four thicknesses (900nm, 480nm, 120nm and 30nm) would be represented in this study. The image below (Fig 3.1) intends to show in a clearer fashion how our model has been laid out.

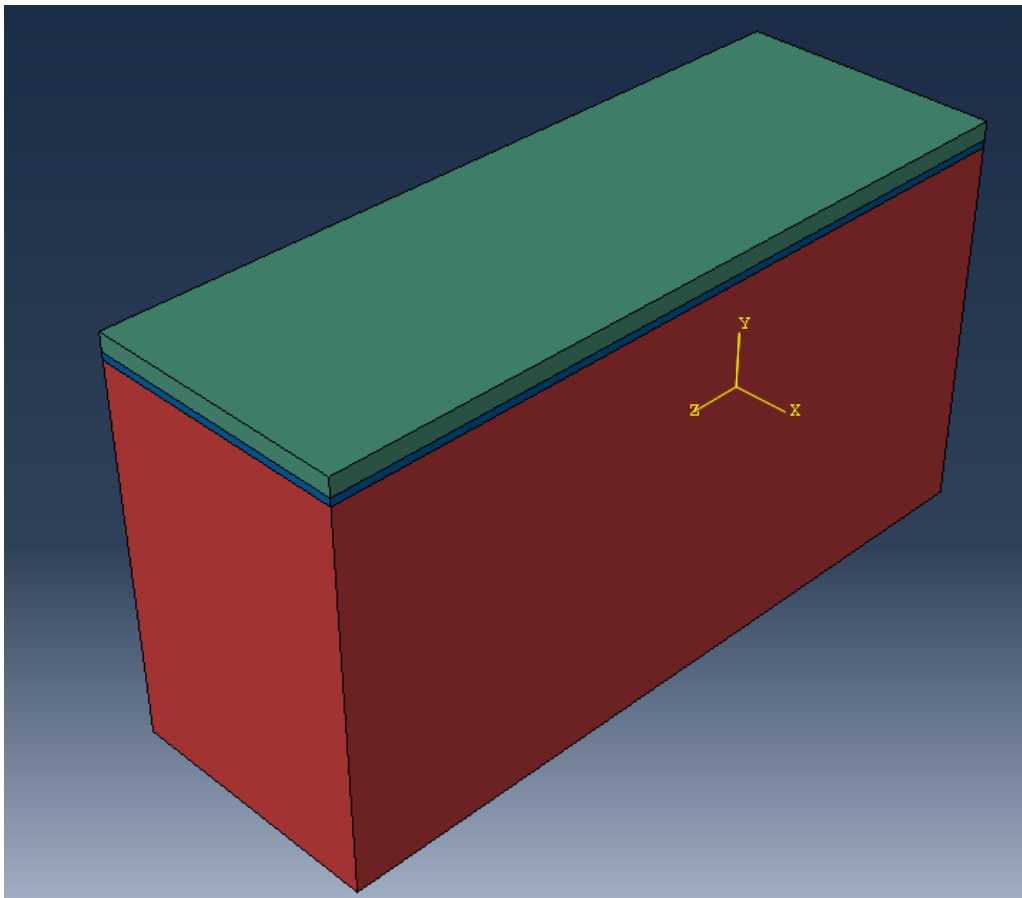


Fig 3.1 - Assembly of a thin copper film atop a SiO_2 and Si substrate

Besides these three layers, a very thin (3nm) layer of tantalum can be used to promote adhesion between the thin film and the SiO_2 layer. However, since in our model these two layers share nodes at

their boundaries, there is no chance of separation. As such, the tantalum layer was not included in this model but it is understood that there could be an interest in evaluating its impact on the stresses and strains caused during the process.

The height of the bottom silicon layer was also shortened from $800\mu\text{m}$ to $10\mu\text{m}$. Having a layer with very big dimensions was a downside in terms of visualization of the model due to its difference in size to the other two layers, but also in terms of computation as it would drastically increase the number of elements in our model, which would in turn increase the time needed by the machine to complete a model analysis. Taking into account a study made by Fidalgo [23], it was decided to represent only $10\mu\text{m}$ of silicon to still have a visually indicative difference between the three layers (Fig 3.2).

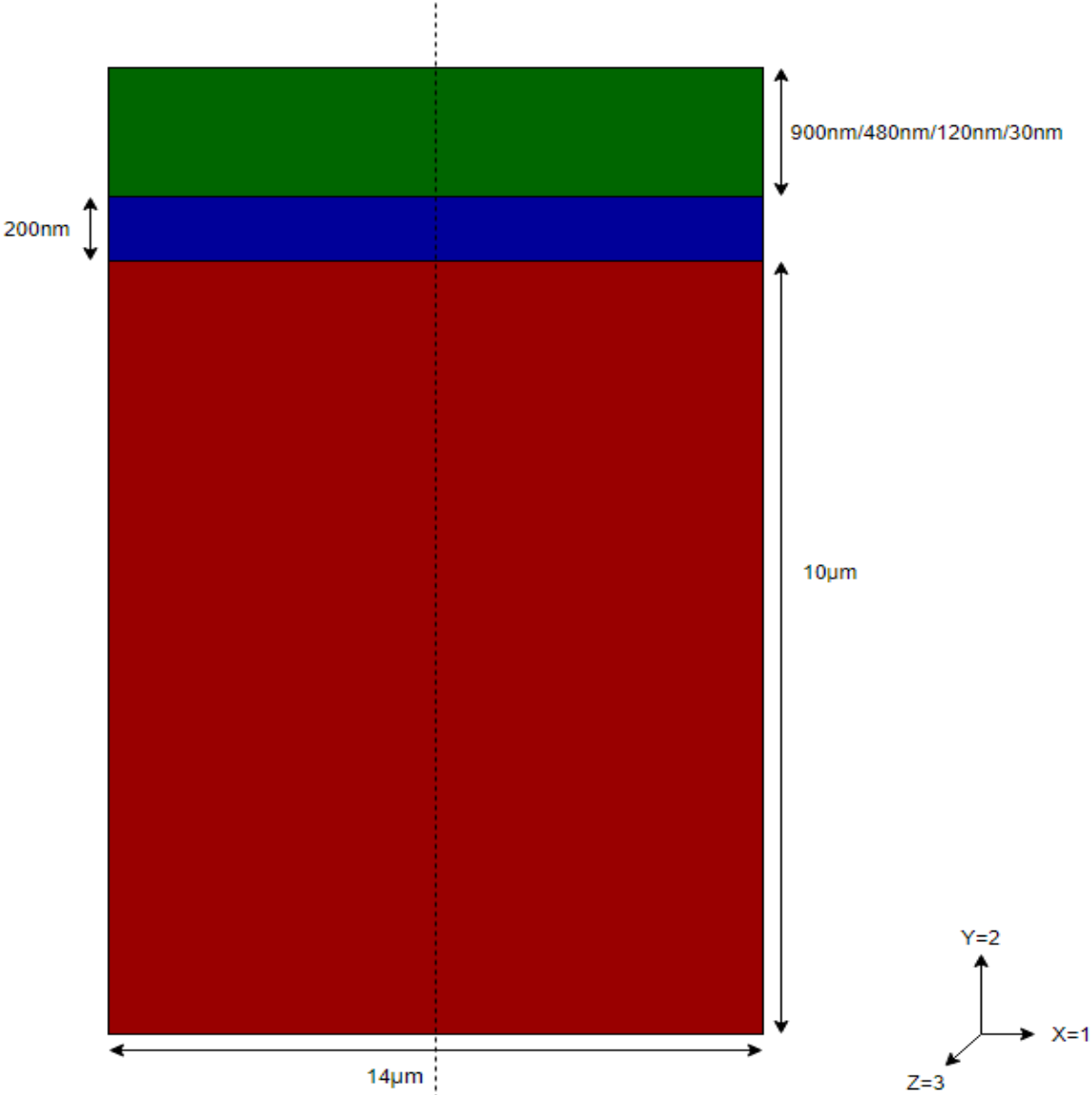


Fig 3.2 - Schematic of the bidimensional model

The bigger part of our analysis has been conducted in a bidimensional model in order to minimize the computational demands. As this is not representative of reality, a second model in three dimensions was also developed to confirm the results obtained in the bidimensional model. Thus, our three-dimensional model has the same geometric conditions as the bidimensional one. What was changed was the length of the assembly, along the z-axis, with four different lengths (5 μ m, 10 μ m, 20 μ m and 40 μ m) to see how this would impact the behaviour of the thin film. Two thicknesses of the thin film were modelled (120nm and 480nm) at two different temperatures (250°C and 500°C).

3.2 - Dimensional analysis

As Abaqus is a dimensionless software, it is up to its user to determine the base units that fit best into their model. There is also a limitation of the software that only allows a difference of 10^5 between the largest and the smallest part in the model, for example, if SI units were to be kept the smallest part we could model would have to be at least 10 μ m in any direction. Since the layers of materials are between 10 μ m and 30 μ m, it was established that the base unit would be the micrometre.

However, this implies that any value input into the software that uses SI units needs to be converted to make sense within the model. A table that shows how the various properties are affected can be found in the appendix. [23]

3.3- Material Properties

In this model only the thin film atop the assembly would be able to plastically deform, with the silicon and silicon dioxide layers below remaining in elastic conditions throughout the cycle. The fact that both the silicon and the silicon dioxide are brittle materials, along with the fact that little information is easily available about their material properties at very high temperatures such as the ones observed during the CVD process, led to the decision of not implementing plastic behaviour for these two materials.

A recreation of the stress-strain curve of the material was needed to implement the plasticity of the thin film. As the information for detailed stress-strain curves at higher temperatures is not abundant in the available literature, the stress-strain curves of the material of the thin film were reconstructed with two points: the yield stress and ultimate stress for a given temperature, the ultimate stress being recorded for the maximum plastic strain and the yield stress when plastic strain is 0, as can be seen in the figure below (Fig 3.3).

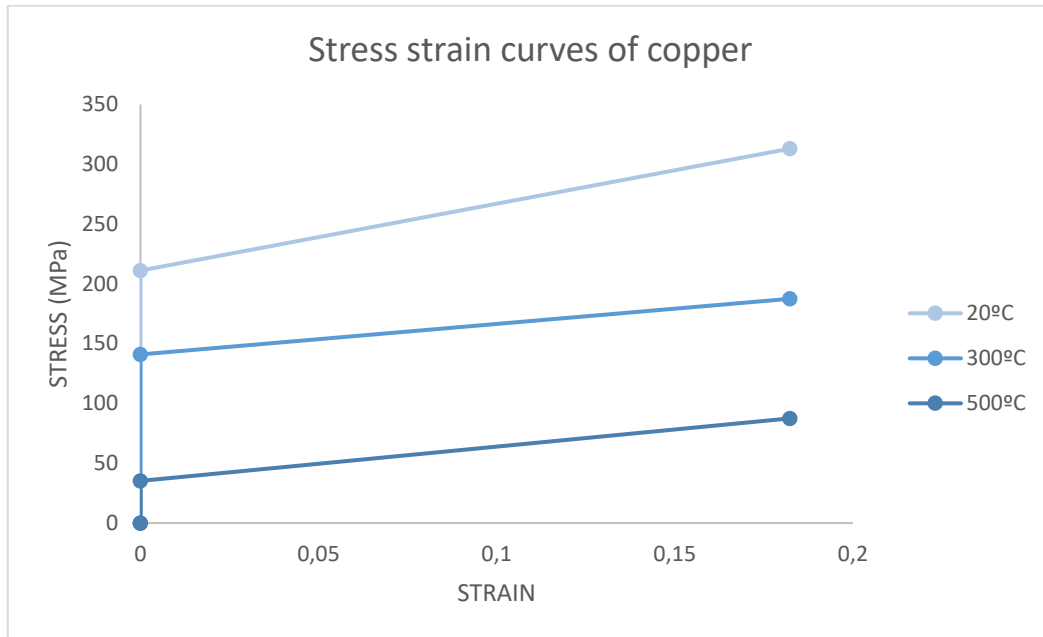


Fig 3.3 - Example of the stress-strain curves used for the model

When working with Abaqus, the user must ensure that the material properties entered into the model are in line with what the software requires. In this case, the values of yield and ultimate stress for the materials in the thin film needed to be properly inserted as Abaqus deals with true stress and true strain values. As such, engineering stress and strain needed to be converted into true stress and strain. This is done through the following equations:

$$\sigma' = \sigma(1 + e) \quad (3.1)$$

$$\varepsilon = \ln(1 + e) \quad (3.2)$$

Hooke's law was used to then deduce the value of true plastic strain, which is required by Abaqus:

$$\varepsilon_{elastic} = \sigma' / E \quad (3.3)$$

$$\varepsilon_{plastic} = \varepsilon_{total} - \sigma' / E \quad (3.4)$$

Since the available data didn't cover the whole range of temperatures needed for this study, a part of the information required needed to be generated. As such, Arrhenius' law [24] was used to extrapolate the values for the yield and ultimate stress at the temperatures that were lacking these values.

$$\sigma(T(K)) = \sigma_0 \exp\left(-\frac{q}{RT(K)}\right) \quad (3.5)$$

After the extrapolation of all the properties needed for the model, the following tables contain all the information regarding material properties:

Table 3.1 - Mechanical properties for the materials used in the model

Copper			
Temperature (°C)	σ_y (MPa)	σ_u (MPa)	ϵ at break
20	211,08	313,03	22%
100	206	287,5	22%
200	196	250	22%
300	141	187,5	22%
400	85,4	125	22%
500	35,2	87,5	22%
600	10,1	37,5	22%
700	3,72	19,1	22%
800	1,65	11,1	22%
900	0,84	7,03	22%
1000	0,48	4,79	22%
Young's Modulus (GPa)		Poisson's	α (x10 ⁻⁶)
128		0,35	16,90

EXTRAPOLATED WITH ARRHENIUS' LAW

Molybdenum			
Temperature (°C)	σ_y (MPa)	σ_u (MPa)	ϵ at break
27	330	791,892	18%
127	315,35	756,804	18%
327	295	708,528	18%
427	282,59	678,204	18%
527	264,79	637,92	18%
627	245	586,692	18%
727	212,6	525,636	18%
927	160,6	385,728	18%
1227	80	191,004	18%
1300	70,3	167,6	18%
1400	60,1	142,8	18%
1500	52,2	123,9	18%
Young's Modulus (GPa)		Poisson's	α (x10 ⁻⁶)
330		0,38	5,20

EXTRAPOLATED WITH ARRHENIUS' LAW

SiO2		
Young's Modulus (GPa)	Poisson's	α (x10 ⁻⁶)
74,8	0,19	0,75

Si		
Young's Modulus (GPa)	Poisson's	α (x10 ⁻⁶)
186,5	0,28	2,6

The copper mechanical properties were sourced from CES13 Edupack [25], while the yield and ultimate stresses came from Karditsas and Baptiste [26]. The molybdenum properties were sourced from AZO materials' website [27], and the yield and ultimate stresses were sourced from the same study as the copper's [26]. Finally, the silicon dioxide properties were sourced from AZO materials' website [28], and the silicon properties were sourced from EL-CAT Inc. website [29].

Two materials were modelled for the thin film, one being copper which is the preferred material when growing graphene as described previously. However, it is prone to dewetting in thinner films at the temperatures necessary for the CVD procedure. As such, molybdenum was suggested as an alternative for comparison, as its higher melting temperature indicates that it might be in a more stable state at the temperatures at which copper starts to dewet.

3.4-Thermal load and boundary conditions

During the CVD process, the assembly is submitted to very high temperatures to enable the reaction between the carbon precursor and the thin film on top to occur. As such, the increase in temperature was divided into two steps for our model. In the first one, the assembly is heated up from room temperature (25°C) to one of four peak temperatures: 250°C, 500°C, 750°C or 900°C, with the latter being the temperature at which the film would be during the CVD process. This decision was taken as problems regarding the stability of the thin copper film arise at high temperatures and as such breaking down the increase of temperature into smaller intervals would allow us to see if there are any

changes in the behaviour of the film that might give us any indication of that. Following the increase of temperature, the assembly is then brought back to room temperature in a second step.

Both steps have the same duration of 1 unit of time which could be viewed as 1 second as the finite element approach is in this case time independent and viscoplastic and stress relaxation effects were not taken into account in this model. These however are relevant to this matter and could be the target of future works. This is true for both the bidimensional and three-dimensional study. The figure below (Fig 3.5) illustrates the evolution of temperature during the process.

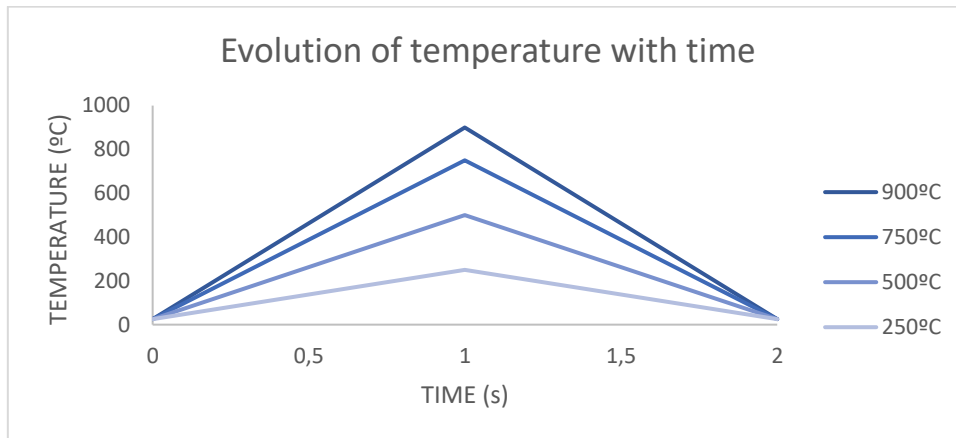


Fig 3.4 - Evolution of temperature with time

For the boundary conditions there is a distinction between the 2D and the 3D models. For the former, the assembly is pinned in the bottom extremities to prevent any movement, while leaving the top of the assembly free. A symmetry condition was also implemented with a plane perpendicular to the X-axis, across the centre (Fig 3.6). This allows to save on computational requirements as only half of the assembly needs to be rendered, and if needed, a representation with the full width could be created with the mirror tool in the software.

For the three-dimensional model, the pinning condition is extended along the bottom edges with the same goal of keeping the bottom of the assembly from moving while leaving the top free to deform, and the symmetry condition along the X-axis remains. However, in a further effort to keep the computational requirements down another symmetry condition was added, this time perpendicular to Z-axis at the halfway length. The image below aims to provide a clearer picture of the restrictions explained above.

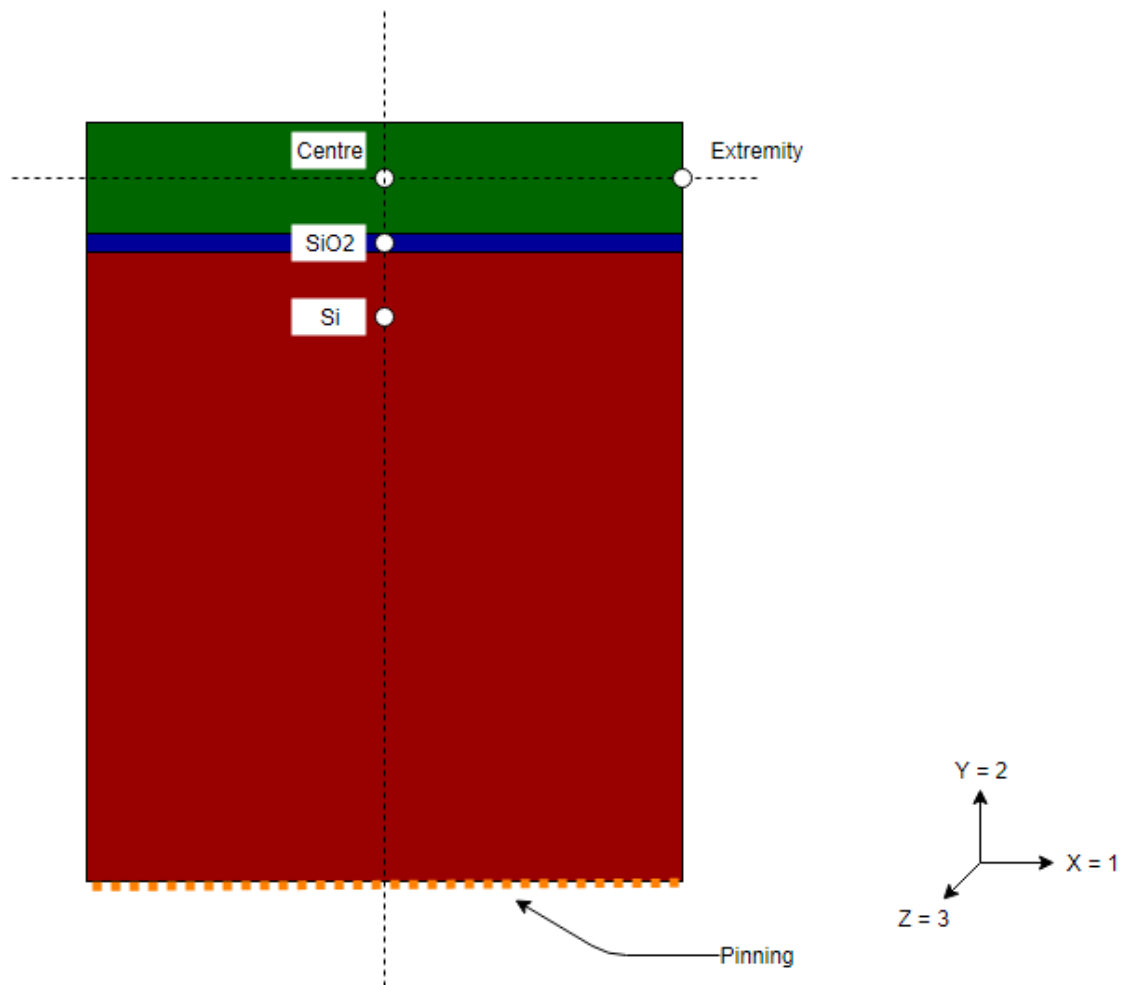


Fig 3.5 - Schematic of the boundary conditions applied to the model

3.5- Convergence Studies

In a Finite Element method study, the further the number of elements are increased in the model to represent the subject, the more consistent is the outcome of the simulation. However, the greater number of elements implies a greater computational demand of the machine the simulation is running on as the number of equations it has solve can increase drastically. As such, the user needs to find a balance between the consistency of the result and the computational capacity of the machine he is using, meaning that one would usually try to find the point at which the results of a simulation are within a reasonable margin of error while remaining within the computational margins of the machine, and apply those results to the study.

3.5.1- Bidimensional model

For this model, an assembly that consisted of the Si and SiO₂ layers with a 900nm thin film of copper on top, which was heated up to 250°C and then cooled down to room temperature was studied to see how the results varied with the changes in element count. Von Mises stress, as an indicator of the overall stress in the model, and the deformation of the assembly were considered as criteria for the

convergence study and data was gathered at four different points in the model. The previous image (Fig 3.5) used to represent the boundary conditions also contains the data gathering points.

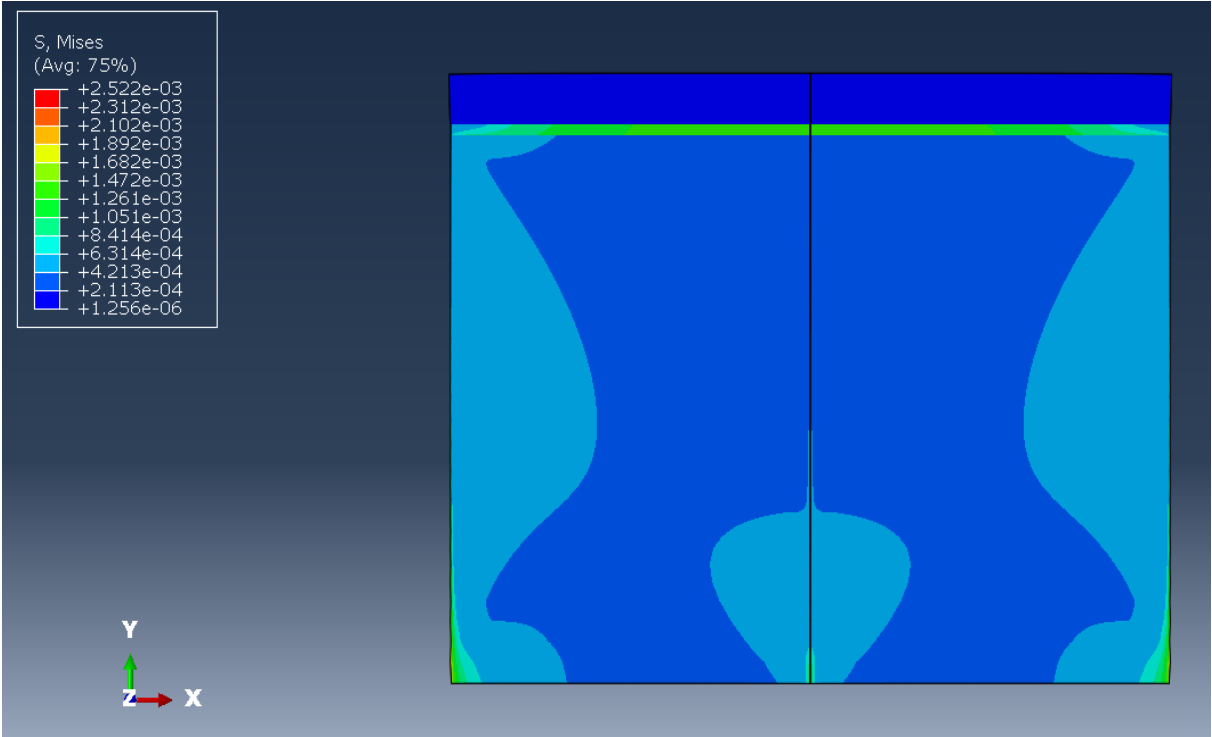


Fig 3.6 - von Mises stress in a bidimensional model at the end of the heating phase at 900°C (Stress in TPa)

The results showed that the model has very consistent results from a very low number of elements up to 1 000 000 elements (Fig 3.7 and Fig 3.8). As the geometry is very simple, this was expected. However, with a very high number of elements in the model the simulation times become very high. When refining the mesh, it was verified that von Mises stress results changed less than 0,5% and displacement results changed less than 2% from 300 000 elements and upwards. As such a compromise was sought, ensuring that every layer had at least 5 elements in its thickness to allow for good deformation, while using single bias seeding on the edges of the silicon layer which helped to keep the element count manageable. This reasoning was applied to all the models in the studies for the four different thicknesses and the two different materials used.

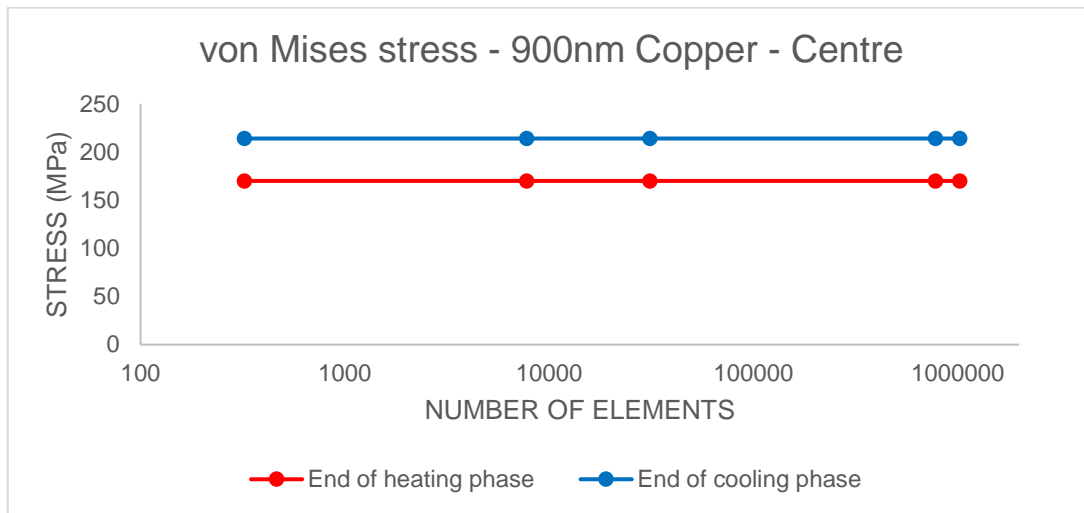


Fig 3.7 – Convergence study for von Mises stress at the centre for a bidimensional model

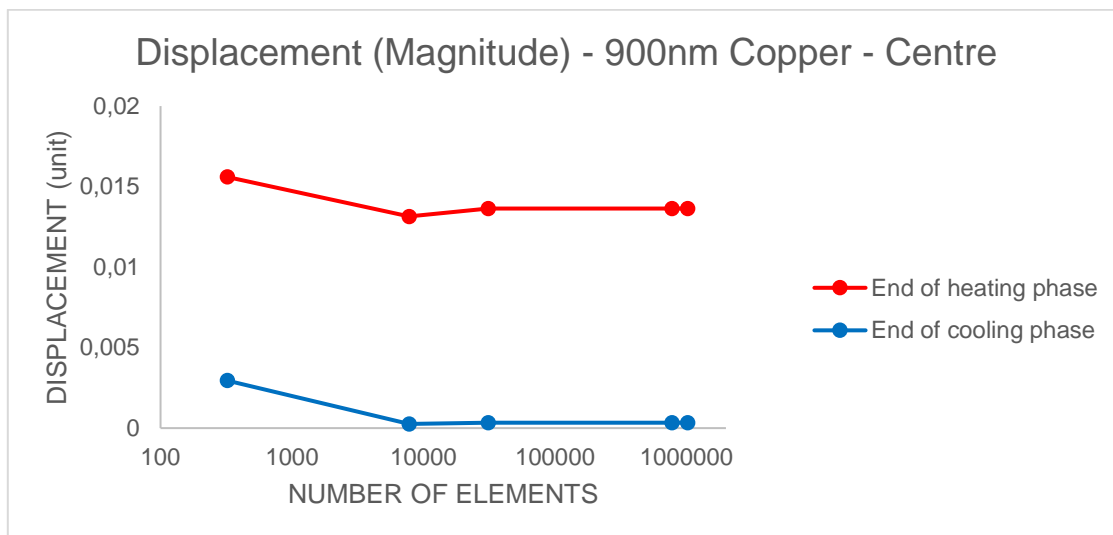


Fig 3.8 – Convergence study for displacement at the centre for a bidimensional model

The results for the remaining data points are in the appendix section of this document.

3.5.2- Three-dimensional model

The convergence study for the 3D models is very much based on what had been previously done in 2D space, following the same approach as before with the added consideration for the length of the assembly. As such, the study consisted of a 20µm long assembly of the three-layer model, with a 900nm thick film on the top. The decision to go for a 20µm long assembly came from the necessity to establish a baseline for the difference in computational demand when going from a bidimensional model to a three dimensional one.

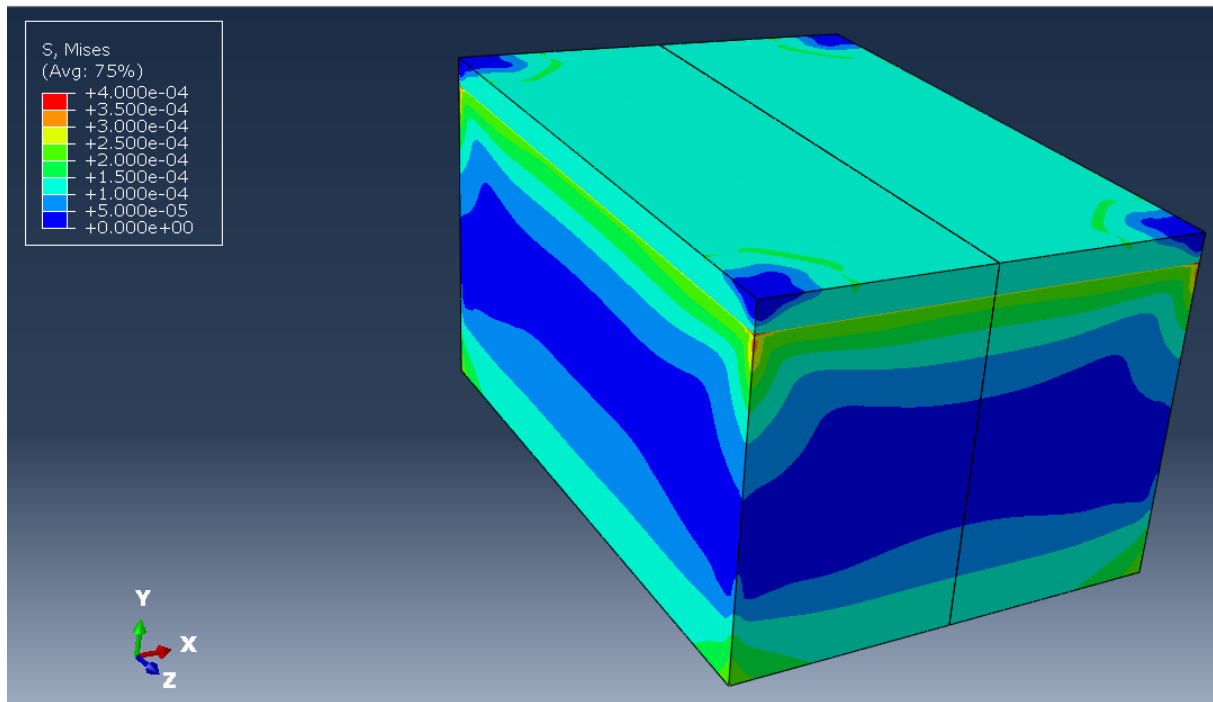


Fig 3.9 – von Mises stress in a three-dimensional model at the end of the heating phase at 250°C. Stress in TPa

The results were similar to what was observed for the two-dimensional model, with the only difference being on the SiO₂ where a shift can be observed at around 100 000 elements. This is due to the fact that up until that point, the seed value, which indicates the size of an element, did not allow for a SiO₂ layer with more than one element in thickness. However, to have a result that would be in line with what was determined for the 2D study, the five element thickness rule needed to be kept, but this meant that the computational requirements would be even higher, as would be the solving times.

The solution to this was to fix the thickness of the elements to ensure that every layer would have at least five by specifying a different seed value to the edges of each layer and setting the global seed, that would then be responsible for the width of our elements, to a value that would be manageable for our models. Additionally, single biased seeding was used on the edges of the bottom silicon layer to further ensure that computational requirements were kept down. The following figures show the results at the centre of the film (Fig 3.10 and Fig 3.11)

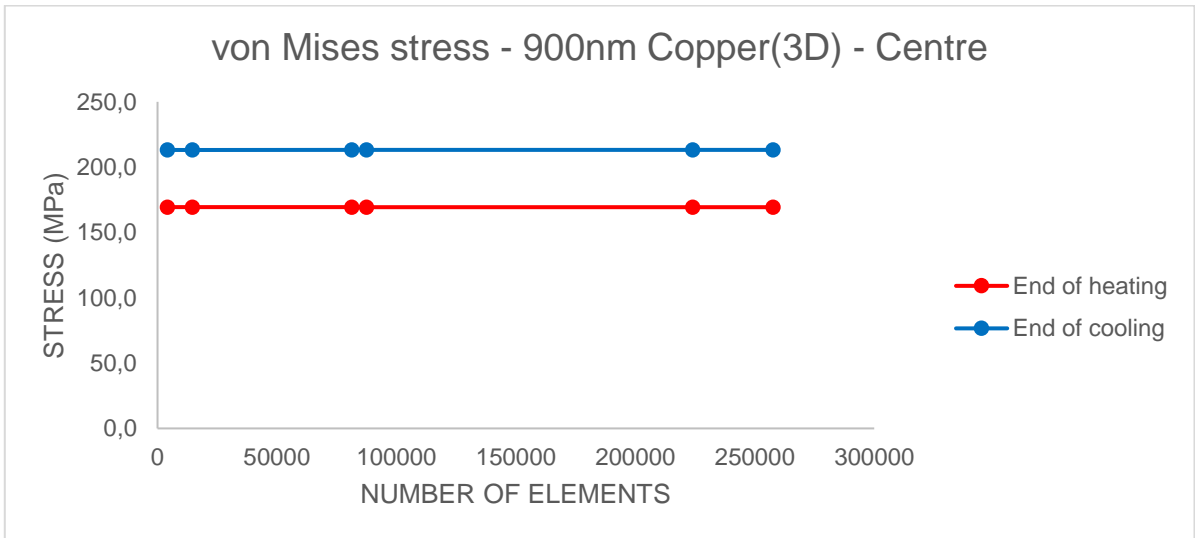


Fig 3.10 – Convergence study for von Mises stress at the centre for a three-dimensional model

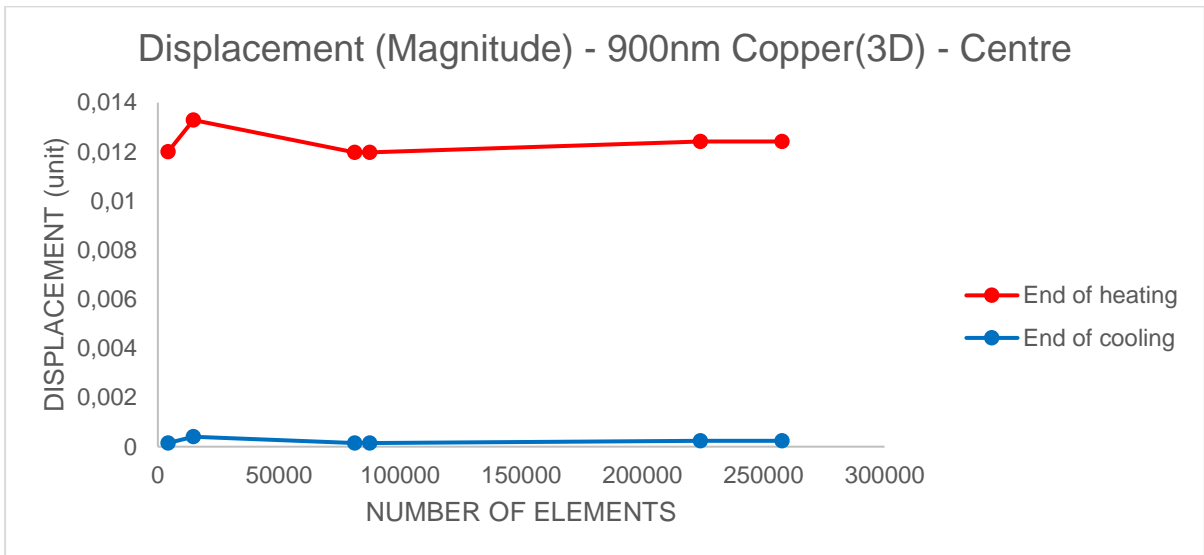


Fig 3.11 – Convergence study for displacement at the centre for a three-dimensional model

As with the bidimensional study, the rest of the results of the various data gathering points is in the annex.

3.6 - Assumptions

Aside from the simplifications that have been mentioned before in this section, the following assumptions were made for this model:

- Initial stresses from the material deposition were not taken into account. While they are an important feature to consider, we can take this study as an extreme case on which annealing cycles have been performed in order to reduce residual stresses to a minimum.
- The system was only submitted to a thermal load, so no other loads were applied.
- Isotropic behaviour is considered for all materials in this system, as crystal orientation was not taken into consideration and as such the materials behave identically at any point and in any direction in their layer.
- For the bidimensional models, plane strain conditions were assumed where strains outside of the XY-plane are not considered:

$$\varepsilon_{xz} = \varepsilon_{yz} = \varepsilon_{zz} = 0 \quad (3.6)$$

4. Results

4.1 Bidimensional study

As to prevent excessively complex sentences when describing the different cycles, they will be referred as A, B, C, and D, with each one corresponding to the 250°C, 500°C, 750°C and 900°C peak temperatures respectively. This information is also indicated in the various plots that will accompany this section.

4.1.1 - Copper films

Von Mises stress is often used for ductile materials and metals as a criterion to indicate whether a material has reached its yield stress, and thus is deforming plastically, as it encompasses the three main stress components and the shear stresses, giving a general view of the stress levels that the system is under.

$$\sigma_{VM} = \sqrt{\frac{(S_{11} - S_{22})^2 + (S_{22} - S_{33})^2 + (S_{11} - S_{33})^2 + 6(S_{12}^2 + S_{23}^2 + S_{13}^2)}{2}} \quad (4.1)$$

Beginning with thicker 900nm copper film, von Mises stress (Fig 4.1 and Fig 4.2) shows that the stress levels in the film rise with the increase in temperature until they reach the yield stress value, at which point they gradually lower until the cycle reaches its peak temperature. As the film cools back down to room temperature, the stress curve follows the same path as it did when the film was heating up but with the difference that the stress levels keep climbing as the temperature passes the point where the film reached its yield stress. For cycle A, with a peak temperature of 250°C, the stress levels dip steeply as the cooling process begins before climbing back again and following the same curve as the cycles with higher peak temperatures when approaching room temperature.

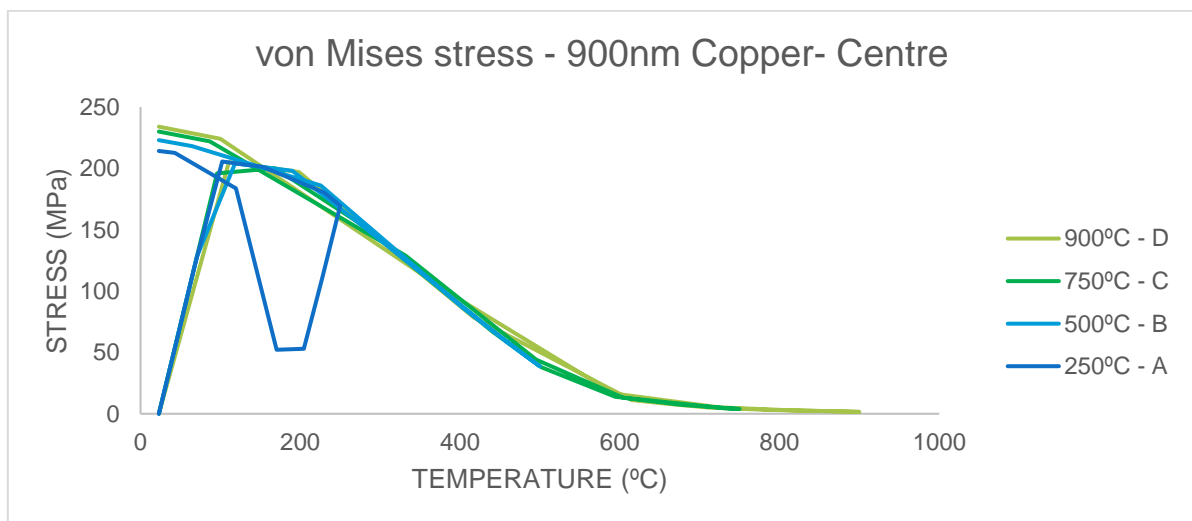


Fig 4.1 - Von Mises stress at the centre of a 900nm copper film

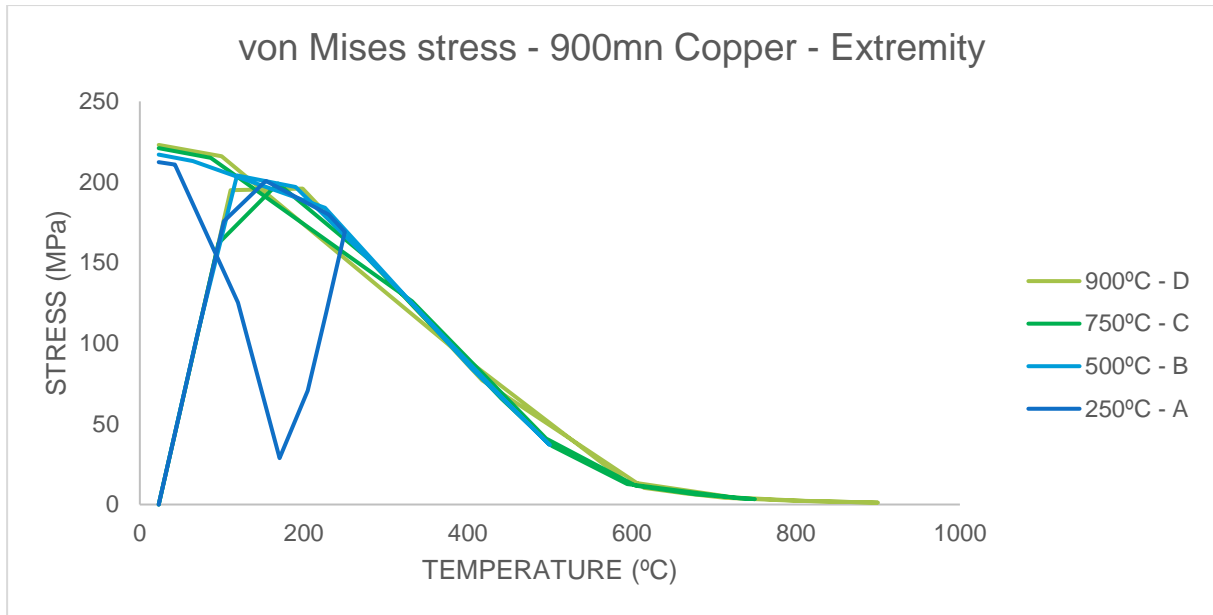


Fig 4.2 - Von Mises stress at the extremity of a 900nm copper film

Looking at the various components of stress, it is visible that the sources for the values that we see in the von Mises graphs are the S11 (Fig 4.3) and S33 (Fig 4.4), along the X-axis and Z-axis respectively, while the results for S22 and S12, along the Y-axis and in the XY plane, are very low in comparison and even sometimes approximately zero.

In both S11 and S33 the trend that was observed in the von Mises stress appears, with the stress levels rising with the temperature until they reach the yield stress value and coming down to approximately zero after that. The plots of both stress components also show that the film is under compressive for the heating part of the cycle and then transitions into tensile stress as the cooling phase beings.

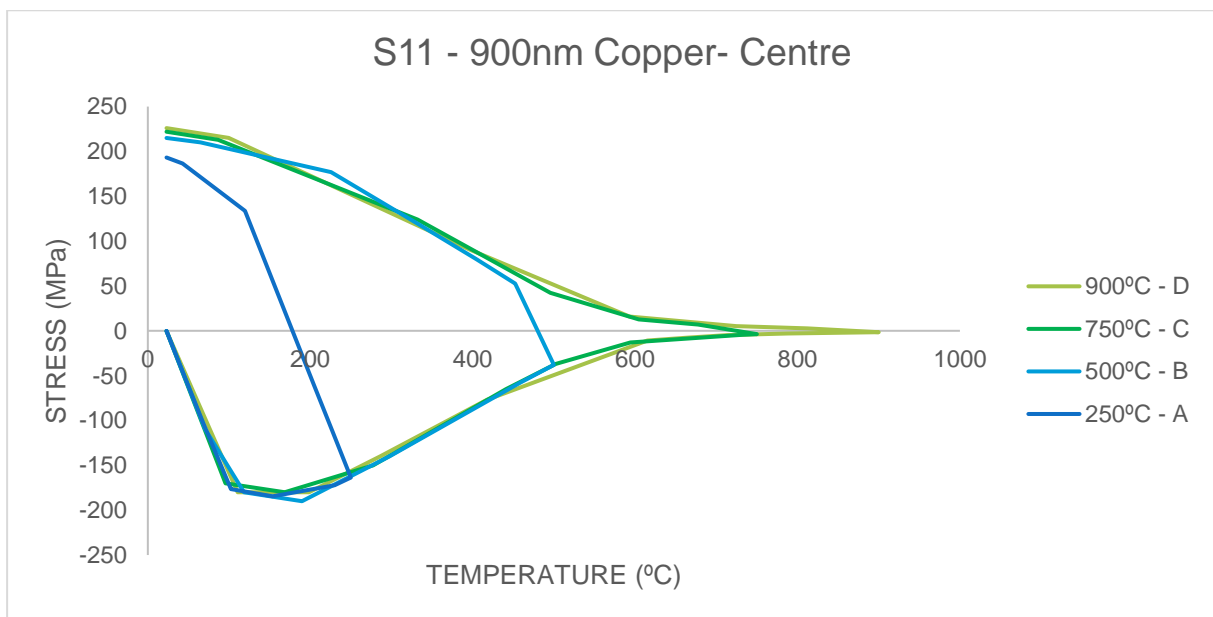


Fig 4.3 - S11 stress at the centre of a 900nm copper film

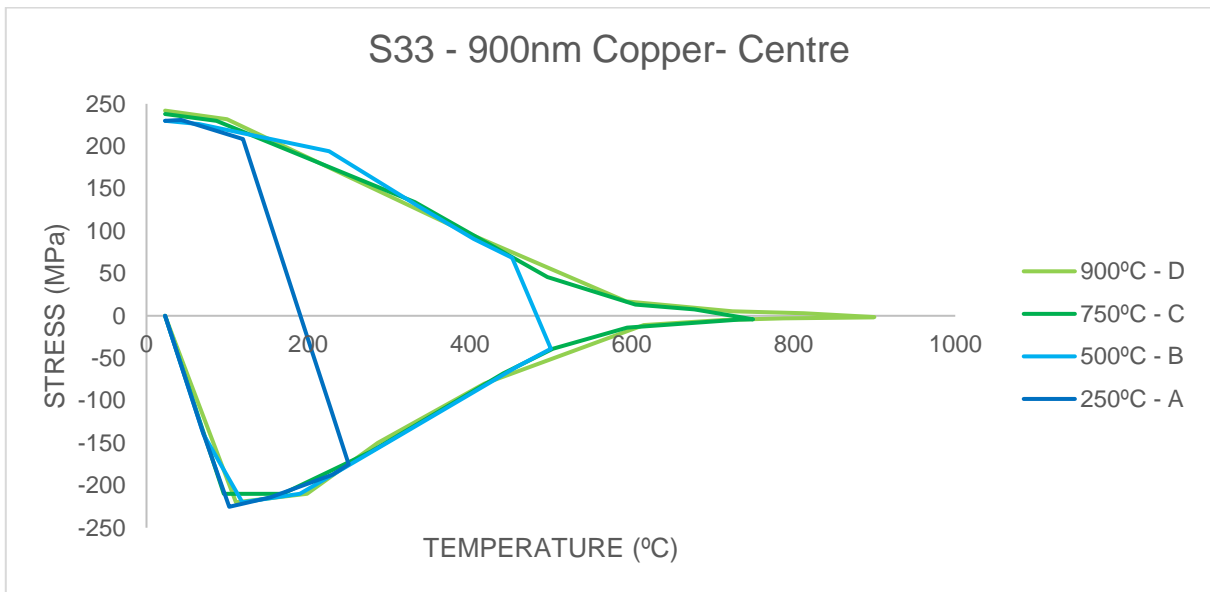


Fig 4.4 - S33 stress at the centre of a 900nm copper film

While it would be expected to see the stress values to rise as the temperatures keep rising since thermal stress increases with the increase of the temperature difference from room temperature, as per equation 2.15, the results show the opposite. This is because the yield stress value of the material decreases as it gets closer to melting temperature. By plotting the results of von Mises stress against the curve obtained from the evolution of yield stress with the increase in temperature (Fig 4.5) we see that the yield stress acts as a sort of filter that prevents the stress levels from rising indefinitely.

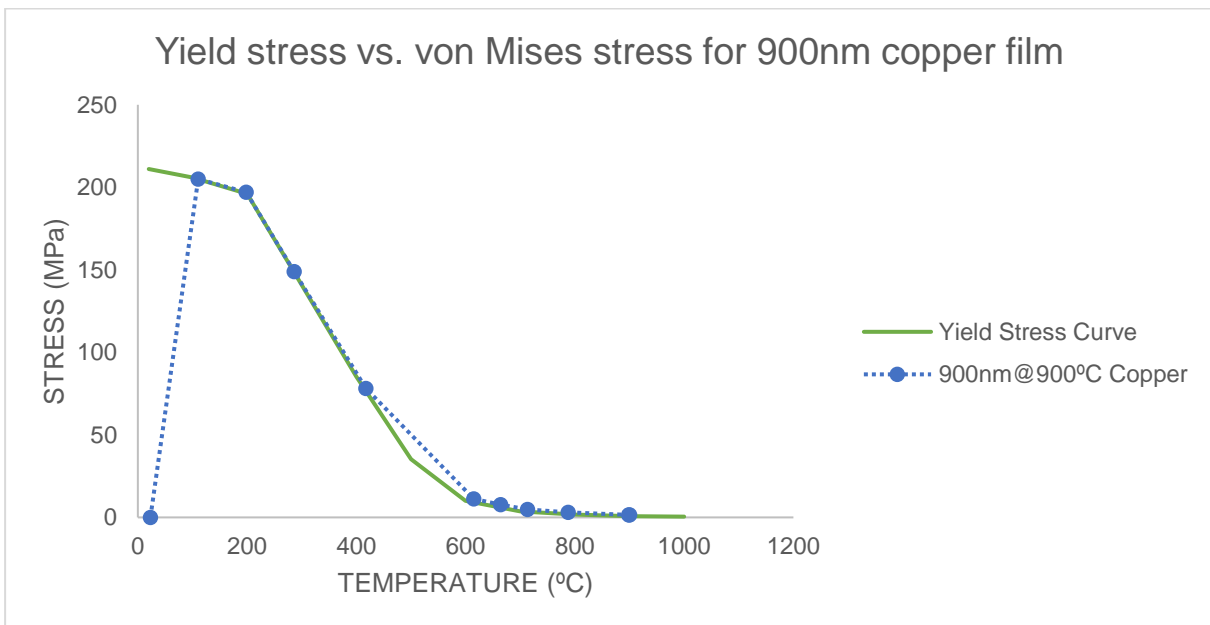


Fig 4.5 - Evolution of yield stress with temperature and comparison with von Mises stress from 900nm copper film

The plastic strain results (Fig 4.6) show a continuous increase in plastic strain levels as the temperature rises as well as identical values for residual plastic strain at the end of the thermal cycle.

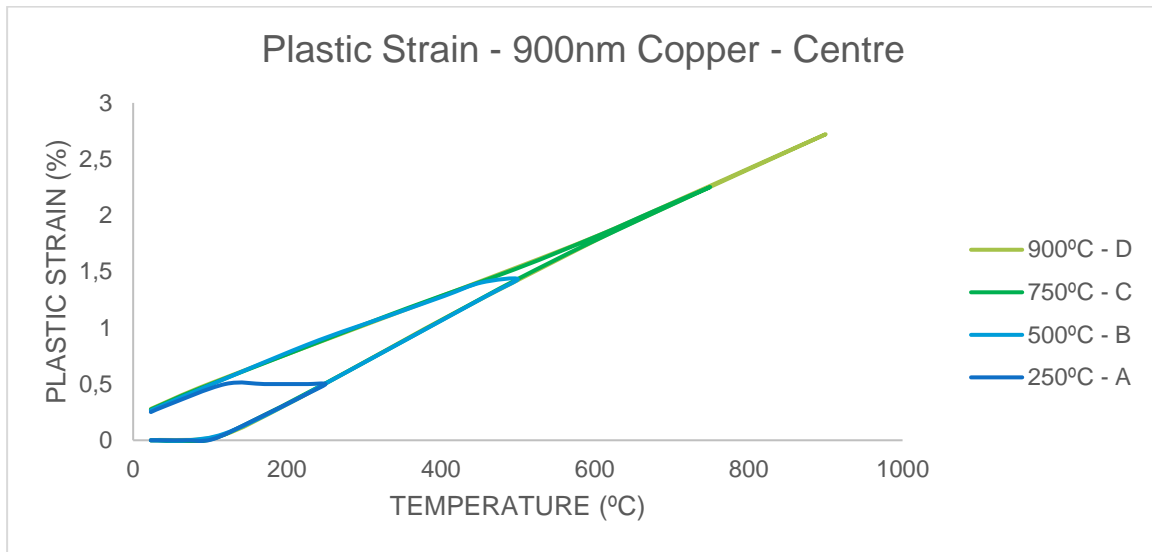


Fig 4.6 - Plastic strain at the centre of a 900nm copper film

The plastic strain plots also show that for cycle A there is a plateau as the film enters the cooling stage before coming back down as the temperatures approach room temperature. This can be related with the comparison between the von Mises stress and yield stresses (Fig 4.7) again, where the film transitions from plastic into elastic deformation for the initial stages of cooling before starting to plastically deform again, signalled by the values that are joined again to the yield stress curve.

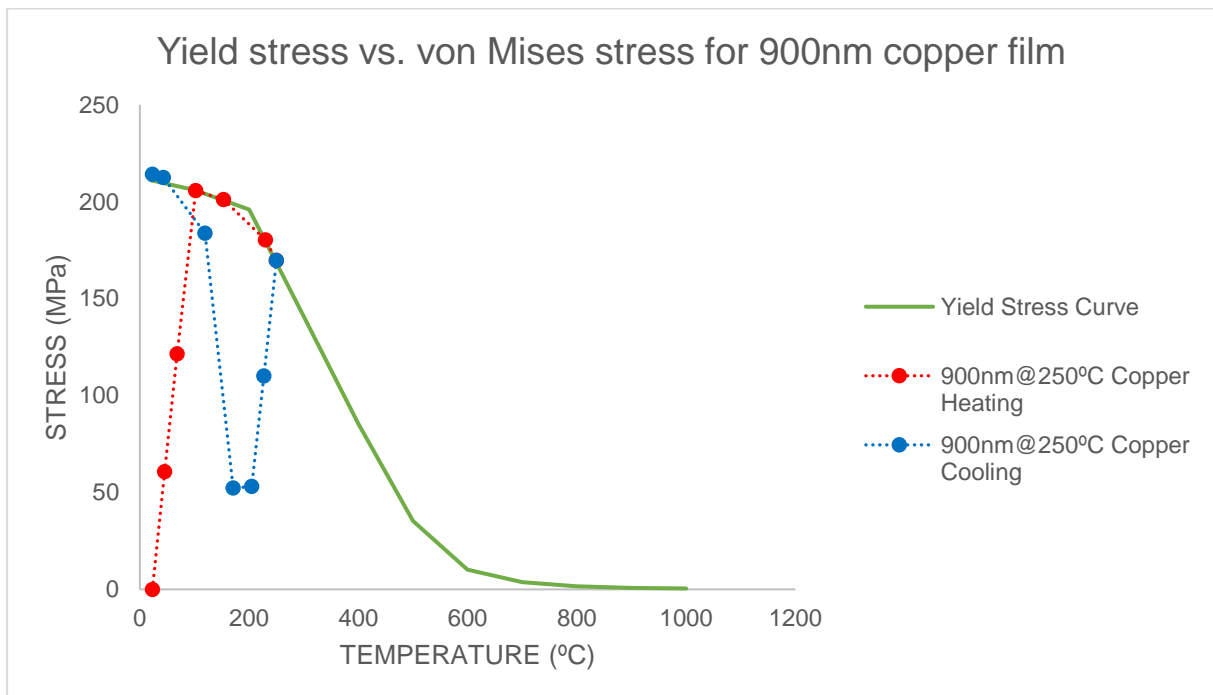


Fig 4.7 - Evolution of yield stress with temperature and comparison with von Mises stress from 900nm copper film

Up until now, the results discussed have focussed on the centre of the film. At the extremity, the von Mises stress behaves similarly as in the centre but upon closer inspection it shows that the stresses are different in these two points. While the S33 (Fig 4.9) stress remains very high and is the main reason as to why the von Mises graphs are similar, the S11 values are close to zero, as are the values for shear stress in the XY plane.

S22 (Fig 4.8) values are higher than what was observed at the centre, however they are lower than those observed along the Z-axis. It is nonetheless important to remark that both points have different stress component values.

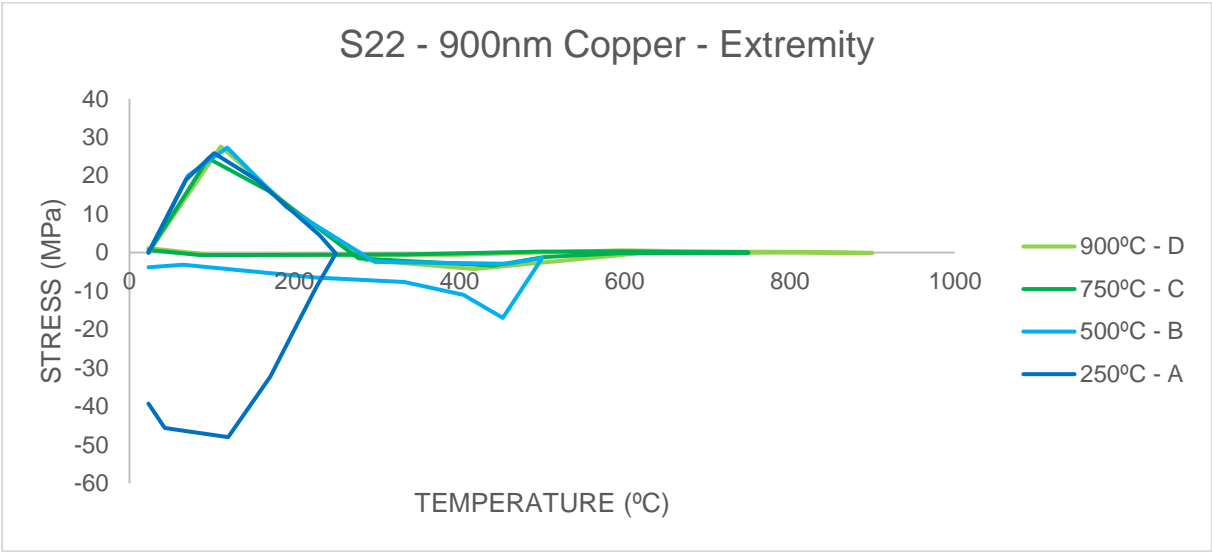


Fig 4.8 - S22 stress at the extremity of 900nm copper film

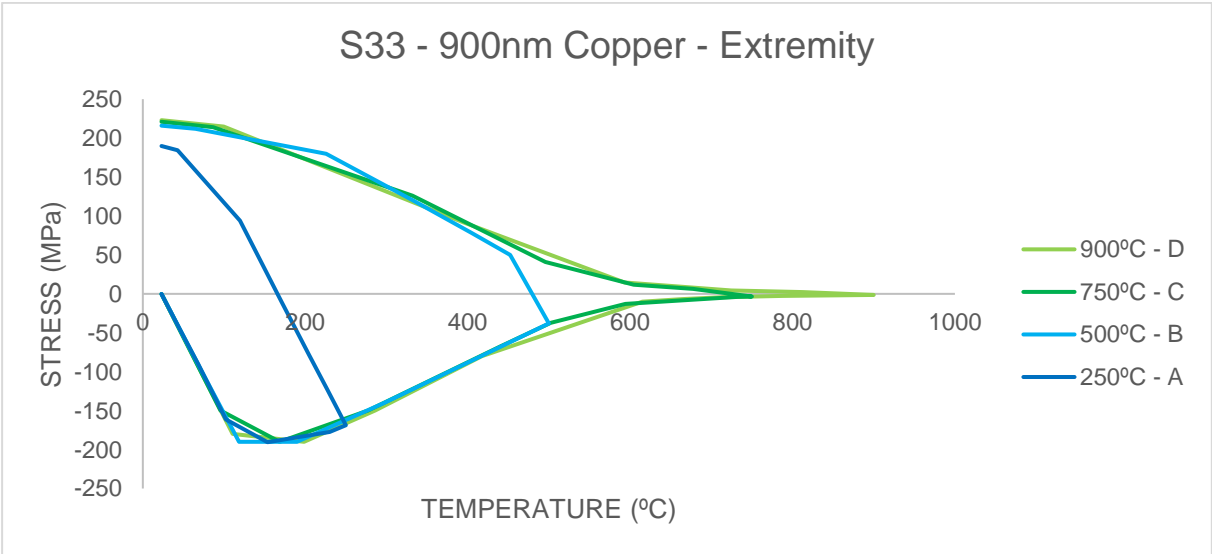


Fig 4.9 - S33 stress at the extremity of a 900nm copper film

The plastic strain analysis (Fig 4.10) continues this trend, as the same plateau that was described above for cycle A is also present here. Strain levels are also lower at the extremity, although they were already low at the centre, which fits with the analysis of the stress.

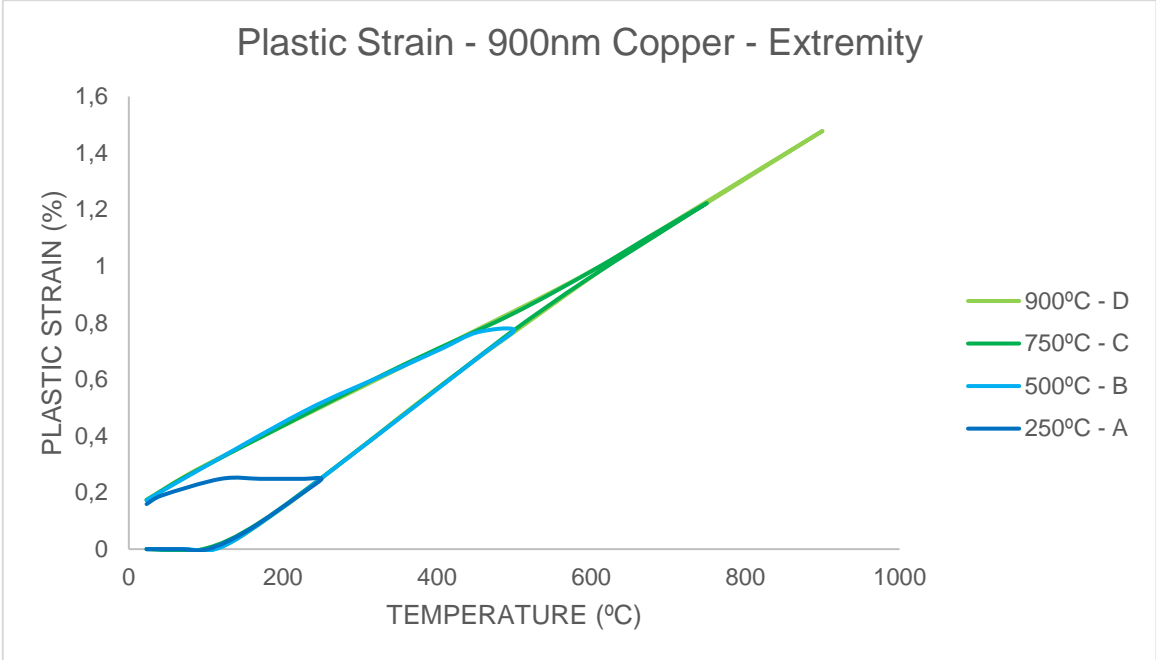


Fig 4.10 - Plastic strain at the extremity of a 900nm copper film

As the thickness of the copper film lowers there isn't much change. There was no evolution in the von Mises stress across the four different thicknesses (Fig 4.11), which indicates that the stress values of the main stress components didn't change either. At the centre, the stress levels of S11 and S33 remain comparable to those of the 900nm thick film. As for the stress values for S22 and S12, they decrease as thickness goes down to 480nm, 120nm and 30nm, but as covered previously these values were already approximately zero.

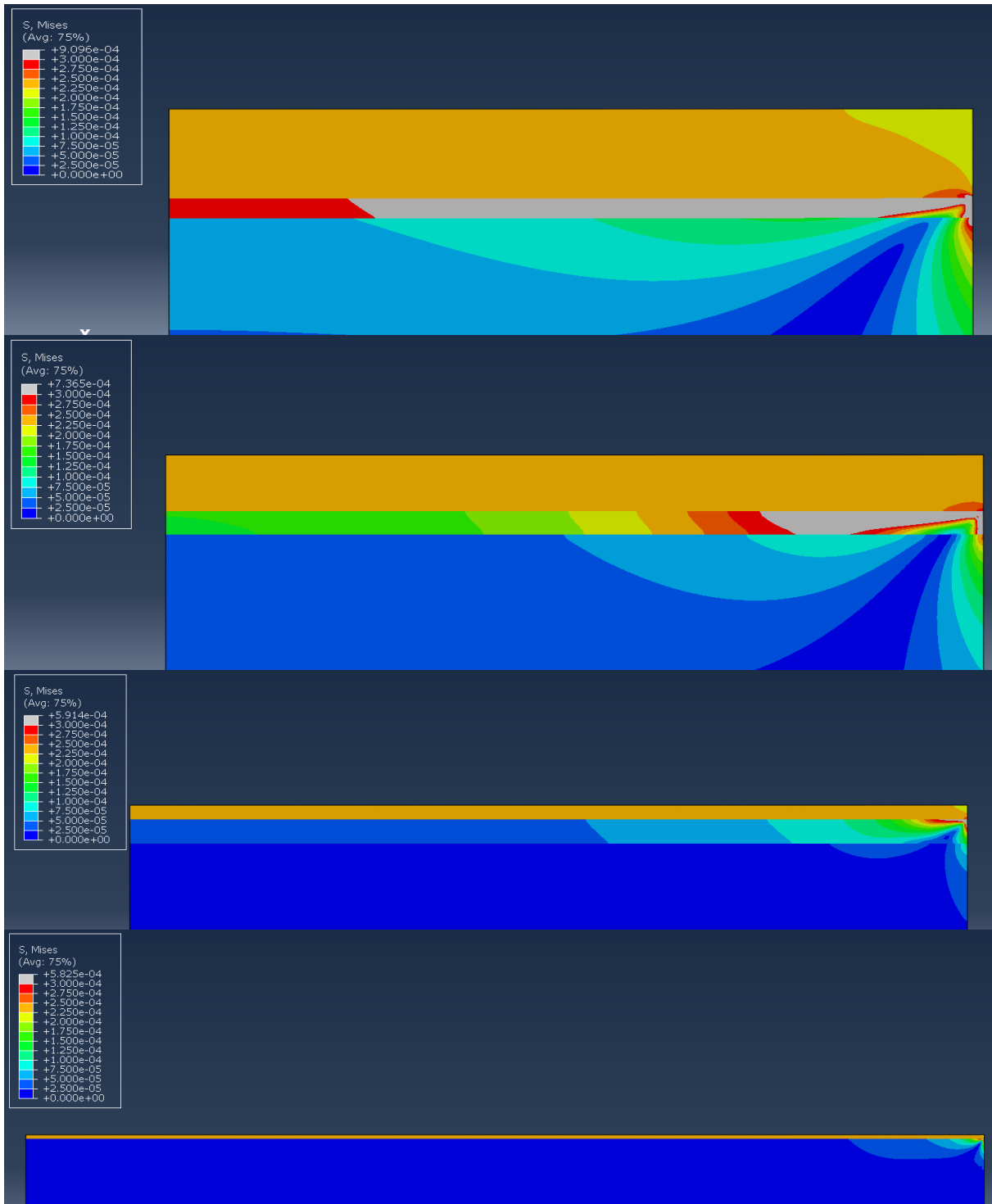


Fig 4.11 - Evolution of von Mises stress with the change in copper film thickness. From top to bottom: 900nm, 480nm, 120nm, 30nm. Only half of the film is represented

At the extremity we have a similar scenario, but there is an evolution in S22 stress levels. As the film's thickness lowers, there is an increase in stress levels however they remain very low when compared to S11 and S33 at the centre.

As there is no change in von Mises stress, it is logical that the plastic strain does not change since both are tied to yield criteria of the material. As such, the curves plotted for the 480nm, 120nm and 30nm films are very similar to what has already been covered.

4.1.2 - Molybdenum films

Since there are stability issues in copper films at the temperatures required for the CVD process, an alternative material, that was also viable for the process, was chosen to compare it against which would allow us to see if there were any differences in the behaviour that could indicate what to look out for when choosing other materials as alternatives. In this case, we chose molybdenum due to its higher melting temperature that leads to less instability related problems at higher temperatures.

Starting with the thickest molybdenum film at 900nm, some trends that were described previously in the copper films can be recognized here as well. As the heat starts to increase, von Mises stress (Fig 4.12 and Fig 4.13) rises until it reaches its yield value and then proceeds to gradually drop with the continued augment in temperature. However, unlike the copper films, with the molybdenum films stress levels dip as the cooling starts for all cycles before rising again.

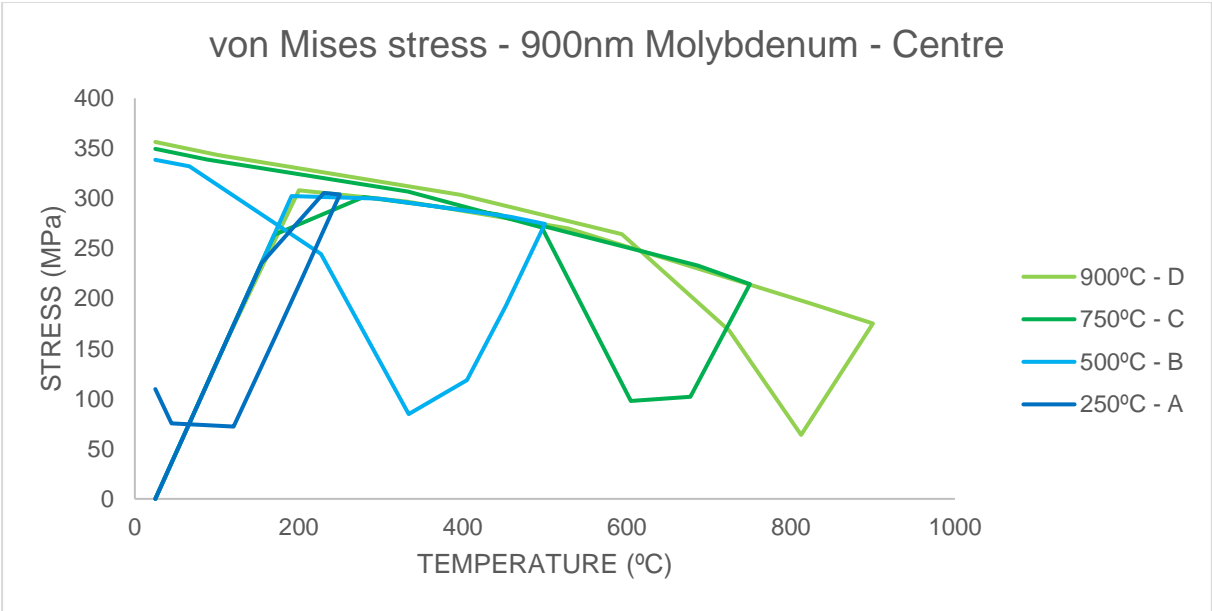


Fig 4.12 - von Mises stress at the centre of a 900nm molybdenum film

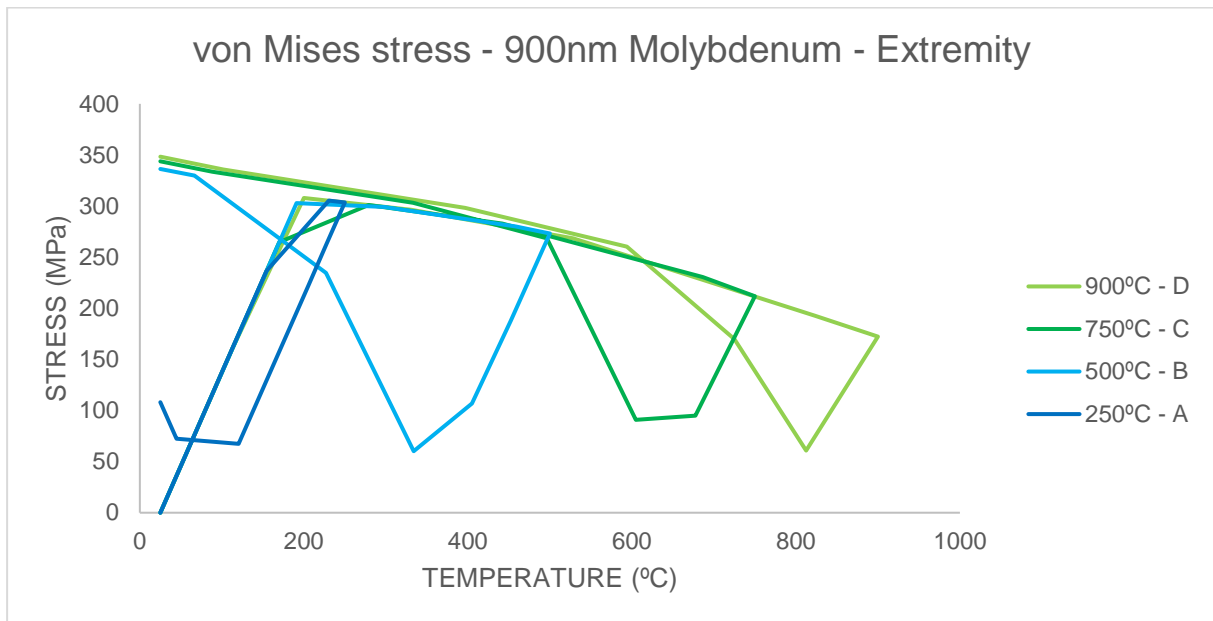


Fig 4.13 - von Mises stress at the extremity of a 900nm molybdenum film

Another difference from the copper films is the higher stress levels observed. Considering the equation for thermal stress (Equation 2.15), we can conclude that this is due to the bigger difference between the molybdenum's and SiO₂'s Young's Modulus, since the difference in coefficient of thermal expansion is lower. The difference of temperature is irrelevant for this comparison as it is equal for both materials.

At the centre, there is once more a similar behaviour to that of the copper films, with high stress levels in the S₁₁ (Fig 4.14) and S₃₃ (Fig 4.15) components while S₂₂ and S₁₂ are close to 0MPa. The same can be said of the stresses at the extremity of the film, where the stress levels are higher at S₃₃, and similar to those in the centre, and very low for S₁₁ and S₁₂, although S₂₂ stress levels (Fig 4.16) are higher than those seen in the copper film, even considering the overall increase in stress levels.

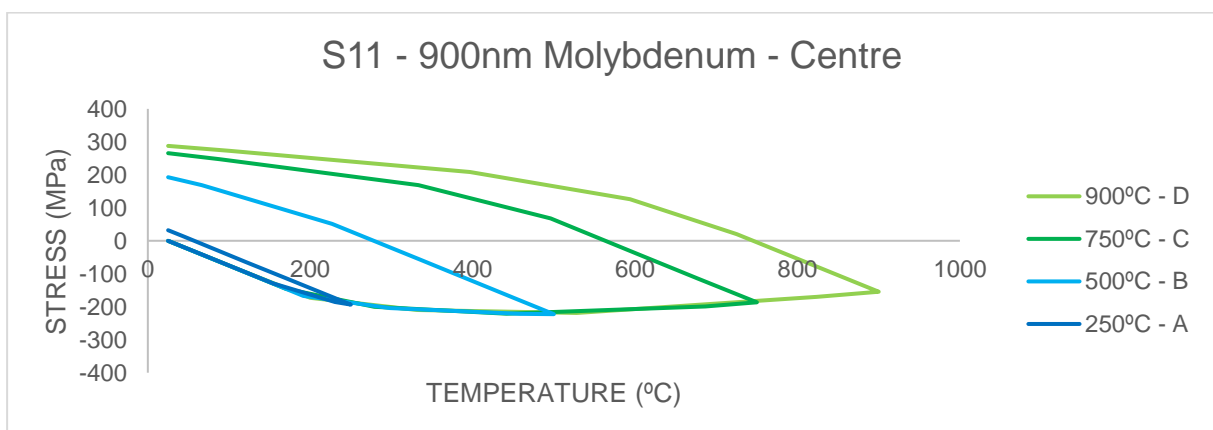


Fig 4.14 - S₁₁ at the centre of a 900nm molybdenum film

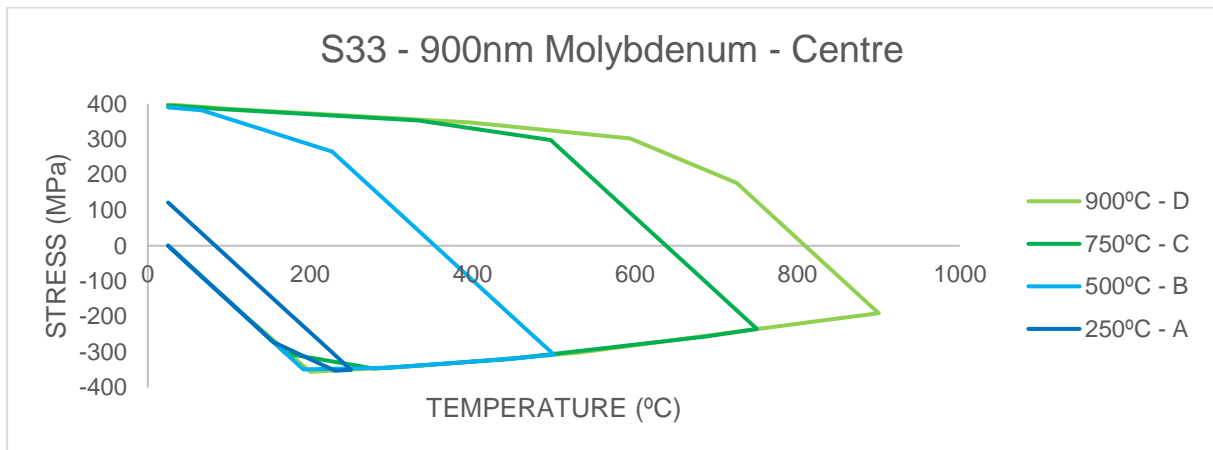


Fig 4.15 - S33 at the centre of a 900nm molybdenum film

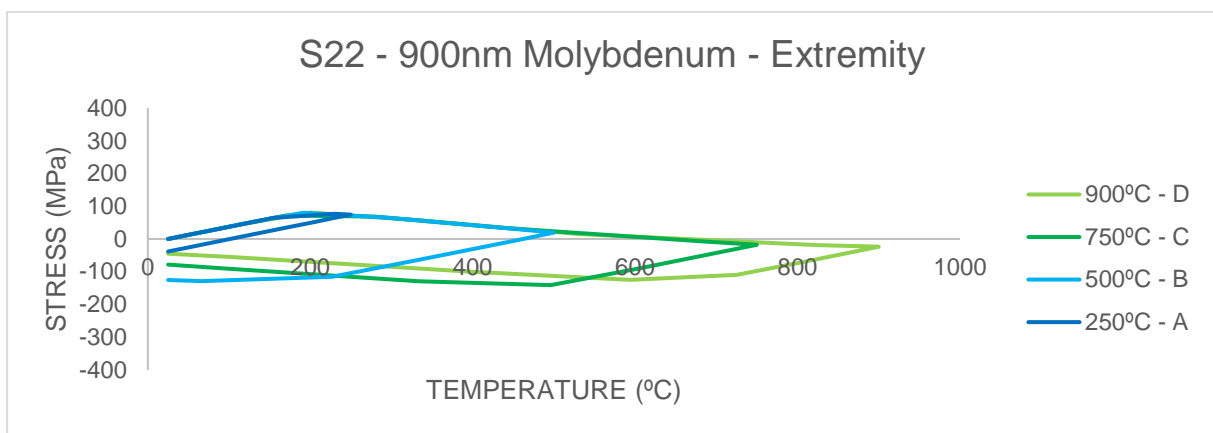


Fig 4.16 - S22 at the extremity of a 900nm molybdenum film

The similarities continue with the plastic strain results, where the plateaus seen in the copper results, however the strain levels are lower than those reported for the copper film. The results also differ in that there are plateaus for all cycles, which indicates that the film has elastic deformation even at the higher peak temperature cycles unlike in the copper films, and also that at lower peak temperatures the plastic strain remains constant throughout the cooldown phase without dropping off as the film reaches room temperature.

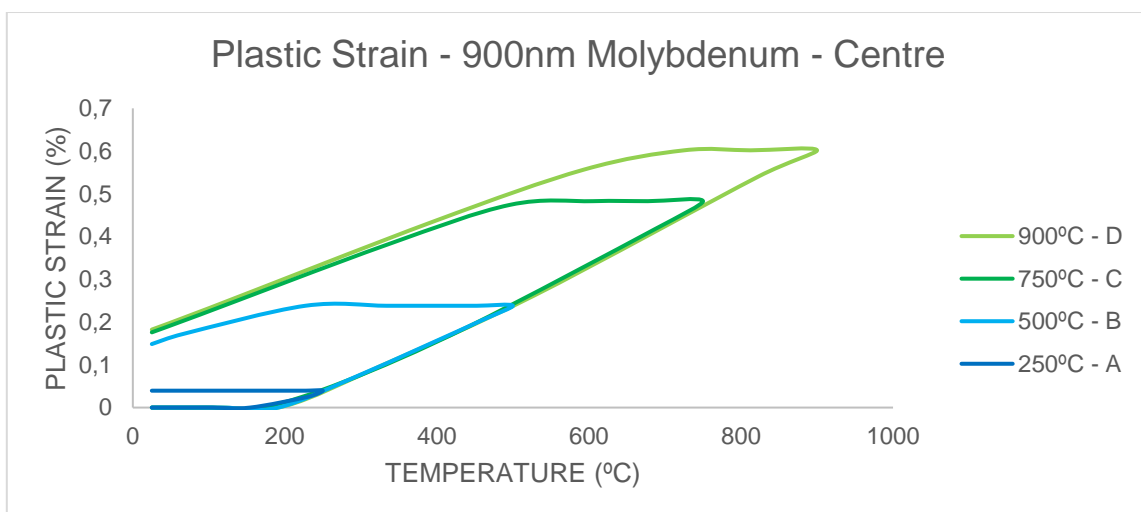


Fig 4.17 - Plastic strain at the centre of a 900nm molybdenum film

The stress and strain distribution between the centre and the extremity of the film is also reminiscing of what was described previously for the copper films, with S11 and S33 being stronger stresses in the centre and S22 and S33 being stronger at the extremity, S12 being very low at both points.

As it was the case in the copper model, the results of the thinner films of molybdenum remained similar to those of the thickest film. Von Mises stress levels remain again constant as film thickness lowers from 900nm to 480nm, 120nm and 30nm (Fig 4.18), the principal stresses remain S11 and S33 for the centre, and S22 and S33 for the extremity, and the same is true for the strain levels.

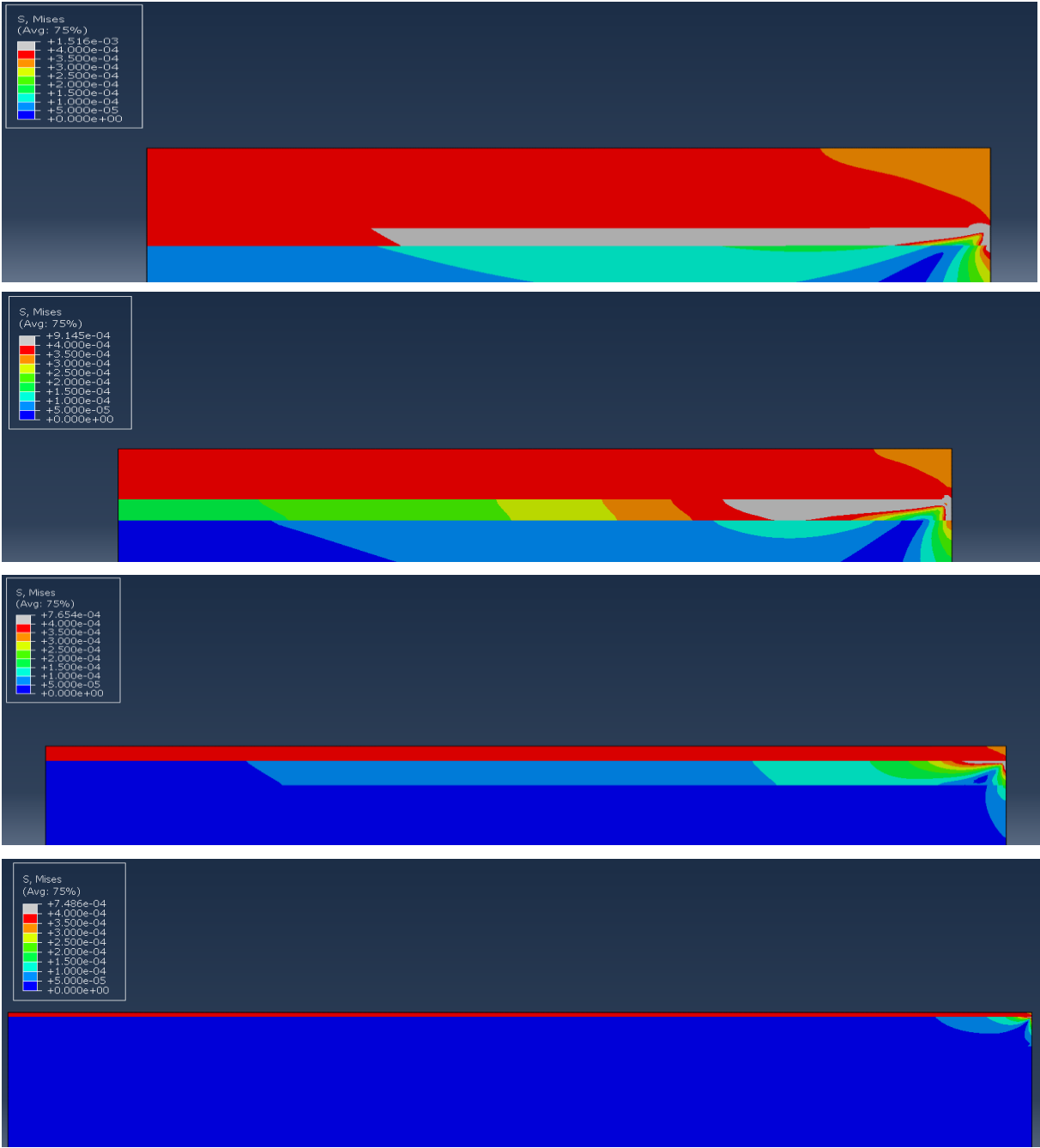


Fig 4.18 – Evolution of von Mises stress with the change in molybdenum film thickness. From top to bottom: 900nm, 480nm, 120nm, 30nm. Only half of the film represented

While the stress and strain levels differ between the two materials, there are trends, like the dips of the stress results and the plateaus of the strain results. These are common to both but occur at much higher temperatures for the molybdenum films.

Using the homologous temperature of the film, which measures the temperature as a fraction of the melting temperature of a given material, we have a better basis of comparison between the copper and the molybdenum to see if the difference in fusion temperatures is a factor in the behaviours that we observed.

$$T_{homologous} = \frac{T(K)}{T_{melting\ point}(K)} \quad (4.2)$$

To that effect, the search for the point at which the dips in the von Mises stress results stopped appearing started in the copper film. A 900nm thick film was used for this analysis and performed cycles at different temperatures until the results did not show the dip at the start of the cooling phase anymore. According to the results (Fig 4.19), that would stop occurring for cycles with a peak temperature of 475°C or higher, which is the equivalent to $0,55T_{melting\ point}$ of copper.

Transferring that value to the molybdenum film would mean that for cycles with peak temperatures of 1307°C the dip would not be visible anymore, which was confirmed by the results (Fig 4.20). However, further analysis revealed that the lowest peak temperature at which the dips were not observed was around 1200°C, corresponding to $0,52T_{melting\ point}$ of molybdenum. While not exactly the same value for both materials, we can however conclude that the two materials have comparable mechanical properties as they exhibit the same behaviour at the same homologous temperatures.

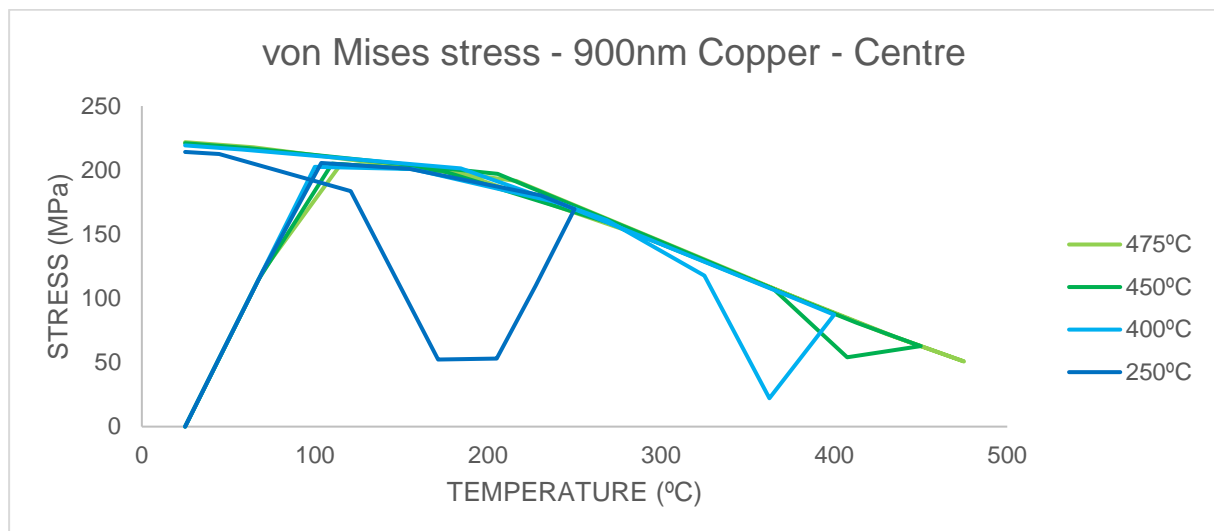


Fig 4.19 - von Mises stress at the centre of a 900nm copper film

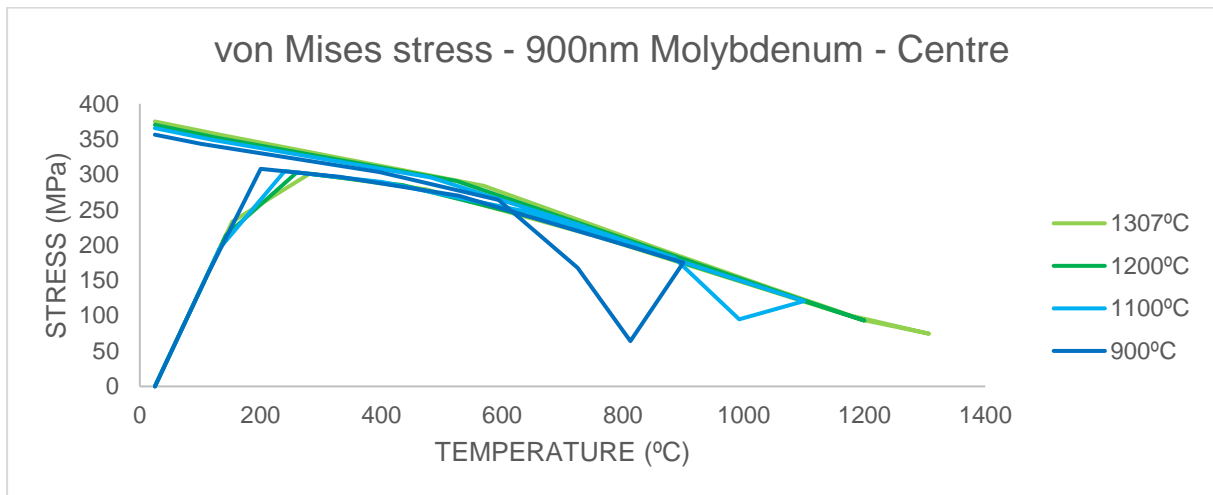


Fig 4.20 - von Mises stress at the centre of a 900nm molybdenum film

This is further shown by comparing the evolution of the yield stresses with the temperature of both materials but using homologous temperature instead of the Celsius scale (Fig 4.21). Both curves are very close at the homologous temperatures where we stopped observing dips in both materials.

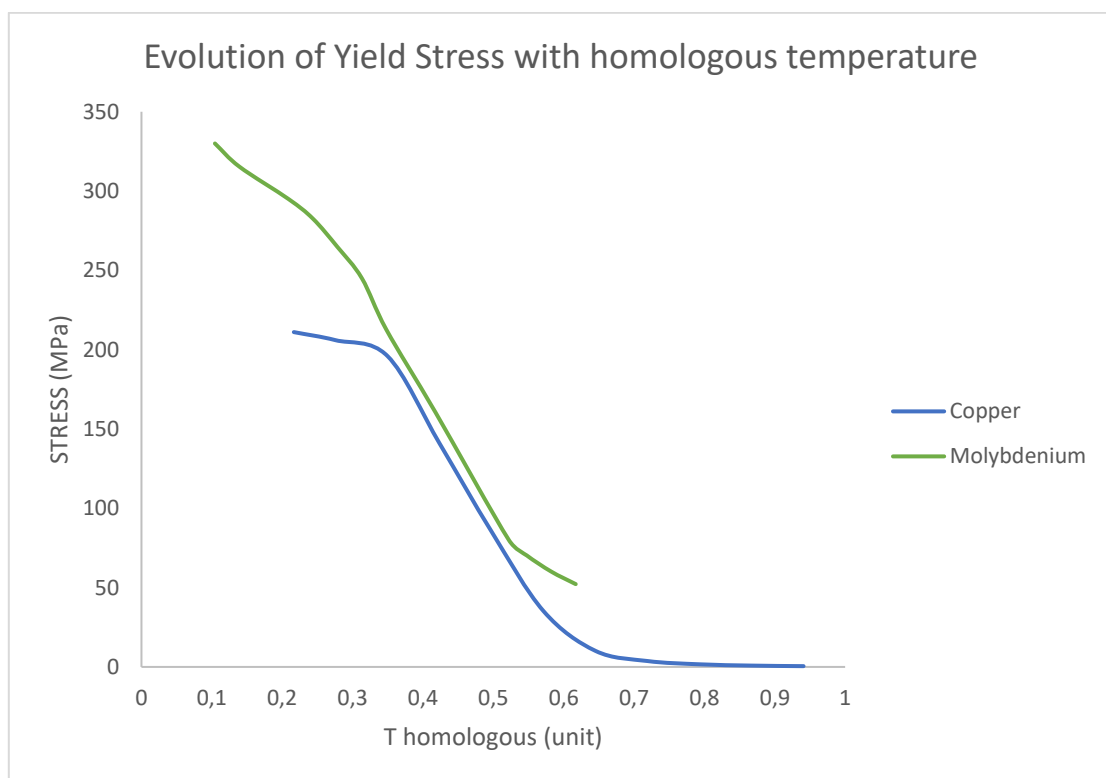


Fig 4.21 - Evolution of yield stress with homologous temperature in copper and molybdenum

This analysis was also performed for the plastic strain to see if the plateaus that were reported for both films could also be related to comparable mechanical properties. As such, it began by finding the highest peak cycle temperature at which the molybdenum film had no decrease in plastic strain during the cooling phase in a 900nm film (Fig 4.22). It was found that the highest temperature at which that behaviour was observed was for a cycle that peaked at 365°C, which corresponds to

$0,22T_{melting\ point}$ of molybdenum. Transferring this value to the copper films would mean that the last plateau would be observed at 28°C but after performing some further iterations it was discovered that the plastic strain remains constant during the cooling phase up to temperatures as high as 200°C (Fig 4.23), or $0,35T_{melting\ point}$ if we compare the homologous temperatures, in the 900nm copper film.

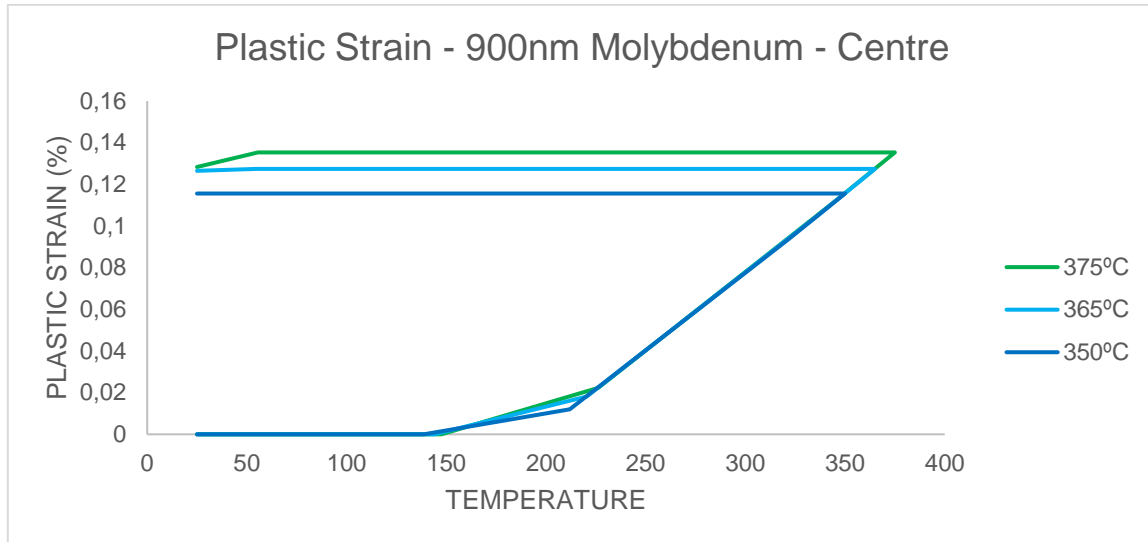


Fig 4.22 - Plastic strain at the centre of a 900nm molybdenum film

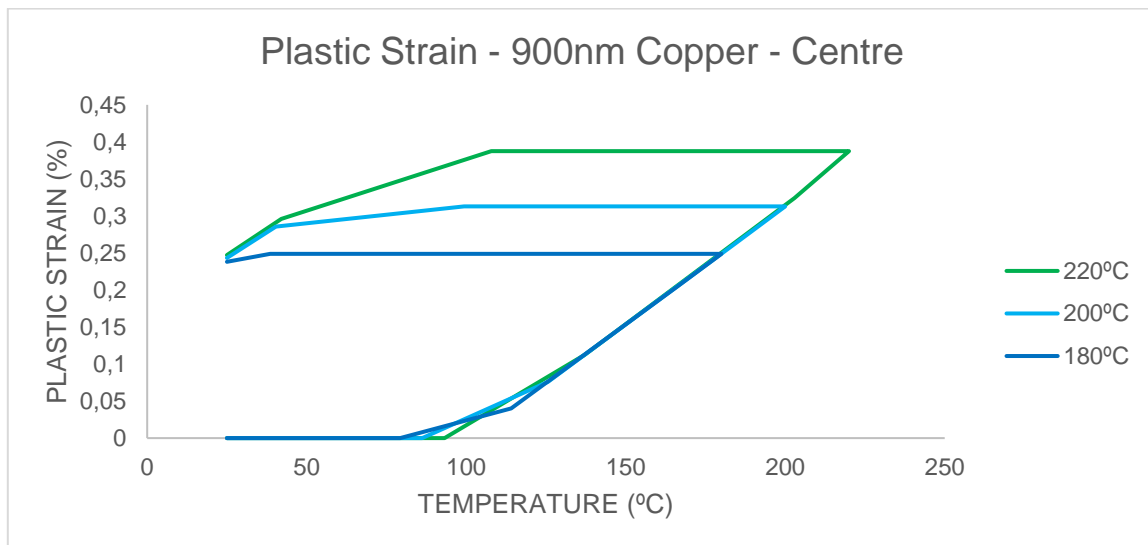


Fig 4.23 - Plastic strain at the centre of a 900nm copper film

This means that a temperature-related connection cannot be established for this behaviour regarding the plastic strain results of the two metals, unlike the stress results addressed previously. Looking again at the graph with the comparison of both material's yield stresses, there is a big difference between them for $0,22T_{fus}$ and for $0,35T_{fus}$ which explains the difference in behaviour.

4.2 Three dimensional studies

Taking the model into 3D space, we can see that the behaviours that were reported in the bidimensional studies continue to appear. Starting with a 20 μ m long model with a 480nm copper film, the von Mises stress levels (Fig 4.24) rise with the increase in temperature until they reach yield stress levels, at which point they follow they gradually lower as the yield stress value is reduced due to the increasing temperature. Stress levels start to rise again as cooling begins, again following closely the yield stress levels.

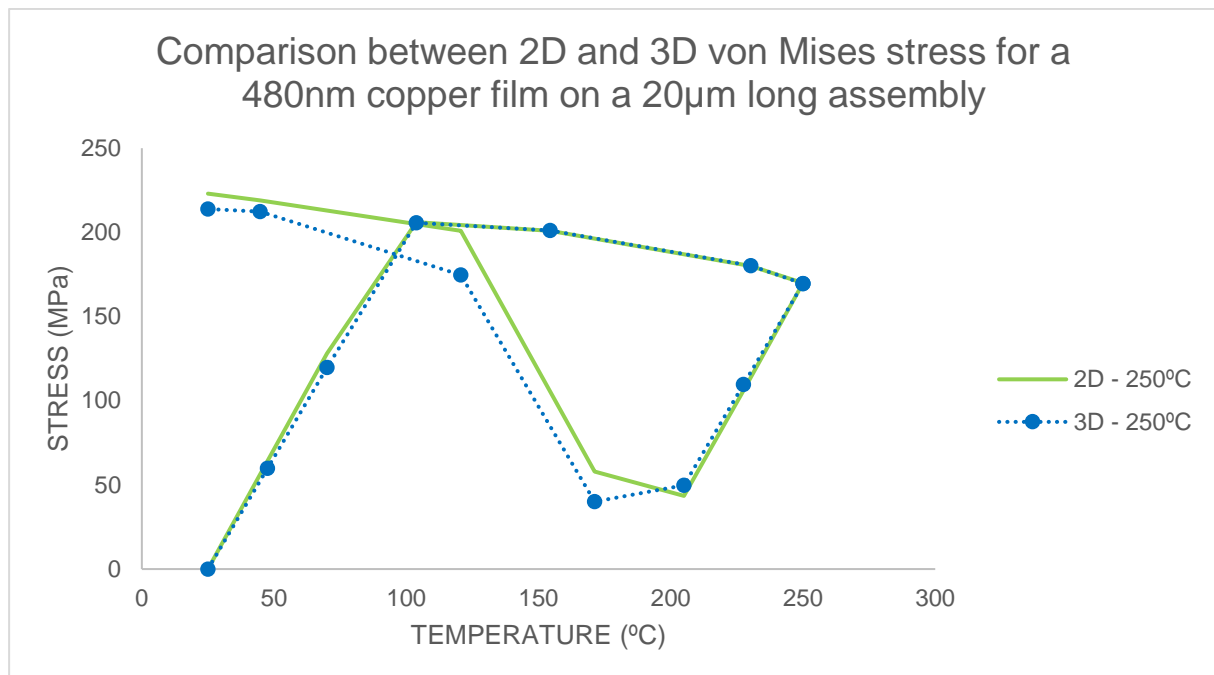


Fig 4.24 - Comparison between 2D and 3D von Mises stress of a 480nm copper film, at the centre

As before, the main stress components remain S11 and S33 for the centre and S22 and S33 for the extremity, and the levels in both remain comparable to what has been previously described in the 2D models. This is also true for the plastic strain results.

While the results and trends seen previously remain comparable to what has been described previously, there is still a difference between the values registered as was expected since the bidimensional models were developed under the supposition of plane strain that considers an infinitely long model to nullify the effect of strain along the Z-axis. As such, the model was rendered with several lengths to see how this impacts the stress and strain values.

This analysis was performed for the 480nm and 120nm copper films for cycles that peaked at 250°C and 500°C, focussing on the centre of the film as it was where the highest stress values were registered in the bidimensional models, and observed that there was a difference between the longer films and the shorter ones.

In the 480nm film there is a noticeable difference in the results as the length increases from a 5µm to a 40µm film. The von Mises stress results for the cycle peaking at 250°C (Fig 4.25) show that the shorter assembly stress levels peak at a lower value, but as the temperature continues to increase, they end up matching with the longer films. As the model enters the cooling step, the values dip as expected and we see again a separation between the results of the longer and shorter films.

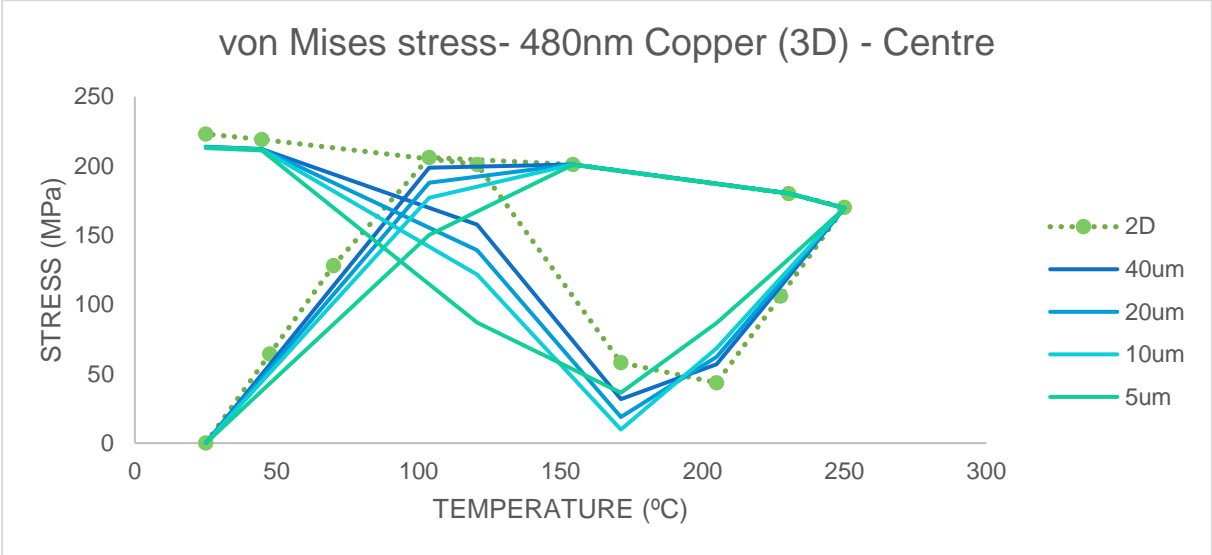


Fig 4.25 - von Mises stress at the centre of a 480nm copper film, 3D model

This is also visible in the stress component results. While for S11 there is not much difference as the length of the film varies, the 5µm long assembly does have a slightly different behaviour but it is still consistent with the other results, the difference is much more noticeable in the S33 component (Fig 4.26). The results show that as the film's length increases that the results get closer to what was recorded in the 2D 480nm thick copper film. There is also a convergence point at the end of the heating phase, before spreading again as the film begins to cool down with longer films having higher stress levels.

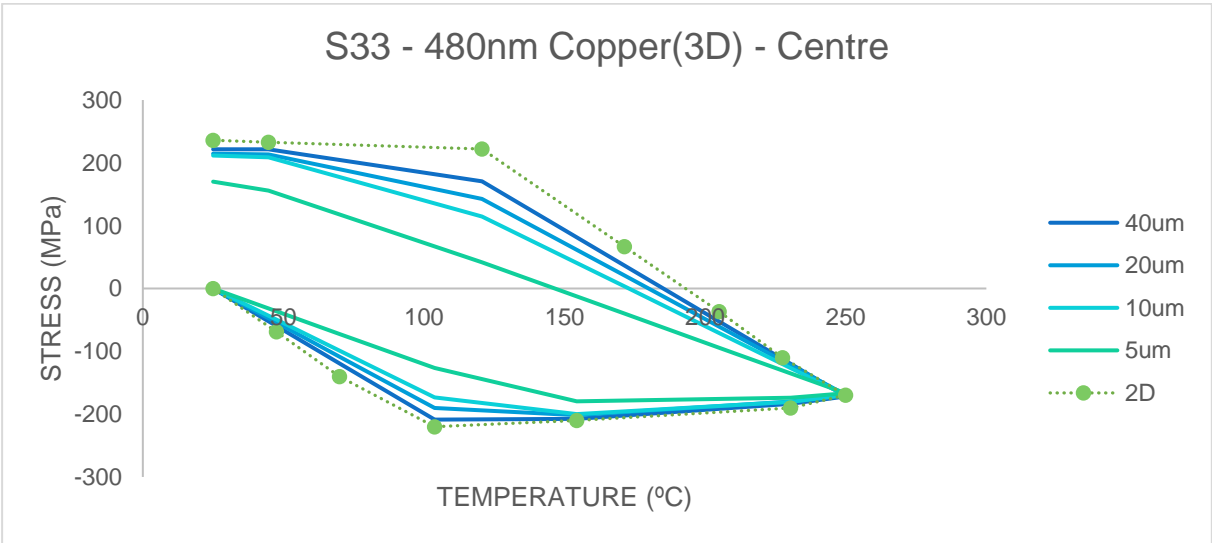


Fig 4.26 - S33 at the centre of a 480nm copper film, 3D model

Looking at the plastic strain results (Fig 4.27) it is visible why the von Mises stress curve for the 5µm long film was different from the others. With the temperatures ramping up, the initial plastic strain increase is not as steep as the longer films, leading to lower stress levels. As the heat continues to rise, stress levels become similar in all models and so does the incline of the plastic strain curve. Strain levels also start to drop off at the same point although the decrease isn't as severe in the 5µm long film.

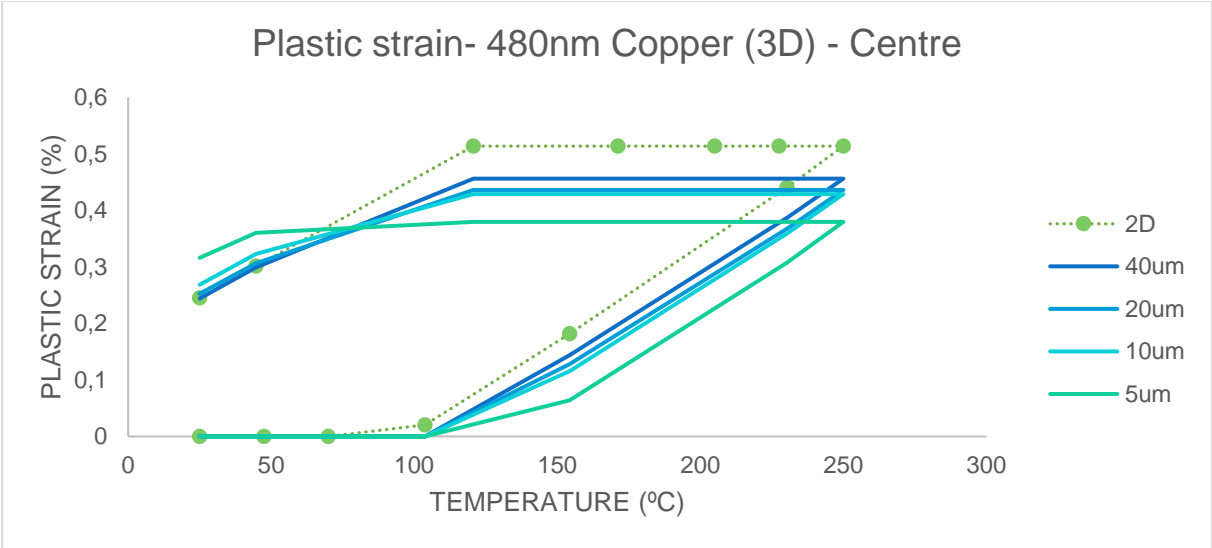


Fig 4.27 - Plastic strain at the centre of a 480nm copper film, 3D model

Comparing with the results from the 2D model, the initial incline is steeper than that of the longest film and that the plastic strain levels are higher at the end of the heating phase. There is nonetheless a continuity to the results, and there is a trend as the length of the film increases that tends towards the values registered in 2D space.

Increasing the peak temperature of the cycle from 250°C to 500°C leads to an interesting result (Fig 4.28). The differences between the varying lengths of copper film, while still present, are much less noticeable in the von Mises stresses apart from the initial peak value for the shortest 5µm film, unlike what has been reported previously. In fact, as the temperature keeps climbing, we see that the values become almost identical for all models, as if the evolution of yield stress with the increasing heat served as a cap on the stress levels and normalized the results. We also see these changes in the S11, S33 and plastic strain results.

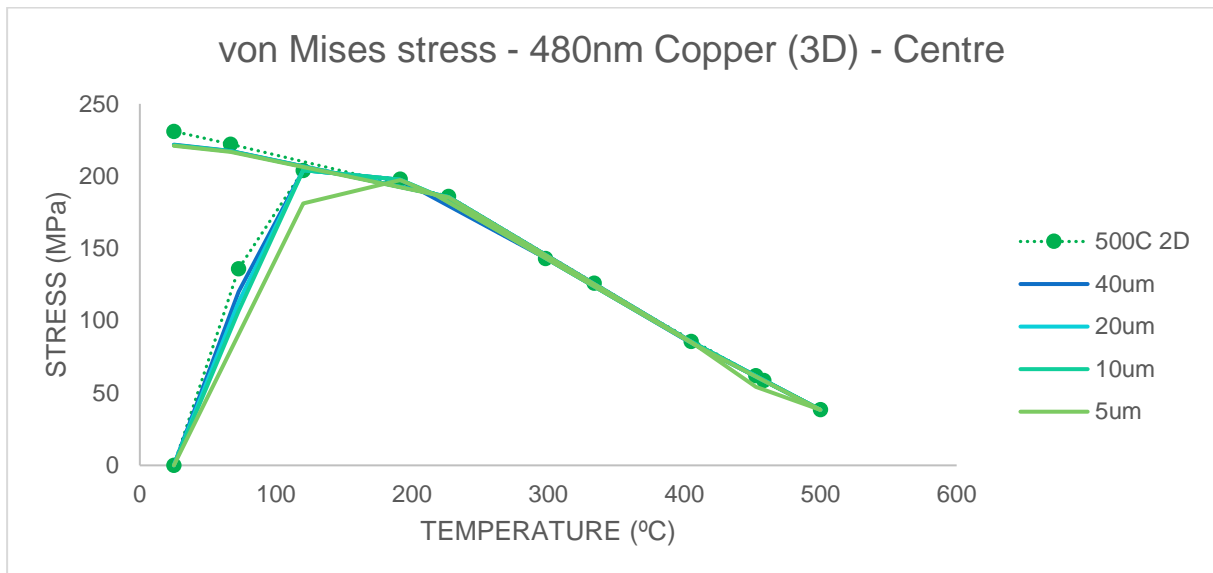


Fig 4.28 - von Mises stress at the centre of a 480nm copper film, 3D model

The results for the 120nm thick copper film are similar to the ones seen in the 480nm film but the differences seen for a 250°C peak temperature cycle aren't as evident (Fig 4.29). Unlike in the thicker film, there isn't a big difference between the 40µm and the 5µm long films when the film transitions from elastic to plastic deformation as results remain homogenous during the heating phase. There is a separation as the stress values dip as the cooling phase begins and results converge again when the film is close to room temperature.

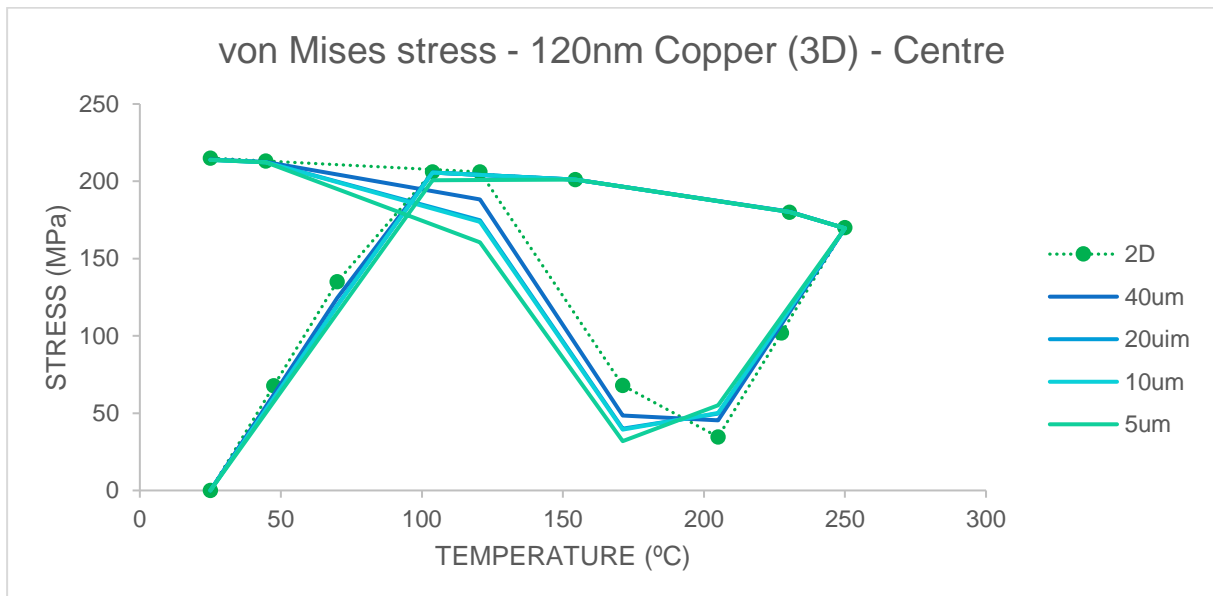


Fig 4.29 - von Mises stress at the centre of a 120nm copper film, 3D model

This can also be observed in the main stress components. For S11 the results are similar throughout the cycle for all the 3D and 2D models, while in the S33 results (Fig 4.30) the separation that was described in the von Mises stress results is visible again. As the temperature starts to come down,

the stress levels increase at different rates for the various lengths, with longer models having steeper curves than the shorter ones.

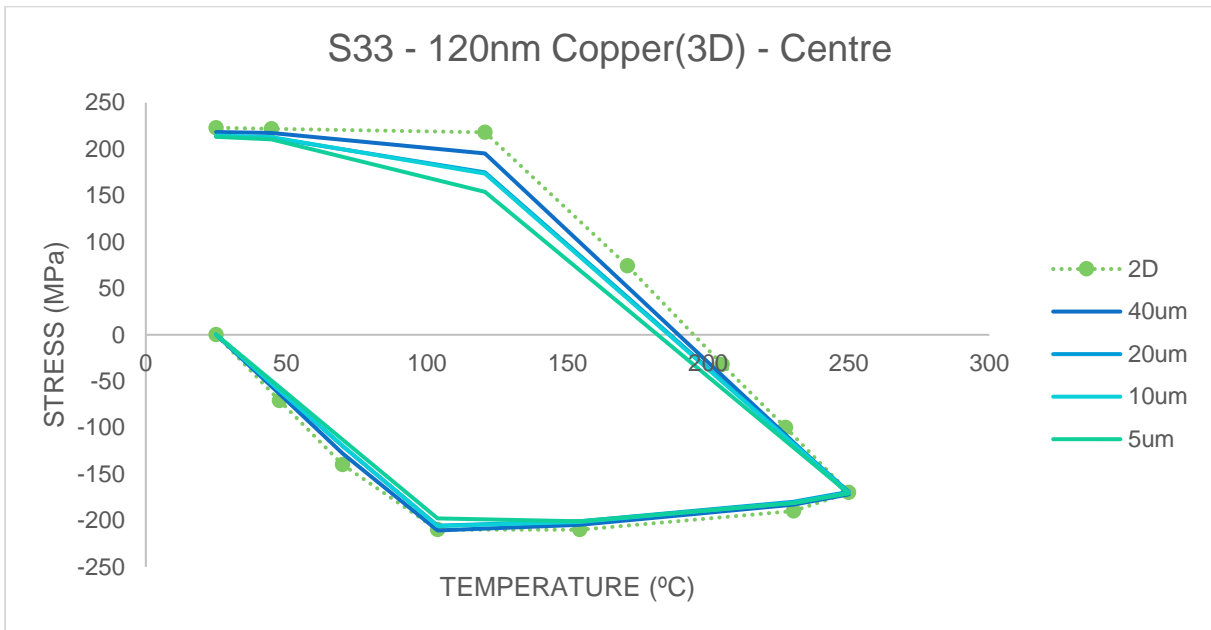


Fig 4.30 - S33 at the centre of a 120nm copper film, 3D model

Like the S11 stress results, plastic strain levels were similar in all 3D models but there is a difference to the 2D model. However, since the plastic strain levels are very low this difference may not be as significant as the graphs might make it seem (Fig 4.31).

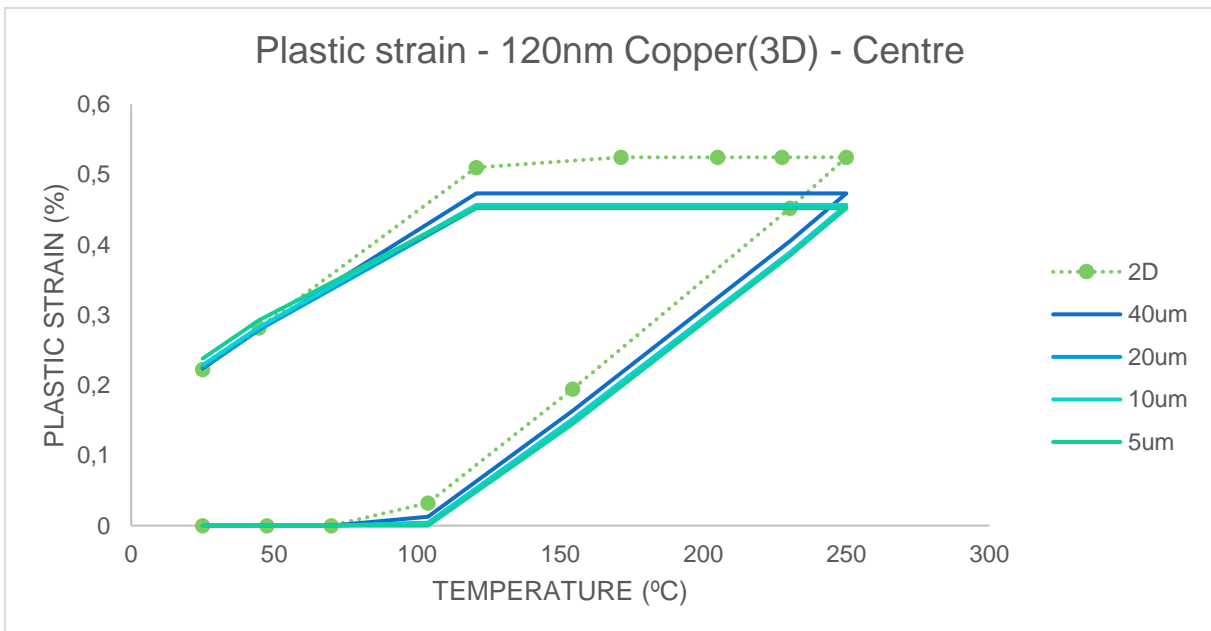


Fig 4.31 - Plastic strain at the centre of a 120nm molybdenum film, 3D model

By increasing the peak temperature up to 500°C, the impact that the evolution of yield stress with the temperature has in the stress results can be observed again. There is no longer any difference in the stress results from both 3D and 2D models across von Mises stress (Fig 4.32) and the S11 and S33 stress (Fig 4.33) components, which shows that the stress levels of the film are dictated by the yield stress since the plastic strain levels are very low.

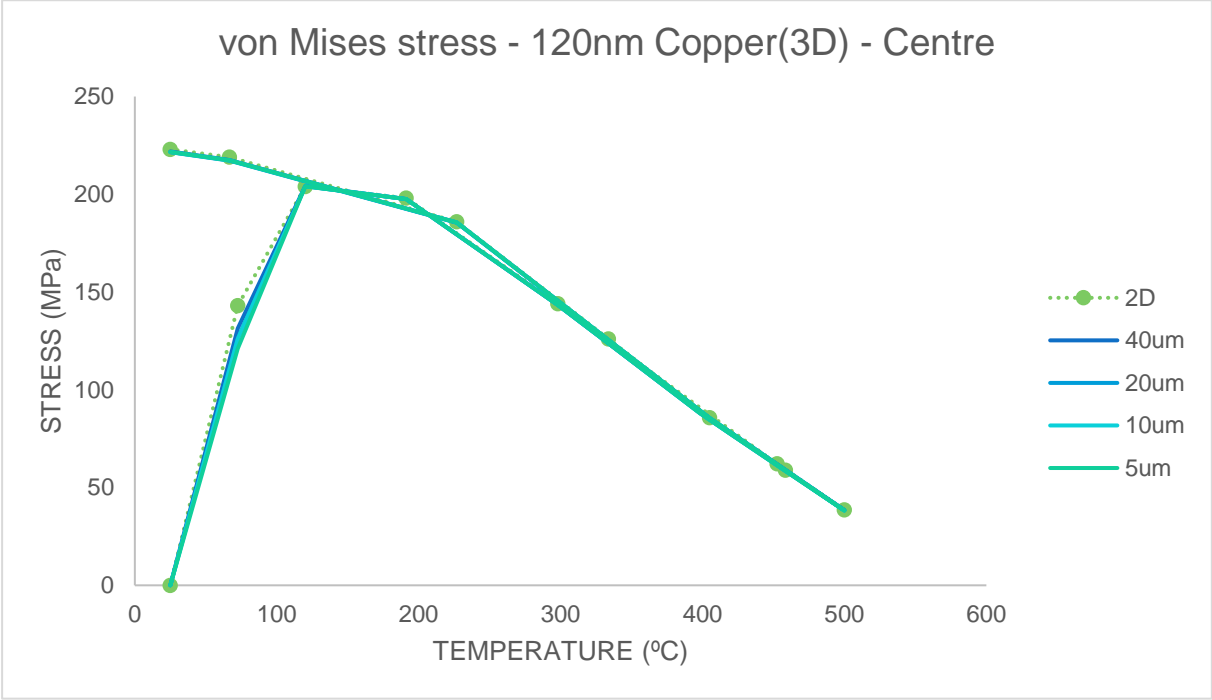


Fig 4.32 - von Mises stress at the centre of a 120nm copper film, 3D model

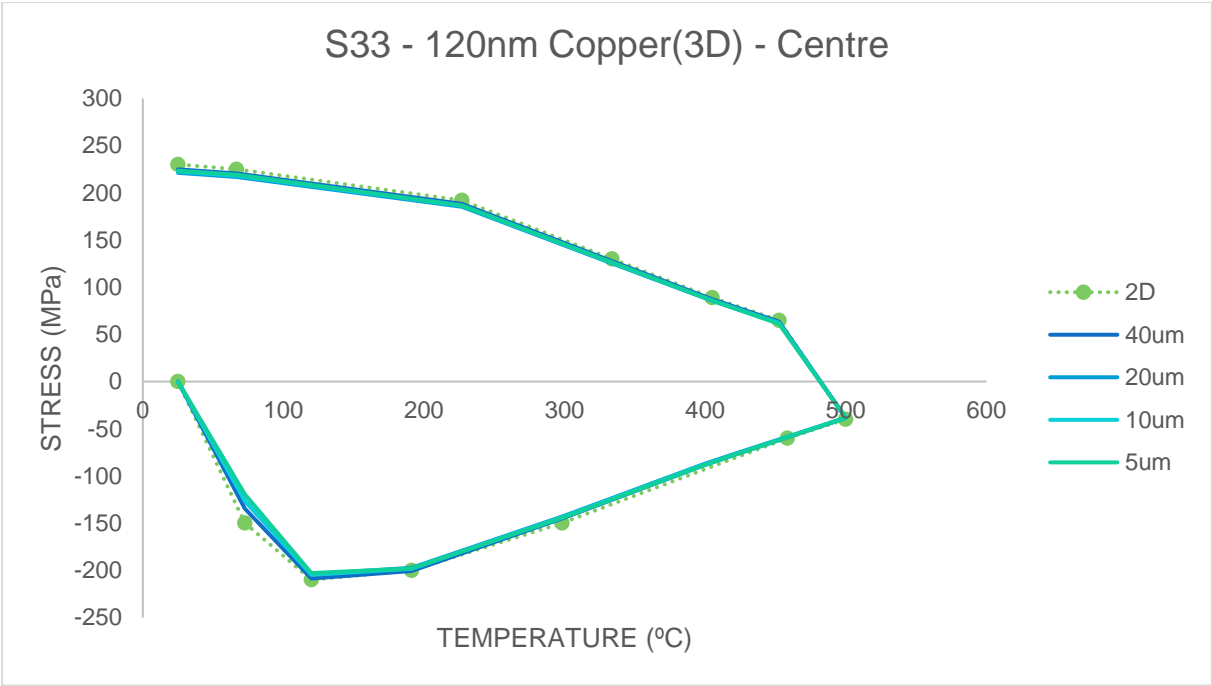


Fig 4.33 - S33 at the centre of a 120nm copper film, 3D model

With the increase in temperature we also see an increase in the plastic strain levels, as was also seen in the 2D model. And like the stress results, the plastic strain results (Fig 4.34) at this temperature are very consistent for all the lengths of film, however there is still a gap to the bidimensional results. In this case, the gap is more significant than at the lower peak temperature but strain levels remain relatively low, which mitigates the impact that this difference between results has.

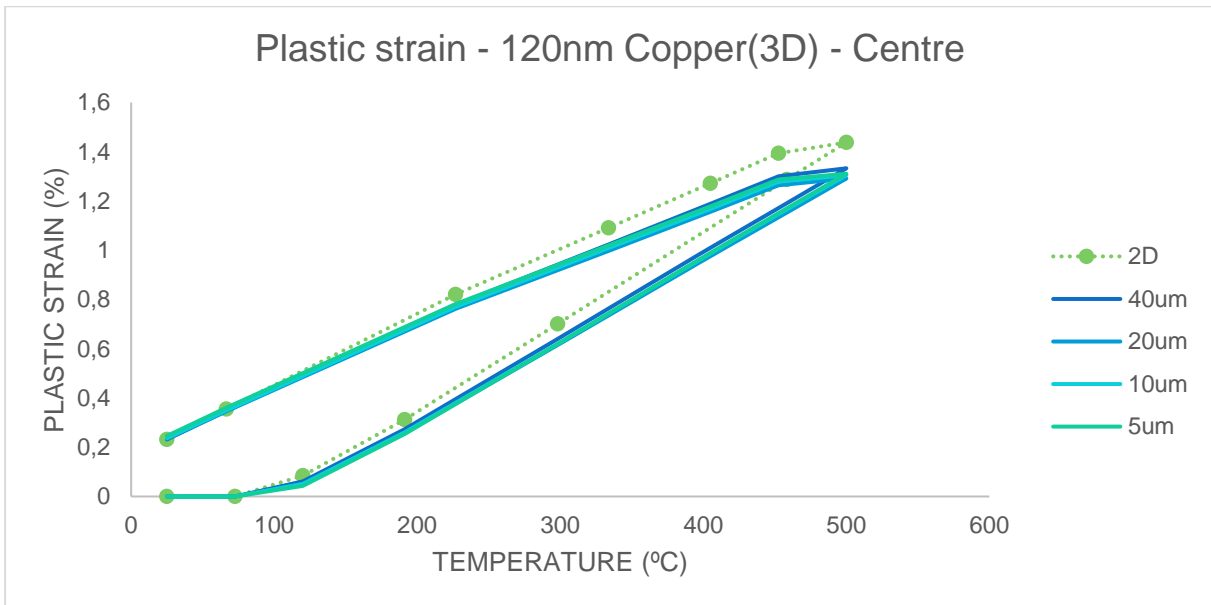


Fig 4.34 - Plastic strain at the centre of a 120nm copper film, 3D model

The following table (Table 4.1) shows us the residual values for plastic strain and the main stresses at the centre of the film for all the cases studied in 3D space, giving a final overview of the results discussed previously.

Table 4.1 - Residual values for copper film results

Copper 3D residual values											
Film thickness		480nm					120nm				
Film length		2D	40µm	20µm	10µm	5µm	2D	40µm	20µm	10µm	5µm
500°C	$\epsilon_{plastic}$	0,25	0,25	0,26	0,27	0,33	0,23	0,23	0,23	0,24	0,25
	σ_{vM}	231	222	221	221	221	223	222	222	222	222
	S11	223	218	222	221	221	216	219	222	221	220
	S33	246	225	221	222	220	230	225	221	223	223
250°C	$\epsilon_{plastic}$	0,25	0,24	0,25	0,27	0,32	0,22	0,22	0,23	0,23	0,24
	σ_{vM}	223	214	214	213	213	215	214	214	214	214
	S11	209	205	213	215	234	206	209	214	213	214
	S33	210	222	215	212	170	223	218	214	215	213

5. Conclusions

Although this model is very limited as it applies to a very specific case both in terms of geometry and starting conditions, it does provide a valid insight into how the film behaved. While the von Mises stresses were similar at both the centre and the extremity of the film, the two points were in fact affected by different stress levels, being lower at the extremity than at the centre. It was also found that the evolution of the yield stress as the temperatures increased conditioned the stress levels as the thermal cycle advanced, and how it homogenized.

The residual stresses for both copper and molybdenum films remained approximately constant regardless of thickness variations. The residual plastic strain was also constant for both materials and relatively low, however it is not negligible as it can have an impact in the ability of the film to serve as a catalyst for graphene growth since plastic deformation is associated with the presence of crystalline defects.

The comparison between the copper and the molybdenum films also showcased other interesting behaviours, in particular the fact that the two materials' stress curves trends were similar at the same homologous temperatures but the strain curves were not, suggesting that after a certain point in the temperature range there is a transition regime common to both materials. The difference in the stress levels that we observed was also interesting: although the difference in thermal expansion coefficients was lower for the molybdenum films, stress levels were in fact higher due to its higher Young's Modulus compared to the one of copper. It was also observed that the copper films remained mostly in a plastic deformation regime while the molybdenum films deformed under plastic and elastic regimes.

As the model transitioned to a three-dimensional analysis, the results remained consistent. The study of the impact of length variation in the three-dimensional models did show that there was a coherence between the two approaches, as the results observed always converged towards what was reported for the 2D models as the assembly increased in size. This indicates that bidimensional models can be used to study the influence of process parameters on the behaviour of graphene catalysts.

However, many of the limiting factors of the metallic thin films used as catalysts in this process have not been taken into account in this model, such as the dewetting of the film due to instabilities at high temperatures, the initial stresses that emerge during the deposition of the thin metallic film on top of the Si/SiO₂ substrate and the stress relaxation effects that appear during the thermal cycle that were covered in this work. These are other avenues to further continue the study of the behaviour of metallic thin films during the CVD process.

In summary:

- Residual stress values remain approximately constant as the thickness of film is varied for both copper and molybdenum

- Residual plastic strain is generally low but not negligible for both materials ($\approx 0,2\%$). This can have an impact on the ability of the film to serve as catalyst for the growth process, as plastic deformation is associated with the presence of crystalline defects, such as dislocations
- In the thermal cycles studied, copper remains mostly in the plastic deformation regime, whereas in the case of molybdenum the film deforms under the elastic and plastic regimes
- Stress-strain behaviour in copper and molybdenum can be compared using the concept of homologous temperature
 - Stress-related behaviour at relatively high homologous temperatures ($T_{\text{homo}} \approx 0,4 - 0,5$) is similar for both materials
 - Residual plastic strain is different for both materials in the case of relatively low homologous temperatures ($T_{\text{homo}} \approx 0,2 - 0,3$)
- 3D study confirmed the findings of the bidimensional study
 - General trends in stresses can be observed: as film length increases, 3D results converge to 2D
 - 2D studies can generally be used to study the influence of process parameters on the behaviour of graphene catalysts

Bibliography

- [1] A. M. De Deus, "A ciência sem nome," *Diário de Notícias*, 2018. [Online]. Available: <https://www.dn.pt/opiniao/opiniao-dn/convidados/a-ciencia-sem-nome-10360194.html>. [Accessed: 12-Feb-2018].
- [2] A. Jorio, G. Dresselhaus, and M. S. Dresselhaus, "Carbon nanotubes: Advanced topics in the synthesis, structure, properties and applications," *Top. Appl. Phys.*, vol. 111, no. 3, p. 57, 2008.
- [3] M. Kumar and Y. Ando, "Chemical vapor deposition of carbon nanotubes: A review on growth mechanism and mass production," *J. Nanosci. Nanotechnol.*, vol. 10, no. 6, pp. 3739–3758, 2010.
- [4] N. Mohammadian, S. M. Ghoreishi, S. Hafeziyeh, S. Saeidi, and D. D. Dionysiou, "Optimization of synthesis conditions of carbon nanotubes via ultrasonic-assisted floating catalyst deposition using response surface methodology," *Nanomaterials*, vol. 8, no. 5, pp. 1–14, 2018.
- [5] F. Bonaccorso, A. Lombardo, T. Hasan, Z. Sun, L. Colombo, and A. C. Ferrari, "Production and processing of graphene and 2d crystals," *Mater. Today*, vol. 15, no. 12, pp. 564–589, 2012.
- [6] N. C. Bartelt and K. F. McCarty, "Graphene growth on metal surfaces," *MRS Bull.*, vol. 37, no. 12, pp. 1158–1165, 2012.
- [7] C. Mattevi, H. Kim, and M. Chhowalla, "A review of chemical vapour deposition of graphene on copper," *J. Mater. Chem.*, vol. 21, no. 10, pp. 3324–3334, 2011.
- [8] C. V. Thompson, "Solid-State Dewetting of Thin Films," *Annu. Rev. Mater. Res.*, vol. 42, no. 1, pp. 399–434, 2012.
- [9] D. J. Srolovitz and S. A. Safran, "Capillary instabilities in thin films. I. Energetics," *J. Appl. Phys.*, vol. 60, no. 1, pp. 247–254, 1986.
- [10] Lord Rayleigh, "On the Stability, or Instability, of certain Fluid Motions," *Proc. London Math. Soc.*, vol. s1-11, no. 1, pp. 57–72, 1879.
- [11] W. W. Mullins, "Flattening of a nearly plane solid surface due to capillarity," *J. Appl. Phys.*, vol. 30, no. 1, pp. 77–83, 1959.
- [12] E. Shaffir, I. Riess, and W. D. Kaplan, "The mechanism of initial de-wetting and detachment of thin Au films on YSZ," *Acta Mater.*, vol. 57, no. 1, pp. 248–256, 2009.
- [13] E. Jiran and C. V. Thompson, "Capillary instabilities in thin films," *J. Electron. Mater.*, vol. 19, no. 11, pp. 1153–1160, 1990.
- [14] R. Brandon and F. J. Bradshaw, "The mobility of the surface atoms of copper and silver evaporated deposits," Royal Aircraft Establishment, Farnborough Hants, 1966.
- [15] H. Wong, P. W. Voorhees, M. J. Miksis, and S. H. Davis, "Periodic mass shedding of a retracting

- solid film step,” *Acta Mater.*, vol. 48, no. 8, pp. 1719–1728, 2000.
- [16] F. Leroy *et al.*, “How to control solid state dewetting: A short review,” *Surf. Sci. Rep.*, vol. 71, no. 2, pp. 391–409, 2016.
- [17] L. Borowik *et al.*, “Method for making semi-conductor nanocrystals,” US 8,647,957 B2, 2014.
- [18] S. Curiotto, F. Leroy, F. Cheynis, and P. Müller, “Oxygen-induced inhibition of silicon-on-insulator dewetting,” *Appl. Phys. Lett.*, vol. 104, no. 6, 2014.
- [19] F. Richter, “Mechanical properties of solid bulk materials and thin films.” TU Chemnitz, Chemnitz, 2010.
- [20] F. Spaepen, “Interfaces and stresses in thin films,” *Acta Mater.*, vol. 48, no. 1, pp. 31–42, 2000.
- [21] W. D. Nix, “Mechanical properties of thin films,” *Class notes*. Stanford University, Stanford, 2005.
- [22] Dassault Systèmes, “Getting Started with Abaqus: Interactive edition.” Dassault Systèmes, Providence, RI, USA, 2012.
- [23] M. A. C. Fidalgo, “Mechanical behavior of nano-copper interconnects subjected to thermal loading,” Instituto Superior Técnico, 2019.
- [24] G. E. Dieter, *Mechanical Metallurgy*. McGraw-Hill, 1988.
- [25] CES EduPack 2013, “Copper properties.” Granta.
- [26] P. J. Karditsas and M.-J. Baptiste, “Thermal and Structural Properties of Fusion related Materials,” *Ukaea Fus 294*, 1995. [Online]. Available: <http://www-ferp.ucsd.edu/LIB/PROPS/PANOS/matintro.html>. [Accessed: 18-Mar-2019].
- [27] AZo Materials, “Molybdenum - Mechanical Properties And Material Applications,” 2017. [Online]. Available: <http://www.azom.com/article.aspx?ArticleID=3352>. [Accessed: 02-Oct-2018].
- [28] AZo Materials, “Silica - Silicon Dioxide (SiO₂),” 2001. [Online]. Available: <https://www.azom.com/properties.aspx?ArticleID=1114>. [Accessed: 02-Oct-2018].
- [29] EL-CAT, “Properties of silicon and silicon wafers,” 2009. [Online]. Available: <https://www.el-cat.com/silicon-properties.htm#5>. [Accessed: 02-Oct-2018].

Appendix

Appendix A: Methodology

Conversion table

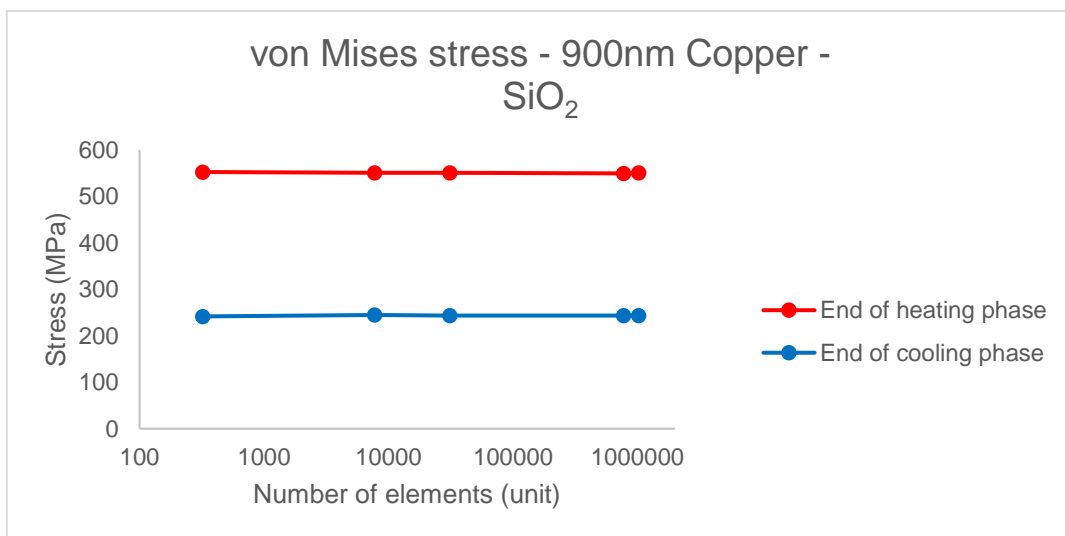
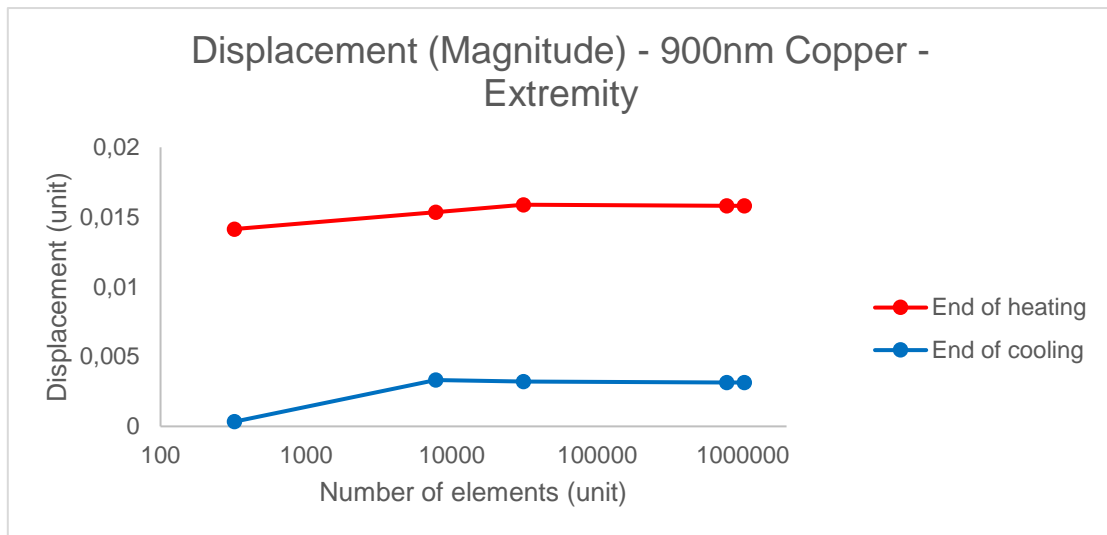
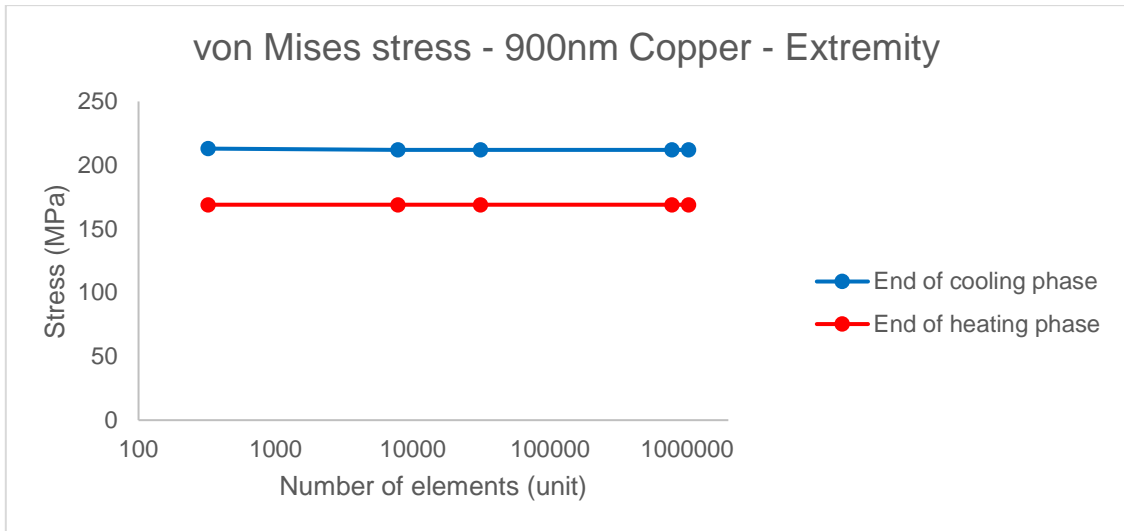
Parameter	Units(m)	Dimensions	Units(μm)	Dimensions	Multiplier m- \rightarrow μm
Length	m	-	μm	-	10^6
*Current	A	-	μA	-	10^{12}
Force	N	$\left[\frac{kg \cdot m}{s^2}\right]$	μN	$\left[\frac{kg \cdot \mu\text{m}}{s^2}\right]$	10^6
Mass	kg	-	kg	-	-
Time	s	-	s	-	-
Temperature	$^{\circ}\text{C}$	-	$^{\circ}\text{C}$	-	-
Thermal Expansion	$\frac{1}{^{\circ}\text{C}}$	-	$\frac{1}{^{\circ}\text{C}}$	-	-
Stress	Pa	$\left[\frac{kg}{m \cdot s^2}\right]$	MPa	$\left[\frac{kg}{\mu\text{m} \cdot s^2}\right]$	10^{-6}
Density	-	$\left[\frac{kg}{m^3}\right]$	-	$\left[\frac{kg}{\mu\text{m}^3}\right]$	10^{-18}
Power	W	$\left[\frac{kg \cdot m^2}{s^3}\right]$	pW	$\left[\frac{kg \cdot \mu\text{m}^2}{s^3}\right]$	10^{12}
Energy	J	$\left[\frac{kg \cdot m^2}{s^2}\right]$	pJ	$\left[\frac{kg \cdot \mu\text{m}^2}{s^2}\right]$	10^{12}
Thermal Conductivity	$\left[\frac{W}{m^{\circ}\text{C}}\right]$	$\left[\frac{kg \cdot m}{s^3^{\circ}\text{C}}\right]$	$\left[\frac{\text{pW}}{\mu\text{m}^{\circ}\text{C}}\right]$	$\left[\frac{kg \cdot \mu\text{m}}{s^3^{\circ}\text{C}}\right]$	10^6
Heat Flux	$\left[\frac{W}{m^2}\right]$	$\left[\frac{kg}{s^3}\right]$	$\left[\frac{\text{pW}}{\mu\text{m}^2}\right]$	$\left[\frac{kg}{s^3}\right]$	1
Specific Heat	$\left[\frac{J}{kg \cdot ^{\circ}\text{C}}\right]$	$\left[\frac{m^2}{^{\circ}\text{C} \cdot s^2}\right]$	$\left[\frac{\text{pJ}}{kg \cdot ^{\circ}\text{C}}\right]$	$\left[\frac{\mu\text{m}^2}{^{\circ}\text{C} \cdot s^2}\right]$	10^{12}
Convection Coefficient	$\left[\frac{W}{m^2^{\circ}\text{C}}\right]$	$\left[\frac{kg}{s^3^{\circ}\text{C}}\right]$	$\left[\frac{\text{pW}}{\mu\text{m}^2^{\circ}\text{C}}\right]$	$\left[\frac{kg}{s^3^{\circ}\text{C}}\right]$	1
Voltage	V	$\left[\frac{kg \cdot m^2}{A \cdot s^3}\right]$	V	$\left[\frac{kg \cdot \mu\text{m}^2}{\text{pA} \cdot s^3}\right]$	1
**Electrical Conductivity	$\left[\frac{S}{m}\right]$	$\left[\frac{A^2 \cdot s^3}{kg \cdot m^3}\right]$	$\left[\frac{\text{pS}}{\mu\text{m}}\right]$	$\left[\frac{\text{pA}^2 \cdot s^3}{kg \cdot \mu\text{m}^3}\right]$	10^6
Electrical Resistivity	$[\Omega\text{m}]$	$\left[\frac{kg \cdot m^3}{A^2 \cdot s^3}\right]$	$[\text{T}\Omega\mu\text{m}]$	$\left[\frac{kg \cdot \mu\text{m}^3}{\text{pA}^2 \cdot s^3}\right]$	10^{-6}

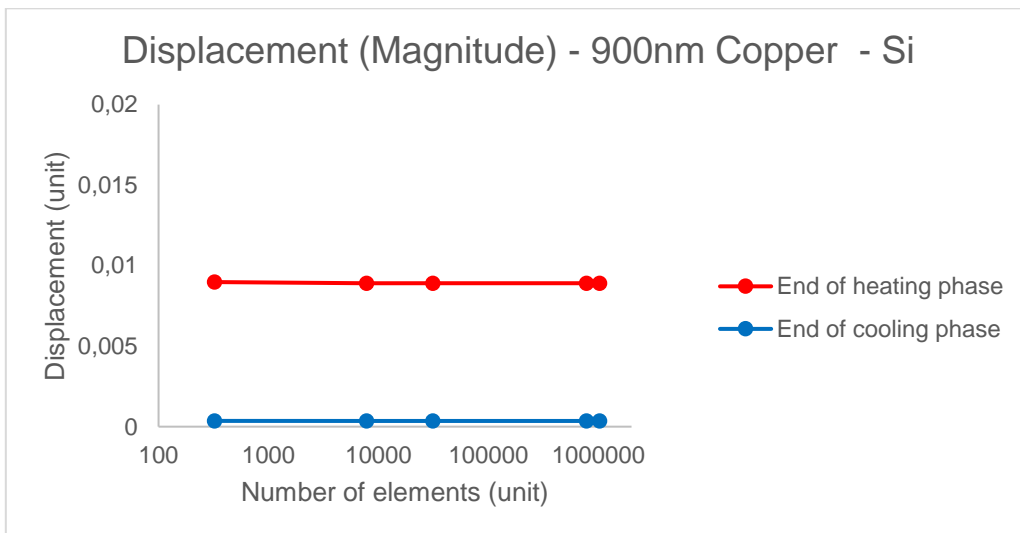
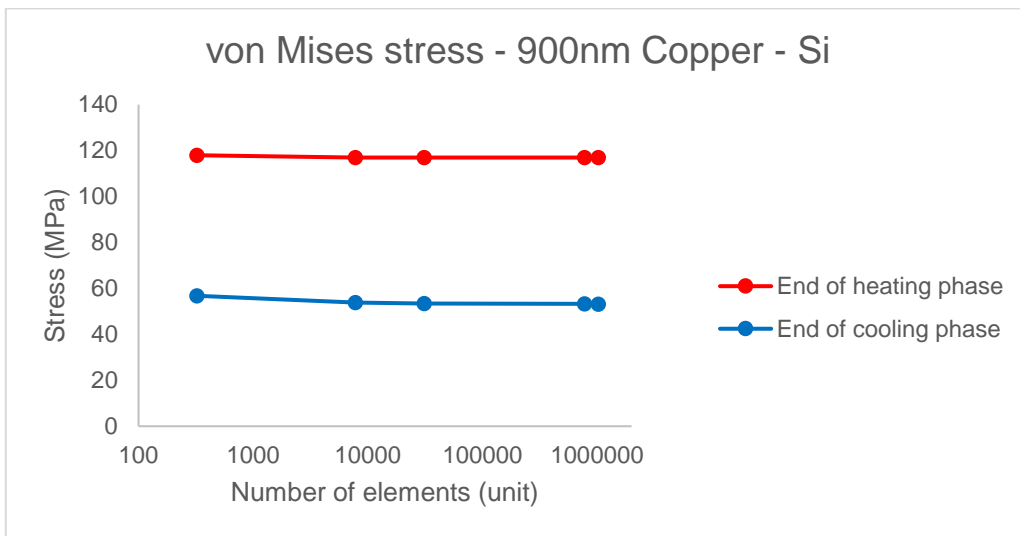
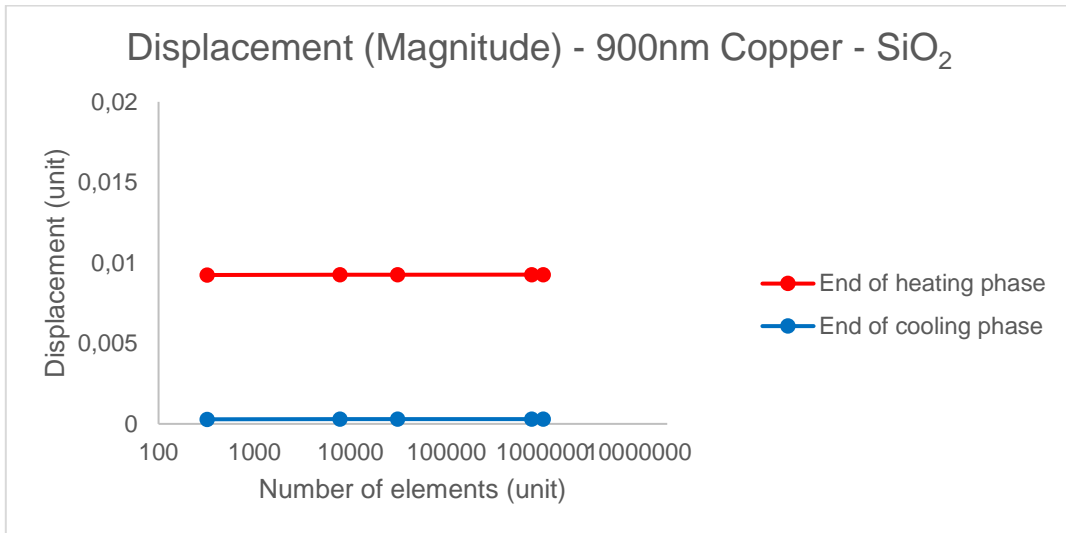
*For simplicity when working with Volts

$$**[S] = \left[\frac{A^2 \cdot s^3}{kg \cdot m^2}\right]$$

A.1 – Table with conversions from dimensional analysis [23]

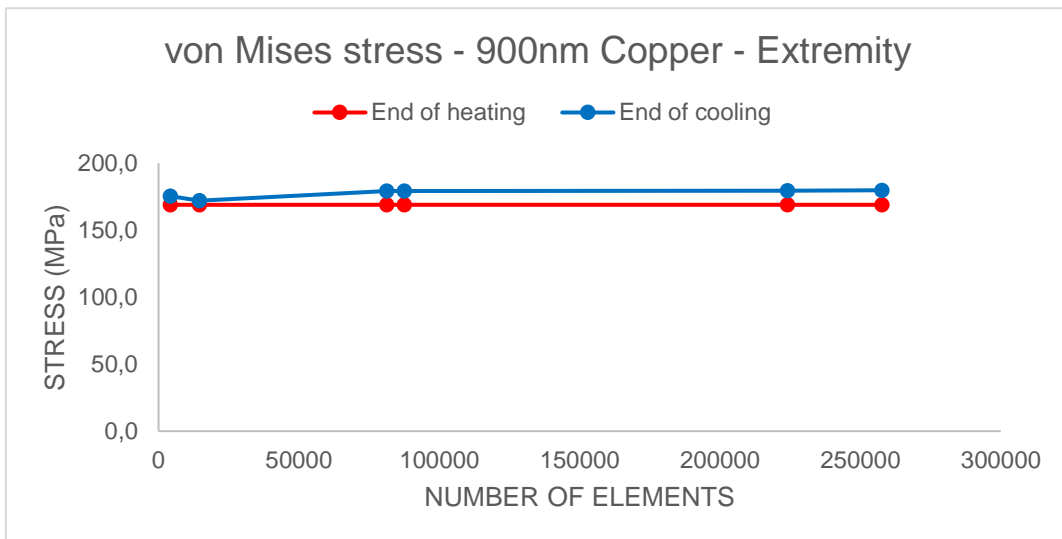
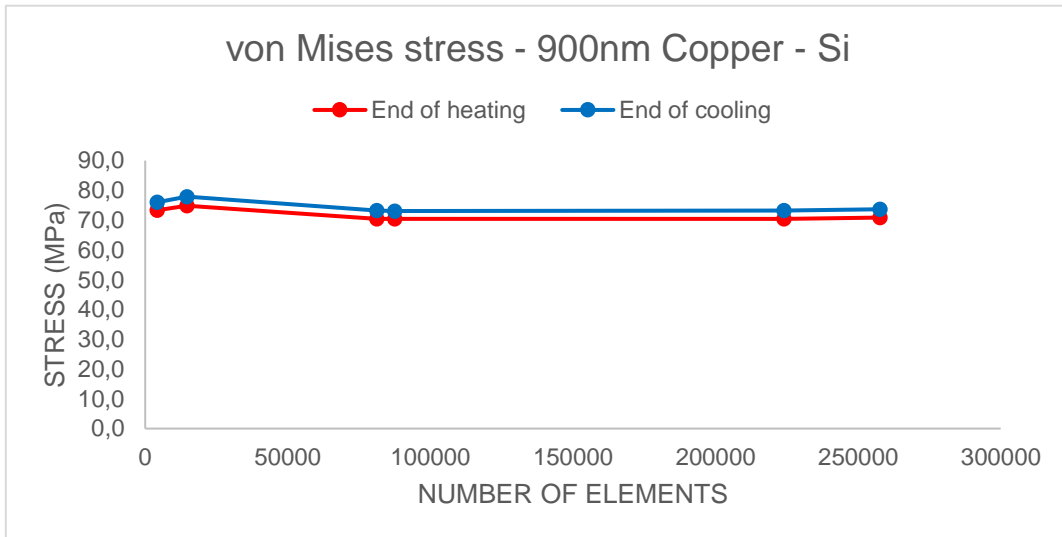
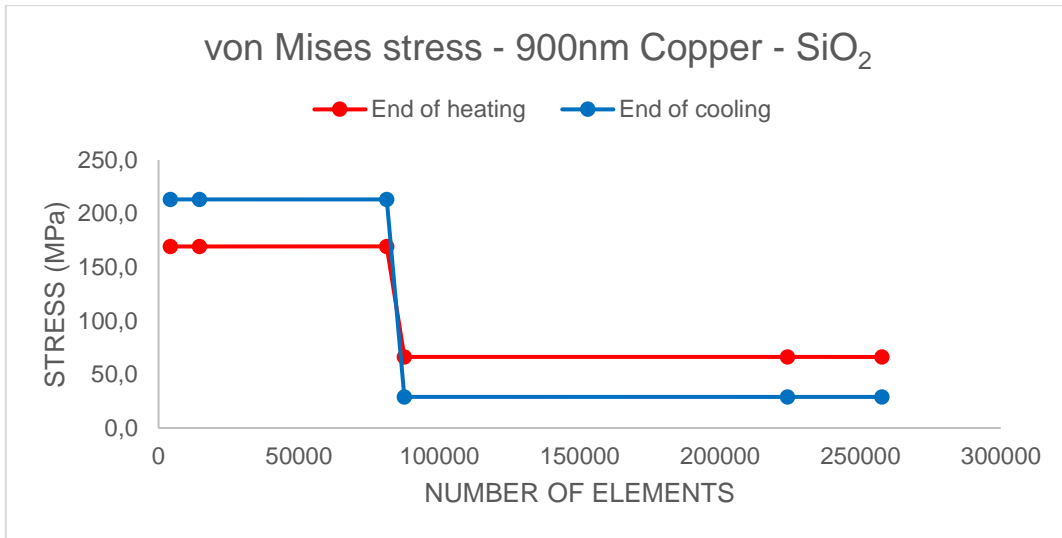
Convergence for the 2D model

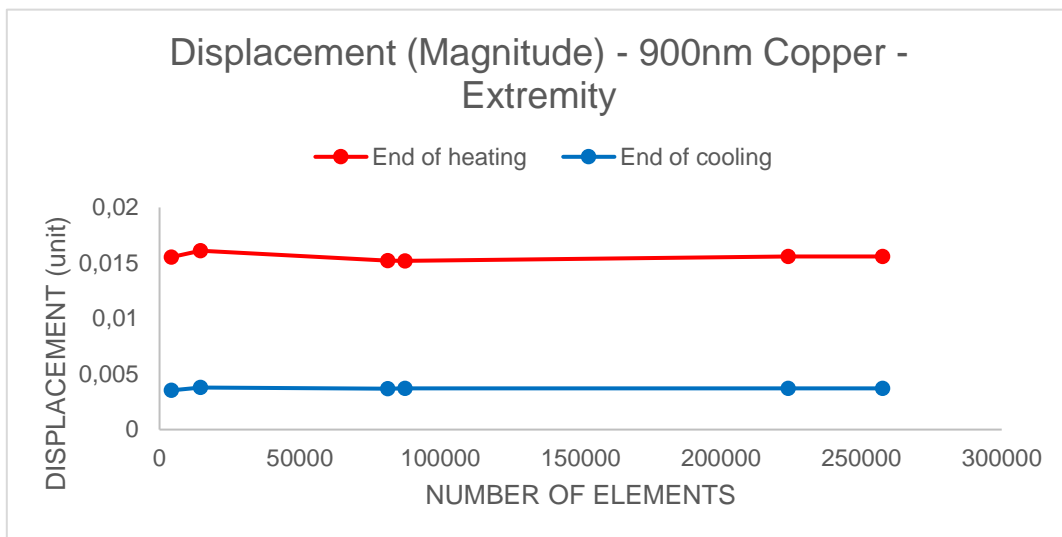
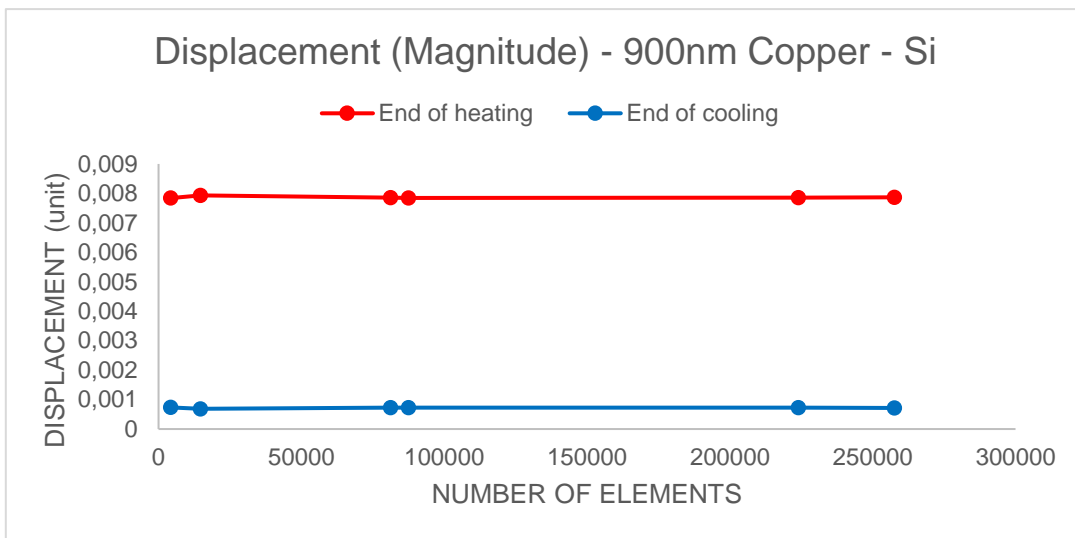
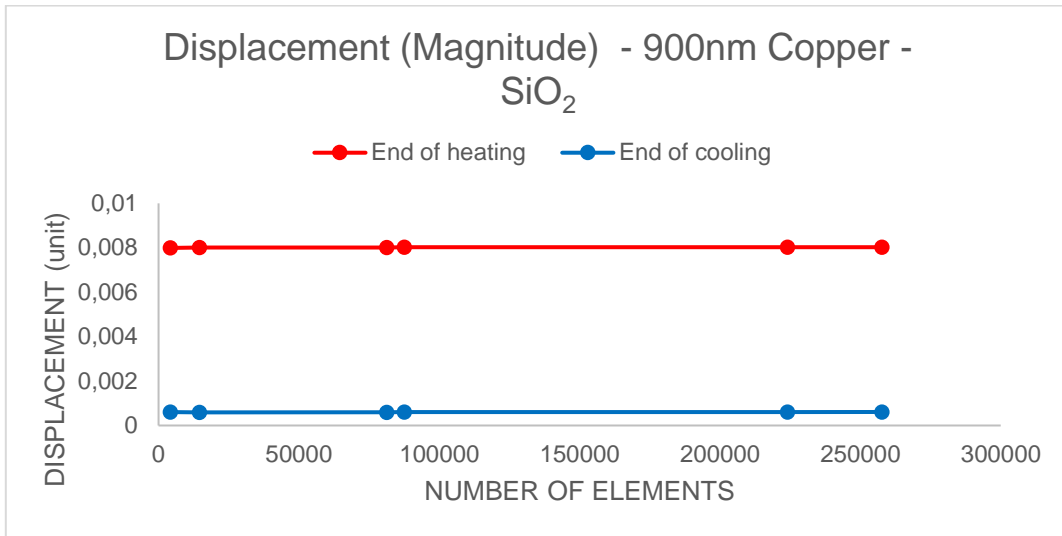




A.2 - Convergence graphs for the 2D model

Convergence for the 3D model





A.3 – Convergence graphs for the 3D model